STUDY ON THE ANALYSES OF THE COASTAL ACOUSTIC TOMOGRAPHY DATA

By

Jae-Hun Park

A DISSERTATION

SUBMITTED IN PARTIAL FULFILLMENT OF THE

REQUIREMENTS FOR THE DEGREE OF

DOCTOR OF ENGINEERING

AT

HIROSHIMA UNIVERSITY

June 2001

TABLE OF CONTENTS

CHAPTER 1

INTRODUCTION

1.1 Coastal acoustic tomography - new approach to the coastal sea monitoring

Monitoring current fields in the coastal seas can produce basic information in predicting disasters caused by ship traffic, oil spill, red tide, water pollution and so on. The conventional point measurement techniques for coastal currents possess an ability to measure current fields when the sufficient number of currentmeters are distributed inside the observation region. However, such arrangements of currentmeters are sometimes inhibited by heavy ship traffic and fishing activities. Those instruments may be usually very difficult to be placed for long-term use in the interior of the coastal regions such as channels or bays since such operations could damage the ships or the instruments themselves. There is also large possibility for the instruments to be caught accidentally by fishing nets. Furthermore, moored currentmeters deployed in the interior of the observation region with strong tidal currents are difficult to be fixed to the bottom. Mooring observation in the ship traffic route is strictly inhibited by the Japan Maritime Safety Agency and coast guard. Therefore, new approaches to continuous current field measurement in the coastal seas have attracted increased attention. The coastal acoustic tomography (CAT), which has a sampling strategy different from the conventional measurements, i.e., spatially averaged evaluation and remote sensing, is one of the promising approaches. The CAT ,which measures current fields by means of a multiple set of acoustic stations arrayed in the periphery

of the observation region, can improve drastically the capability of monitoring the structures of coastal currents.

Although a series of experiments have been conducted in the open ocean to validate the scheme of the ocean acoustic tomography since the first proposal by Munk and Wunsch [39], its application to the coastal seas has been done for only a few of cases because major interest of acoustic oceanographers has been concentrated on the open ocean. Unlike the open ocean, sound transmission in the coastal seas is much complicated due to the interference and scattering of sound waves with the sea surface and bottom. The phenomena causes a significant damping of sound waves which reduces largely the range of tomography experiments. Furthermore, the ambient noise level in the coastal seas is higher than that in the open ocean due to various man-made noises.

Variable tidal currents have recently been measured in a challenging way by a reciprocal sound transmission between two shipboard-type acoustic stations by Zheng *et al.* [51, 52]. A good agreement between the range-averaged current velocity measured by the reciprocal acoustic transmission and the shipboard ADCP (Acoustic Doppler current profiler) data obtained along the sound transmission line provided strong motivation for conducting the multi-station tomography experiment in the coastal seas. They used the GPS (global positioning system) clock signal to synchronize the timing of sound transmission and reception for all the acoustic stations. Precise measurement of travel time differences between paired acoustic stations was also performed by using the GPS clock signal.

In 1998, the CAT design was shifted from the shipboard to moored (self-contained) type, and five sets of the moored CATs were constructed at the beginning of 1999. In March 1999, the first CAT experiment was successfully carried out in the Neko-Seto Channel of the Seto Inland Sea, Japan. A target for this experiment was the current field measurement through reciprocal sound transmission between each station pair. Now a next important work for the CAT is shifted to seek the inversion scheme

suitable for coastal-sea application.

The inversion scheme for the open ocean tomography which has been developed well is not directly applied to the coastal seas because of the complicated bottom topography and coastline. Also the different strategy of inversion is needed for the coastal region with so variable velocity fields due to strong tidal currents.

1.2 Data analysis for the coastal acoustic tomography - inversion and data assimilation

There are two important points to be notified in the inversion for the coastal tomography. One is that current fields so variable with tidal phases and this situation make it difficult to retrieve *a priori* statistical information on current fields while most inversion schemes proposed previously for the open ocean tomography are based on *a priori* statistical information. The other is how to include the influence of coastlines into the inversion scheme. In the coastal tomography, the tomography region might be bounded by semi-enclosed and enclosed coastlines. At some cases, the coastlines are located on the both sides of the tomography region or either side of it. Until now, no inversions are constructed to consider the complicated coastlines.

The ocean acoustic tomography has attracted the attention of oceanographers because of its potential ability of serving the data assimilation, a methodology in which the observation data are combined optimally with a dynamical ocean model [38, 49]. In the CAT experiment, acoustic stations are generally placed near the coastlines, regarded as external boundaries of the observation region. However, the CAT experiment can produce data in the interior of the region, where data so useful for the data assimilation are obtained. Though several attempts have been made for the data assimilation related to the ocean acoustic tomography (*e.g.*, [15, 43, 6, 11, 35]), real tomographic data acquired in the ocean are rarely used. The assimilation of the real tomography data into a ocean model is still at a standing phase. The

algorithm for the assimilation of the CAT data is also a time to be developed because the CATs start to be operated in the sea.

In this thesis, two kinds of optimal inversions to process CAT data are proposed. The feasibility test of them are done through computer experiments in which various vortex fields are constructed by a spectral ocean model and the inversions are applied to the data analyses for the CAT field experiments.

Two kinds of data assimilation techniques, a time-invariant Kalman gain filter method based on the Chandrasekhar-type algorithm and a ensemble Kalman filter method based on the Monte Carlo method, are proposed for the analysis of the CAT data.

1.3 Overview

The contents of this thesis can be divided roughly into two parts. In the first part, composed of Chapters 2, 3, and 4, inversion and data assimilation methods for the CAT are introduced. Chapter 2 starts with a brief introduction of forward and inverse problems and it is followed by the inversion schemes for the ocean acoustic tomography. Chapter 3 is reserved for the data assimilation. The Kalman filter algorithm and its approximation methods, applicable to the CAT, are described. This is followed by an inversion which does not require the *a priori* statistical information as presented in Chapter 4. The optimal inversion for the CAT are examined through computer experiments.Two methods to include the influence of coastlines in the inversion are proposed.

The second part, Chapter 5, deals with two kinds of data analyses, namely the inversion and data assimilation. Finally, general discussion and conclusions are given in Chapters 6 and 7, respectively.

CHAPTER 2

FORWARD AND INVERSE PROBLEMS

2.1 Basic concepts of the ocean acoustic tomography

The ocean acoustic tomography is a scheme to infer sound speed or current velocity fields of the intervening ocean from the travel time of sound, which is the function of sound speed and current velocity. It has special advantage to get the snapshots of small scale to large scale phenomena in the ocean, which is so difficult to be done by conventional shipboard and mooring techniques. The speed of sound in the ocean is as fast as 1.5kms^{-1} which permits the reconstruction of synoptic fields of mesoscale or even large scale. In case of conventional moorings the number of data is equal to that of one-point measurement stations, while N tomography stations produce the data number of ${}_NC_2$. With increasing number of the stations, the spatial resolution for the acoustic tomography becomes much better in comparison with the conventional method. There is also a proper aspect of the acoustic tomography such that all data are path-averaged ones along the ray and no point-measurement data are acquired. Another aspect of the acoustic tomography is that it is one of the remote sensing techniques. Ocean interiors, where the direct observation is difficult due to ship traffic, fishing grounds, military training areas, etc, become targets to be measured continuously by the tomography stations arrayed at the periphery of the observation region.

2.2 Forward problem

Sound waves which propagate from the source to receiver are influenced by the sound speed $C(x, y, z)$ and current velocity $\mathbf{u}(x, y, z)$ in the intervening water. This is called the forward problem and the detailed properties of received signals can be calculated by solving the sound wave equation with the given values of C and $\mathbf{u}$. To understand the forward problem is so important to solve optimally the inverse problem because received acoustic signals have to be identified for making the inversion accurate and successful. As for the ocean acoustic tomography, the forward problem is solved by the computer simulation in which *a priori* sound speed data obtained in the observation region are used. The received signals can be identified by comparing the simulated results with observed ones.

The observable data for the ocean acoustic tomography are travel times and intensities of received signals while the latter are out of scope in this study. Early arrival rays and lately arrival rays take different ray paths and thus experience different sound speed and current velocity fields.

The travel times of sound between two acoustic transceivers along the reciprocal ray paths can be formulated

$$t^{\pm} = \oint_{\Gamma^{\pm}} \frac{ds}{C(x, y, z) + \mathbf{u}(x, y, z) \cdot \mathbf{n}} \tag{2.1}$$

where +/- represents the positive/negative direction from one transceiver to another, $\mathbf{n}$ the unit vector tangent to the ray path and s the arc length measured along the ray path. $\Gamma^{\pm}$ are the positive and negative paths refracted by $C(x, y, z)$ and $\mathbf{u}(x, y, z) \cdot \mathbf{n}$. The ray paths are generally not coincident for two ways in the reciprocal transmission, but we can approximate $\Gamma^{+} \simeq \Gamma^{-} \equiv \Gamma_0$ when $\mathbf{u} \cdot \mathbf{n}/C \ll 1$. The mean travel time perturbation δt and the differential travel time Δt are expressed by

$$\delta t \;=\; \frac{1}{2}(t^{+} + t^{-}) - t_0 \simeq -\oint_{\Gamma_0} \frac{\delta C(x, y, z)}{C_0(z)^2} ds \tag{2.2}$$

$$\Delta t = \frac{1}{2}(t^+ - t^-) \simeq -\oint_{\Gamma_0} \frac{\mathbf{u}(x,y,z)\cdot\mathbf{n}}{C_0(z)^2} ds \tag{2.3}$$

where t_0 is the travel time along the ray path Γ_0 associated with a reference sound speed $C_0(z)$ and $\delta C(x,y,z)\Big(= C(x,y,z) - C_0(z)\Big)$ is the sound speed perturbation. We also assume $\delta C/C \ll 1$. These are the linearized formulations for the acoustic travel times obtained in the oceanic environment with C and $\mathbf{u}$. Equations (2.2) and (2.3) are kinds of integral equations with the unknown variables δC and $\mathbf{u}$.

2.3 Inverse problem

Suppose that there are M numbers of rays and N numbers of discrete segments with the unknown values $\delta C(x,y,z)$ and $\mathbf{u}(x,y,z)$. Then equations (2.2) and (2.3) can be rewritten

$$\delta t_i = \sum_j^N E_{ij}\delta C_j + \delta\epsilon_i \tag{2.4}$$

$$\Delta t_i = \sum_j^N E_{ij}\mathbf{u}_j + \Delta\epsilon_i \qquad \text{for} \quad i = 1,\ldots,M \tag{2.5}$$

where $\delta\epsilon_i$ and $\Delta\epsilon_i$ are introduced to represent the noise contributions to δt_i and Δt_i, respectively. E_{ij} can be evaluated

$$E_{ij} = -\oint_{\Gamma_{0ij}} \frac{1}{C_j(z)^2} ds \tag{2.6}$$

where Γ_{0ij} is the distance traveled by the i-th ray in the j-th segment and $C_j(z)$ the reference sound speed in the same area j. Equation (2.4)/(2.5) is a set of M-order coupled equations with the N unknown values $\delta C_j/\mathbf{u}_j$. Both the equations can be written with a compact matrix notation

$$\mathbf{y} = \mathbf{E}\mathbf{x} + \mathbf{e} \tag{2.7}$$

with

$$
\begin{aligned}
\mathbf{y} &= [\delta t_1, \ldots, \delta t_M] \quad \text{or} \quad [\Delta t_1, \ldots, \Delta t_M] \\
\mathbf{E} &= \begin{pmatrix} E_{11} & \cdots & E_{1N} \\ \vdots & \ddots & \vdots \\ E_{M1} & \cdots & E_{MN} \end{pmatrix} \\
\mathbf{x} &= [\delta C_1, \ldots, \delta C_N] \quad \text{or} \quad [\mathbf{u}_1, \ldots, \mathbf{u}_N] \\
\mathbf{e} &= [\delta \epsilon_1, \ldots, \delta \epsilon_M] \quad \text{or} \quad [\Delta \epsilon_1, \ldots, \Delta \epsilon_M]
\end{aligned} \tag{2.8}
$$

The inverse problem is to determine the unknown variable $\mathbf{x}$ which fits optimally to the observational data $\mathbf{y}$ under the presence of noise $\mathbf{e}$.

2.4 Inversion schemes

2.4.1 Lease squares method

The least squares method is a classical method which can be applied to the overdetermined case, i.e., $M > N$. The best fitted solution that makes the noise as small as possible is obtained by minimizing the "objective function" (J)

$$
\begin{aligned}
J &= \mathbf{e}^T\mathbf{e} = (\mathbf{y} - \mathbf{E}\mathbf{x})^T(\mathbf{y} - \mathbf{E}\mathbf{x}) \\
&= \mathbf{x}^T\mathbf{E}^T\mathbf{E}\mathbf{x} - \mathbf{x}^T\mathbf{E}^T\mathbf{y} - \mathbf{y}^T\mathbf{E}\mathbf{x} + \mathbf{y}^T\mathbf{y}
\end{aligned} \tag{2.9}
$$

Differentiating equation (2.9) with respect to $\mathbf{x}$ in consideration of the following relations

$$
\frac{\partial(\mathbf{x}^T\mathbf{y})}{\partial\mathbf{x}} = \frac{\partial(\mathbf{y}^T\mathbf{x})}{\partial\mathbf{x}} = \mathbf{y} \tag{2.10}
$$

$$
\frac{\partial(\mathbf{x}^T\mathbf{E}^T\mathbf{E}\mathbf{x})}{\partial\mathbf{x}} = \left(\mathbf{E}^T\mathbf{E} + (\mathbf{E}^T\mathbf{E})^T\right)\mathbf{x} \tag{2.11}
$$

and setting

$$\frac{\partial J}{\partial \mathbf{x}} = 0 \tag{2.12}$$

lead to the equation

$$\mathbf{E}^T\mathbf{E}\mathbf{x} = \mathbf{E}^T\mathbf{y} \tag{2.13}$$

When $(\mathbf{E}^T\mathbf{E})^{-1}$ exists, the expected value $\hat{\mathbf{x}}$ for $\mathbf{x}$ reduces to

$$\hat{\mathbf{x}} = (\mathbf{E}^T\mathbf{E})^{-1}\mathbf{E}^T\mathbf{y} \tag{2.14}$$

$$\hat{\mathbf{e}} = \mathbf{y} - \mathbf{E}\hat{\mathbf{x}} = (\mathbf{I} - \mathbf{E}(\mathbf{E}^T\mathbf{E})^{-1}\mathbf{E}^T)\mathbf{y} \tag{2.15}$$

The solution based on equation (2.14) has serious shortcomings; (i)for the underdetermined case, i.e., $M < N$, the inverse matrix $(\mathbf{E}^T\mathbf{E})^{-1}$ never exists, and (ii)the solution may have an error of unacceptable magnitude due to the less independency of data and the existence of significant noises.

The characteristic properties of the least squares method can be illustrated by using the singular value decomposition (SVD) of the matrix $\mathbf{E}$. We shall put

$$\mathbf{E} = \sum_{i=1}^{N} \lambda_i \mathbf{u}_i \mathbf{v}_i^T \tag{2.16}$$

where $\mathbf{u}_i$ and $\mathbf{v}_i$ are the orthonormal eigenvectors for the data and model spaces, respectively. The eigenvalues λ_i are non-negative and ordered with decreasing magnitudes, i.e., $\lambda_1 \geq \lambda_2 \geq \cdots \geq \lambda_N \geq 0$. By substituting equation (2.16) into (2.14), $\hat{\mathbf{x}}$ reduces to

$$\hat{\mathbf{x}} = \sum_{i=1}^{N} \frac{\mathbf{u}_i^T\mathbf{y}}{\lambda_i}\mathbf{v}_i \tag{2.17}$$

In equation (2.17), the divergence problem of the solution occurs when quite small eigenvalues are included and the resulting solution becomes dominated by only the terms which correspond to the small eigenvalues. This problem may be relaxed by

multiplying the filter factor f_i to equation (2.17) as follows:

$$\hat{\mathbf{x}}_f = \sum_{i=1}^{N} f_i \frac{\mathbf{u}_i^T \mathbf{y}}{\lambda_i} \mathbf{v}_i \tag{2.18}$$

where $0 \leq f_i \leq 1$. For $f_i = 1$, solution (2.18) reduces to the least squares solution (2.17).

One of the well-known methods which consider the filter factors is the damped least squares method that starts from modifying the objective function (2.9) with an additional term as

$$J = \mathbf{e}^T \mathbf{e} + \alpha^2 \mathbf{x}^T \mathbf{x} = (\mathbf{y} - \mathbf{E}\mathbf{x})^T (\mathbf{y} - \mathbf{E}\mathbf{x}) + \alpha^2 \mathbf{x}^T \mathbf{x} \tag{2.19}$$

where α^2 is a weighting factor to change the ratio of the variance of the error to that of the solution. This method is sometimes called the tapered least squares method. By setting the derivative of equation (2.19) with respect to $\mathbf{x}$ to zero as done in (2.12), the solution and error result in

$$\hat{\mathbf{x}} = (\mathbf{E}^T \mathbf{E} + \alpha^2 \mathbf{I})^{-1} \mathbf{E}^T \mathbf{y} \tag{2.20}$$

$$\hat{\mathbf{e}} = \mathbf{y} - \mathbf{E}\hat{\mathbf{x}} = (\mathbf{I} - \mathbf{E}(\mathbf{E}^T \mathbf{E} + \alpha^2 \mathbf{I})^{-1} \mathbf{E}^T) \mathbf{y} \tag{2.21}$$

Here, the solution is also rewritten by using the equation (2.16)

$$\hat{\mathbf{x}} = \sum_{i=1}^{N_r} \frac{\lambda_i (\mathbf{u}_i^T \mathbf{y})}{\lambda_i^2 + \alpha^2} \mathbf{v}_i \tag{2.22}$$

and the filter factors f_i are expressed by

$$f_i = \frac{\lambda_i^2}{\lambda_i^2 + \alpha^2} \tag{2.23}$$

The role of f_i is to damp or filter out the contribution of eigenvalues smaller than α on

the solution $\hat{\mathbf{x}}$. As the largest errors of the least squares solution are associated with the smallest eigenvalues, it is clear that the damped least squares method is so useful when the quite small eigenvalues appear in the solution (2.22). Another important point for the damped least squares method is that the inverse matrix $(\mathbf{E}^T\mathbf{E} + \alpha^2\mathbf{I})^{-1}$ always exists even for the underdetermined problem, $M < N$, as long as $\alpha^2 > 0$.

The best optimal value of α^2 had been discussed by Hoerl and Kennard [25] and Lawson and Hanson [31]. Recently, Hansen [20] and Hansen and O'leary [21] developed the L-curve method, proposed originally by Lawson and Hanson [31]. The scheme of the L-curve method and its application to the analysis of the tomography field data are presented in Chapter 4.

2.4.2 Gauss-Markov estimate

A quite different approach of inversion, called the Gauss-Markov estimate, starts from attempting to minimize the expected uncertainty, a difference between the true value of $\mathbf{x}$ and its estimate $\hat{\mathbf{x}}$,

$$\mathbf{P} = < (\hat{\mathbf{x}} - \mathbf{x})(\hat{\mathbf{x}} - \mathbf{x})^T > \tag{2.24}$$

where the individual diagonal elements, not the sum of their squares, are to be minimized. The difference may be understood in comparison with equation (2.9), in which the sum of the squared residuals $\sum \mathbf{e}_i^2$ is required to be minimized.

The $\hat{\mathbf{x}}$ may be described as a linear combination of data

$$\hat{\mathbf{x}} = \mathbf{B}\mathbf{y} \tag{2.25}$$

In the method called the Gauss-Markov estimate, the $M \times N$ matrix $\mathbf{B}$ is determined to minimize the diagonal components of $\mathbf{P}$. Substituting (2.25) into (2.24) yields the

expected uncertainty as

$$\begin{aligned} \mathbf{P} &= <(\mathbf{By}-\mathbf{x})(\mathbf{By}-\mathbf{x})^T> \\ &= \mathbf{B}<\mathbf{yy}^T>\mathbf{B}^T - <\mathbf{xy}^T>\mathbf{B}^T - \mathbf{B}<\mathbf{yx}^T> + <\mathbf{xx}^T> \end{aligned} \tag{2.26}$$

By using the following notations

$$\mathbf{R}_{xx} = <\mathbf{xx}^T>, \qquad \mathbf{R}_{yx} = <\mathbf{yx}^T> = \mathbf{R}_{xy}^T, \qquad \mathbf{R}_{yy} = <\mathbf{yy}^T> \tag{2.27}$$

equation (2.26) becomes

$$\mathbf{P} = \mathbf{B}\mathbf{R}_{yy}\mathbf{B}^T - \mathbf{R}_{xy}\mathbf{B}^T - \mathbf{B}\mathbf{R}_{xy}^T + \mathbf{R}_{xx} \tag{2.28}$$

By use of the matrix inversion identity derived by Liebelt [32], equation (2.28) becomes

$$\mathbf{P} = (\mathbf{B}-\mathbf{R}_{xy}\mathbf{R}_{yy}^{-1})\mathbf{R}_{yy}(\mathbf{B}-\mathbf{R}_{xy}\mathbf{R}_{yy}^{-1})^T - \mathbf{R}_{xy}\mathbf{R}_{yy}^{-1}\mathbf{R}_{xy}^T + \mathbf{R}_{xx} \tag{2.29}$$

Since $\mathbf{R}_{xx}$, $\mathbf{R}_{yy}$ and $\mathbf{R}_{yy}^{-1}$ are positive, the diagonal components of all three terms on the right-hand side of equation (2.29) are positive. Therefore, the matrix $\mathbf{B}$ which minimizes the diagonals of $\mathbf{P}$ must be chosen to vanish the first term of (2.29) as

$$\mathbf{B} = \mathbf{R}_{xy}\mathbf{R}_{yy}^{-1} \tag{2.30}$$

The estimate $\hat{\mathbf{x}}$ obtained through $\mathbf{B}$ is called the Gauss-Markov estimate, and also called the stochastic inverse estimate.

When using equation (2.7), $\mathbf{R}_{xy}$ is determined

$$\mathbf{R}_{xy} = <\mathbf{x}(\mathbf{Ex}+\mathbf{e})^T> = \mathbf{R}_{xx}\mathbf{E}^T \tag{2.31}$$

under the assumption that there is no correlation between $\mathbf{x}$ and $\mathbf{e}$. $\mathbf{R}_{yy}$ is also determined similarly

$$\mathbf{R}_{yy} =< (\mathbf{Ex}+\mathbf{e})(\mathbf{Ex}+\mathbf{e})^T >= \mathbf{E}\mathbf{R}_{xx}\mathbf{E}^T + \mathbf{R}_{ee} \tag{2.32}$$

As a result, the solution $\hat{\mathbf{x}}$ and residual $\hat{\mathbf{e}}$ reduce to

$$\hat{\mathbf{x}} = \mathbf{R}_{xx}\mathbf{E}^T(\mathbf{E}\mathbf{R}_{xx}\mathbf{E}^T + \mathbf{R}_{ee})^{-1}\mathbf{y} \tag{2.33}$$

$$\hat{\mathbf{e}} = (\mathbf{I} - \mathbf{E}\mathbf{R}_{xx}\mathbf{E}^T(\mathbf{E}\mathbf{R}_{xx}\mathbf{E}^T + \mathbf{R}_{ee})^{-1})\mathbf{y} \tag{2.34}$$

The Gauss-Markov estimate (2.33) is here compared with the damped least squares estimate (2.20). When α^2 is chosen to be the ratio of the covariance matrix of $\mathbf{x}$ to that of $\mathbf{e}$, the both equations become coincident.

A priori statistical information is needed to estimate $\mathbf{R}_{xx}$ and $\mathbf{R}_{nn}$. The accurate estimate is not obtained without sufficient *a priori* information, but such information is usually lacked especially for the current velocity. This is a limitation of the Gauss-Markov estimate.

2.5 Summary and discussion

In this chapter, the method of data analysis associated with the ocean acoustic tomography have been investigated. In the forward problem, the travel times of sound from one acoustic station to another are simulated by a computer, using the given sound speed data. Comparison of the simulated and observed travel time patterns is so useful in ray identification which leads us to solve the inverse problem. The fields of temperature and current velocity are reconstructed by the inverse analyses which use the identified travel time data.

The least squares method, damped least squares method and Gauss-Markov method are introduced as suitable inversion techniques for the ocean acoustic tomography.

The Gauss-Markov method has been used as the most familiar technique. However, in the case with lacked statistical information, the least squares method may be an alternative to be selected. When the least squares method has problems related to smaller eigenvalues for the matrix $\mathbf{E}$, it should be replaced by the damped least squares method.

CHAPTER 3

DATA ASSIMILATION

3.1 Introduction

The ocean model is capable of simulating the circulation at various scales with a high spatial resolution. However, the accuracy of the ocean model must be validated because of selectable, unknown parameters and open boundary conditions. On the other hand, the observation can provide actual information on the ocean, but the spatial resolution is usually so limited. The spatial resolution of the CAT is not dramatically improved because there are special characteristics that the CAT deals with the path-averaged information and has the limited number of acoustic stations. This provides a strong motivation for assimilating of the CAT data into the ocean model of a fine spatial resolution.

Data assimilation is an intelligent technique to incorporate the measured data into the numerical ocean model in an optimal way. An overview of the data assimilation method is presented by Ghil and Malanotte-Rizzoli [18]. It may be separated into two categories of sequential and variational assimilation methods. The Kalman filter [28, 29] is one of the most well-known and widely used sequential assimilation methods. The Kalman filter algorithm uses a two-step procedure. First, the model is integrated from the previous state to the present one at which the new observational data are available. Second, this model prediction is corrected in comparison with the new data.

Recently, a field experiment was carried out by Elisseeff *et al.* [11] who assimilated the acoustic tomography and point-measurement data into the coastal ocean model. They used the melding scheme in which the modeling result are merged with the tomography and point measurement data. However, this melding scheme is based on the statistical properties of model prediction and measurement errors which is independent of time. It is likely that the statistical properties of the prediction and measurement errors evolve with time in the coastal environments. The Kalman filter scheme, in which the prediction errors change with time through the model, may be a more suitable assimilation technique than the melding scheme in the CAT.

In this chapter the basic Kalman filter theory and two simplified Kalman gain filters applicable to the CAT are introduced.

3.2 Kalman filter theory

Propagation of the state vector in a linear stochastic discretized model may be represented by

$$\mathbf{x}_{k+1} = \mathbf{A}_k \mathbf{x}_k + \mathbf{B}_k \mathbf{w}_k + \mathbf{\Gamma}_k \mathbf{q}_k \tag{3.1}$$

where $\mathbf{x}_k$ is the state vector at time t_k with length n, which corresponds to the number of grid points multiplied by the number of prognostic variables. $\mathbf{A}_k$ is the $n \times n$ state transition matrix that represents the ocean model dynamics. The matrix $\mathbf{B}_k$ distributes the external forcing, represented by $\mathbf{w}_k$, over the whole ocean model grid. The $\mathbf{q}_k$ represents the model errors which include the uncertainty of the external forcing and $\mathbf{q}_k$ is assumed to have a zero mean and known covariance matrix $\mathbf{Q}_k$. $\mathbf{\Gamma}_k$ for $\mathbf{q}_k$ plays the same role as $\mathbf{B}_k$ for $\mathbf{w}_k$

Under the assumption that measurements $\mathbf{y}_k$ available for the data assimilation are linearly related to the state vector $\mathbf{x}_k$, the observation equation is written

$$\mathbf{y}_k = \mathbf{E}_k \mathbf{x}_k + \mathbf{e}_k \tag{3.2}$$

where $\mathbf{E}_k$ is the observation matrix which contains a relation between the prognostic model variables and measurements and $\mathbf{e}_k$ the measurement error assumed to have a zero mean and known covariance matrix $\mathbf{R}_k$.

The optimal state estimate and the model errors are propagated from t_k to t_{k+1} in the following forms:

$$\mathbf{x}^f_{k+1} = \mathbf{A}_k \mathbf{x}^a_k + \mathbf{B}_k \mathbf{w}_k \tag{3.3}$$

and

$$\mathbf{P}^f_{k+1} = \mathbf{A}_k \mathbf{P}^a_k \mathbf{A}^T_k + \mathbf{\Gamma}_k \mathbf{Q}_k \mathbf{\Gamma}^T_k \tag{3.4}$$

respectively, where the superscripts f and a represent the forecasted value and analyzed value, respectively. $\mathbf{P}_k$ is the error covariance matrix for the state vector variables $\mathbf{x}_k$

The optimal estimate of the ocean state for the system at time t_{k+1} is obtained

$$\mathbf{x}^a_{k+1} = \mathbf{x}^f_{k+1} + \mathbf{K}_{k+1}(\mathbf{y}_{k+1} - \mathbf{E}_{k+1}\mathbf{x}^f_{k+1}) \tag{3.5}$$

where $\mathbf{K}_{k+1}$ is the Kalman gain, the weighting factor added to the innovation vector which is a difference between the observed and forecasted variables. The Kalman gain is expressed by

$$\mathbf{K}_{k+1} = \mathbf{P}^f_{k+1}\mathbf{E}^T_{k+1}(\mathbf{E}_{k+1}\mathbf{P}^f_{k+1}\mathbf{E}^T_{k+1} + \mathbf{R}_{k+1})^{-1} \tag{3.6}$$

The Kalman gain is dependent on both the error covariance matrix $\mathbf{P}^f_{k+1}$ and measurement error $\mathbf{R}_{k+1}$. The analyzed value of the error covariance matrix are given as

$$\mathbf{P}^a_{k+1} = \mathbf{P}^f_{k+1} - \mathbf{K}_{k+1}\mathbf{E}_{k+1}\mathbf{P}^f_{k+1} \tag{3.7}$$

The process described in equations (3.3) - (3.7) is the optimal estimate procedures of the Kalman filter. In principle, the Kalman filter procedures are applicable to solve

various data assimilation problems. However, if these procedures are used as it is, computational and memory requirements increase rapidly with the dimension of state vector $\mathbf{x}$. Particularly, estimating the error covariance matrix $\mathbf{P}_k$ by equation (3.4) is the most time consuming part because it takes $2n$ times the model computational time needed for proceeding one time step. Moreover, it requires $n \times n$ memory spaces. Another difficulty in the application of the Kalman filter to the data assimilation is the appropriateness to use the linear model. Of course the Kalman filter can be applied to the nonlinear case, but more computational times in use of this algorithm are needed. Therefore, a lot of effort has been devoted to find computationally effective Kalman filters, which may be separated into two groups of the time-invariant and time-variant Kalman gain filters.

3.3 Time-invariant Kalman gain filter

The Kalman gain $\mathbf{K}_{k+1}$ is independent of the measurements $\mathbf{y}$ as seen in the equation (3.6), so it can be calculated in advance and stored for the following computation. The Kalman gain stored is used during the subsequent filterings. An noticeable approach to the time-invariant Kalman gain filter was proposed by Fukumori and Malanotte-Rizzoli [15], who assimilated the simulated altimeter data and the simulated path-averaged acoustic tomography data into the nonlinear, primitive equation model of the Gulf Stream. They reduced remarkably the computational time by using the Kalman filter state space with grid sizes much coarser than the original ones. However, no applications of this assimilation technique to the coastal seas with complicated coastlines and bottom topographies are attempted because of the difficult interpolation method to simulate the land-sea boundary.

In this section, an approach based on the Chandrasekhar-type filter algorithm is introduced because this algorithm has no limitation in application to the coastal seas. When the dimension of system noise process p is much less than that of system states n, i.e., $p << n$, the Chandrasekhar-type algorithm provides a significant reduction

of computational time. The major aspect of this algorithm is that the incremental covariance is factorized by eigendecomposition as

$$\begin{aligned} \mathbf{P}^a_{k+1} - \mathbf{P}^a_k &= \mathbf{S}_{k+1}\mathbf{L}_{k+1}\mathbf{S}^T_{k+1} \\ \mathbf{P}^f_{k+1} - \mathbf{P}^f_k &= \mathbf{Y}_k\mathbf{L}_k\mathbf{Y}^T_k \end{aligned} \tag{3.8}$$

where $\mathbf{S}_{k+1}$ and $\mathbf{Y}_k$ are $n \times p$ matrices and $\mathbf{L}_{k+1}$ is a $p \times p$ matrix. For the state vector propagation equation (3.1) and the observation equation (3.2) the time-invariant Kalman gain $\mathbf{K}$ are formulated as follows:

$$\begin{aligned} \mathbf{G}_{n+1} &= \mathbf{G}_n + \mathbf{Y}_n\mathbf{L}_n\mathbf{Y}^T_n\mathbf{E}^T \\ \mathbf{R}_{n+1} &= \mathbf{R}_n + \mathbf{E}\mathbf{Y}_n\mathbf{L}_n\mathbf{Y}^T_n\mathbf{E}^T \\ \mathbf{K}_{n+1} &= \mathbf{G}_{n+1}\mathbf{R}^{-1}_{n+1} \\ \mathbf{S}_{n+1} &= \mathbf{Y}_n - \mathbf{K}_{n+1}\mathbf{E}\mathbf{Y}_n \\ \mathbf{L}_{n+1} &= \mathbf{L}_n + \mathbf{L}_n\mathbf{Y}^T_n\mathbf{E}^T\mathbf{R}^{-1}_n\mathbf{E}\mathbf{Y}_n\mathbf{L}_n \\ \mathbf{Y}_{n+1} &= \mathbf{A}\mathbf{S}_{n+1} \end{aligned} \tag{3.9}$$

where n denotes the number of iteration. The initial conditions are

$$\mathbf{Y}_0 = \Gamma, \qquad \mathbf{G}_0 = 0, \qquad \mathbf{R}_0 = \mathbf{R}, \qquad \mathbf{L}_0 = \mathbf{Q}$$

Equations (3.9) are iterated until

$$\|\mathbf{K}_{n+1} - \mathbf{K}_n\| < \epsilon\|K_n\|$$

where ϵ is a predetermined constant. The time-invariant Kalman gain determined by this procedure is substituted into the optimal estimate equation (3.5) directly. Thus most time-consuming processes for equations (3.6) and (3.7) are not necessary to be

conducted.

The system matrices $\mathbf{A}$ and $\mathbf{\Gamma}$, used to determine the time-invariant Kalman gain in equation (3.9), can be constructed numerically as follows. When using the time-invariant model under no external forcing and noises, the model equation (3.1) reduces to $\mathbf{x}_{k+1} = \mathbf{A}\mathbf{x}_k$. To know the matrix form of $\mathbf{A}$ may be a difficult task especially for the nonlinear case. IF $\mathbf{x}_k$ is replaced by the j-th column of the identity matrix, A is determined from the model equation through the following steps:

(1) $\mathbf{x}_k$ is replaced by the m-th column $\mathbf{I}_{i,m}$ of the identity matrix $\mathbf{I}$.

(2) $\mathbf{x}_{k+1}$ is replaced by the m-th column $\mathbf{A}_{i,m}$ of $\mathbf{A}$, and as a result, equation is changed to

$$\mathbf{A}_{i,m} = \mathbf{A}_{i,j} \cdot \mathbf{I}_{i,m}$$

(3) By shifting m in $\mathbf{I}_{i,m}$, we can determine the matrix form of $\mathbf{A}_{i,j}$ numerically.

Note that the time step to construct $\mathbf{A}$ is equal to not the model time step but the measurement time interval because the model state is estimated every measurement cycle or assimilation cycle. The model is evolved during the period between two successive data assimilations.

The forcing matrix $\mathbf{B}$ can be constructed numerically in a manner similar to $\mathbf{A}$. If the model errors are assumed to be caused by only the external forcing, $\mathbf{\Gamma}$ is equivalent to $\mathbf{B}$. By assuming the state vector and noises are zero, the model equation (3.1) reduces to $\mathbf{x}_{k+1} = \mathbf{B}\mathbf{w}_k$. If $\mathbf{w}_k$ is replaced by the j-th column of the identity matrix, $\mathbf{B}$ is determined from the model equation through the following steps:

(1) $\mathbf{w}_k$ is replaced by the m-th column $\mathbf{I}_{i,m}$ of the identity matrix $\mathbf{I}$.

(2) $\mathbf{x}_{k+1}$ is replaced by the m-th column $\mathbf{B}_{i,m}$ of $\mathbf{B}$, and as a result, equation is changed to

$$\mathbf{B}_{i,m} = \mathbf{B}_{i,j} \cdot \mathbf{I}_{i,m}$$

(3) By shifting m in $\mathbf{I}_{i,m}$, we can determine the matrix form of $\mathbf{B}_{i,j}$ numerically.

This Chandrasekhar-type filter approach has been developed by Heemink [22, 23] to predict the coastal sea storm surge. This approach has also been operated successfully in combination with nonlinear tidal models [24]. However, the limitation due to the time-invariant Kalman gain produces a difficulty in application of this filter to variable coastal seas with strong tidal currents.

3.4 Ensemble Kalman filter

New algorithms to relax the computational burden associated with the time evolution of the error statistics have been developed in a more efficient manner. These are the so called suboptimal schemes or SOS's. An approach of the SOS proposed by Todling and Cohn [47] uses a station transition matrix of low rank to simplify the model dynamics. The reduced rank square root (RRSQRT) filter which approximates the error covariance matrix at a lower rank is introduced by Verlaan and Heemink [48]. Another approach for solving this problem is the ensemble Kalman filter (EnKF), proposed by Evensen [14]. In this section, the EnKF is focused on because it deals with the primitive equation models and as a result its computational burden is reduced drastically. The EnKF is accompanied by the Monte Carlo method which takes an ensemble of state vectors to determine the forecast state vector and the error covariance matrix. The EnKF is here described briefly, following Evensen [14] and Madsen and Canñizares [33].

When an N-size ensemble of initial states $\mathbf{x}^f_{i,k+1}$ $(i = 1, \ldots, N)$ are generated with random errors, the updating of every ensemble member may be done by using the following equation:

$$\mathbf{x}^f_{i,k+1} = \mathbf{F}(\mathbf{x}^a_{i,k}, \mathbf{w}_k + \mathbf{q}_{i,k}) \qquad \text{for} \quad i = 1, \ldots, N \tag{3.10}$$

where the model error $\mathbf{q}_{i,k}$ is generated from a set of random number with zero mean and covariance matrix $\mathbf{Q}_k$.

Evensen [14] used the ensemble mean of the state vector

$$\bar{\mathbf{x}}^f_{k+1} = \frac{1}{N}\sum_{i=1}^{N} \mathbf{x}^f_{i,k+1} \tag{3.11}$$

as its forecast. The forecast of the vector covariance matrix is obtained by using every member of the ensemble as

$$\mathbf{P}^f_{k+1} = \mathbf{S}^f_{k+1}[\mathbf{S}^f_{k+1}]^T \tag{3.12}$$

when the i-th column of $\mathbf{S}^f_{k+1}$ is expressed by

$$\mathbf{s}^f_{i,k+1} = \frac{1}{\sqrt{N-1}}(\mathbf{x}^f_{i,k+1} - \bar{\mathbf{x}}^f_{k+1}) \tag{3.13}$$

In the EnKF algorithm, the measurement data should be regarded as random variables, so it is reasonable to add random errors to the measurement data. In no addition of random errors to the measurement data, the error covariance matrix described by equation (3.13) becomes very small with only numerical errors [2]. The ensemble of measurement data is obtained from

$$\mathbf{y}_{i,k+1} = \mathbf{y}_{k+1} + \epsilon_{i,k+1} \qquad \text{for} \quad i = 1, \ldots, N \tag{3.14}$$

where $\epsilon_{i,k+1}$ is the measurement error which has a zero mean and known covariance matrix $\mathbf{R}_{k+1}$.

All ensemble members of the state vector are updated through the following equation:

$$\mathbf{x}^a_{i,k+1} = \mathbf{x}^f_{i,k+1} + \mathbf{K}_{k+1}(\mathbf{y}_{i,k+1} - \mathbf{E}_{k+1}\mathbf{x}^f_{i,k+1}) \qquad \text{for} \quad i = 1, \ldots, N \tag{3.15}$$

The Kalman gain $\mathbf{K}_{k+1}$ is determined by substituting the error covariance matrix of equation (3.12) into equation (3.6).

3.5 Summary and discussion

The Kalman filter technique is an intelligent method which can consider the time evolution by the dynamic model and the optimal fitting between the model and measurement over the observation domain. However, huge computational time is needed to estimate the error covariance matrix included in the calculation of the Kalman gain. Two kinds of the approximated Kalman gain filters, proposed to reduce the computational time, are discussed in this chapter. As for the time-invariant Kalman gain based on the Chandrasekhar-type algorithm, computational time is saved so much, but not applicable to the coastal seas with variable temperature and current velocity fields generated by strong tidal currents. Strong nonlinearity in the current velocity fields is not well described by this technique. The EnKF technique is proposed as the best method of data assimilation applicable to the coastal seas with strong nonlinearities.

CHAPTER 4

COMPUTER SIMULATION OF THE CAT

4.1 Introduction

The ocean acoustic tomography is separated into two parts as temperature and velocity tomographies according to the object of observation. The temperature tomography converts the measured travel times of one-way transmitted sounds or the mean of travel times for the reciprocally transmitted sounds into temperature fields. The differential travel times between the reciprocally transmitted sounds, inverted into current fields, are used for velocity tomography. In contrast to temperature tomography, which needs precise positioning accuracy, precise clock accuracy is required for the velocity tomography [38].

After the first proposition of acoustic tomography scheme for oceanic measurement by Munk and Wunsch [39] the ocean acoustic tomography has taken rapid development as a modern technology to monitor three-dimensional mesoscale temperature structures in the ocean (e.g. [19, 8, 5, 7, 9, 30, 42, 37, 17, 50]). The possibility of water velocity monitoring through sound transmission was demonstrated in the midocean region on a 300km scale in 1983 [26], and on a 1000km scale in 1987 [10]. However, no the three-dimensional monitoring of velocity structures is attempted because only two or three acoustic stations were deployed in those field experiments.

A velocity tomography experiment with five stations was done in the south of the Gulf Stream meandering region [3]. The wave-like energy flux radiated southward from the Gulf Stream meander was well estimated at different depth layers, but the

velocity structure of cold rings separating from it was not imaged due to the failure of data recording at one station. A computer simulation of velocity tomography was carried out by Gaillard [16] who used a quasi-geostrophic ocean model with mesoscale variabilities. The barotropic and baroclinic velocity fields described in terms of the stream function were the targets of inverse analysis. The reconstruction of velocity fields was worse for the barotropic mode than for the baroclinic modes, although the reason for this was not well clarified.

As described in chapter 2, the conventional inverse method used in midocean acoustic tomography for mapping temperature and velocity fields is based on stochastic inversion, which requires statistical information on both solution fields and data error. However,tidal currents in the coastal seas are extremely variable at each tidal phase and sometimes induce two-dimensional vortices [45]. In such complicated situations it is unlikely that sufficient statistical information on the solution field can be obtained. Further simplification of inversion is required for the reconstruction of tidal currents in the coastal seas.

There is a prominent difference between the deep acoustic tomography (DAT) and coastal acoustic tomography (CAT). In the coastal seas, current velocity fields are strongly influenced by complicated shorelines. The first step of velocity field inversion for CAT is done similarly to DAT by using travel time data obtained for the ray paths which cross the interior of the observation region. At the next step, the inversion result is modified to satisfy the boundary conditions at the shorelines. This modification is effective especially for the near-shore region.

This chapter is concerned with the acoustic tomography of barotropic or depth-averaged tidal vortices distributed in the coastal sea model. The main purpose of this chapter is to develop a simple inversion method applicable to the acoustic tomography of two-dimensional current fields in the coastal seas. Vortex fields induced by strong tidal currents around straits, islands and peninsulas may be the best targets for this study because of their two-dimensionality. The feasibility test of this simple method

is performed through computer simulation.

Two methods are examined to consider the boundary condition at the coastline. In the first method, current fields are corrected to satisfy the boundary condition after the inversion (Chapter 4.5). In the second method, the stream function is put zero at the coastlines prior to the inversion (Chapter 4.6). In addition, the coordinate transformation by using the boundary-fitted curvilinear grid generation technique is introduced to make the above two methods applicable to the coastal seas with complicated coastlines (Chapter 4.7).

4.2 Tidal vortex model

For the simulation of CAT the vortex fields induced by strong tidal currents are constructed by a two-dimensional spectral model. The model fields are described by the stream function Ψ alone.

The most important parameter in understanding the performance of tomography is a spatial resolution of inversion. This can be easily examined by distributing two-dimensional vortices of various sizes in the tomography domain. To distribute tidal vortices with expected strengths and sizes in the model domain, the wavenumber spectrum of the stream function is given in the following form:

$$\begin{aligned} S_{kl} &= S_0 \Bigg[a \exp\Big\{ -(\frac{K-k_1}{\sigma})^2 \Big\} + b \exp\Big\{ -(\frac{K-k_2}{\sigma})^2 \Big\} \\ &+ c \exp\Big\{ -(\frac{K-k_3}{\sigma})^2 \Big\} + d \exp\Big\{ -(\frac{K-k_4}{\sigma})^2 \Big\} \Bigg] \exp(i\Theta_{kl}) \end{aligned} \tag{4.1}$$

where $K = \sqrt{k^2 + l^2}$ (k and l are the horizontal components of wave number), S_0 is the amplitude, Θ_{kl} the random phase function and σ the spectral width. The maximum wave number K is 21 and the model domain is divided into 64×64 grid points. Each component of the above spectrum shows peaks at wave numbers $k1$, $k2$, $k3$ and $k4$, which are determined as 2, 3, 4 and 5, respectively. The spectral

width σ is given 0.3. The magnitude of each spectral component is weighted with the parameters a, b, c and d. To test the performance of the inverse method, these parameters are examined for three cases with tidal vortices of different size. The variable spectral peaks and random phases make it possible to construct expected vortex fields in the model domain. The tomographic experiment is conducted in the 5km×5km area located in the center of this model domain (Figure 4.1).

4.3 Forward problem and inverse analysis

4.3.1 Forward problem

As the coastal sea is modeled by a stream function which provides no information on temperature, the sea is assumed to be homogeneous. In this situation, the ray paths of sound are refracted by the vertical variation of sound velocity due to the pressure and the vertical shear of water flow. In the coastal seas, ray paths can also be reflected by the sea surface and bottom. The complicated ray paths in the vertical section can be projected onto the horizontal section in the analysis. The horizontal refraction of ray paths due to the horizontal variation of sound velocity and the horizontal shear of water flow is negligible in comparison with the refraction in the vertical section. As a result, we can plot all ray paths as straight, horizontal lines. Furthermore, the vertical component of velocity is assumed to be very small compared to the horizontal ones and is thus not considered in this study.

The travel time t_i along the i-th ray path Γ_i in the two-dimensional flow field $\mathbf{u}(x, y)$ is determined from the following path integral equation:

$$t_i = \oint_{\Gamma_i} \frac{\mathrm{d}s}{C_0 + \mathbf{u}(x, y) \cdot \mathbf{n}} \tag{4.2}$$

where C_0 is the reference sound speed, $\mathbf{n}$ the unit vector tangent to the i-th ray and s the arc length along the i-th ray path. Equation (4.2) is nonlinear and can be

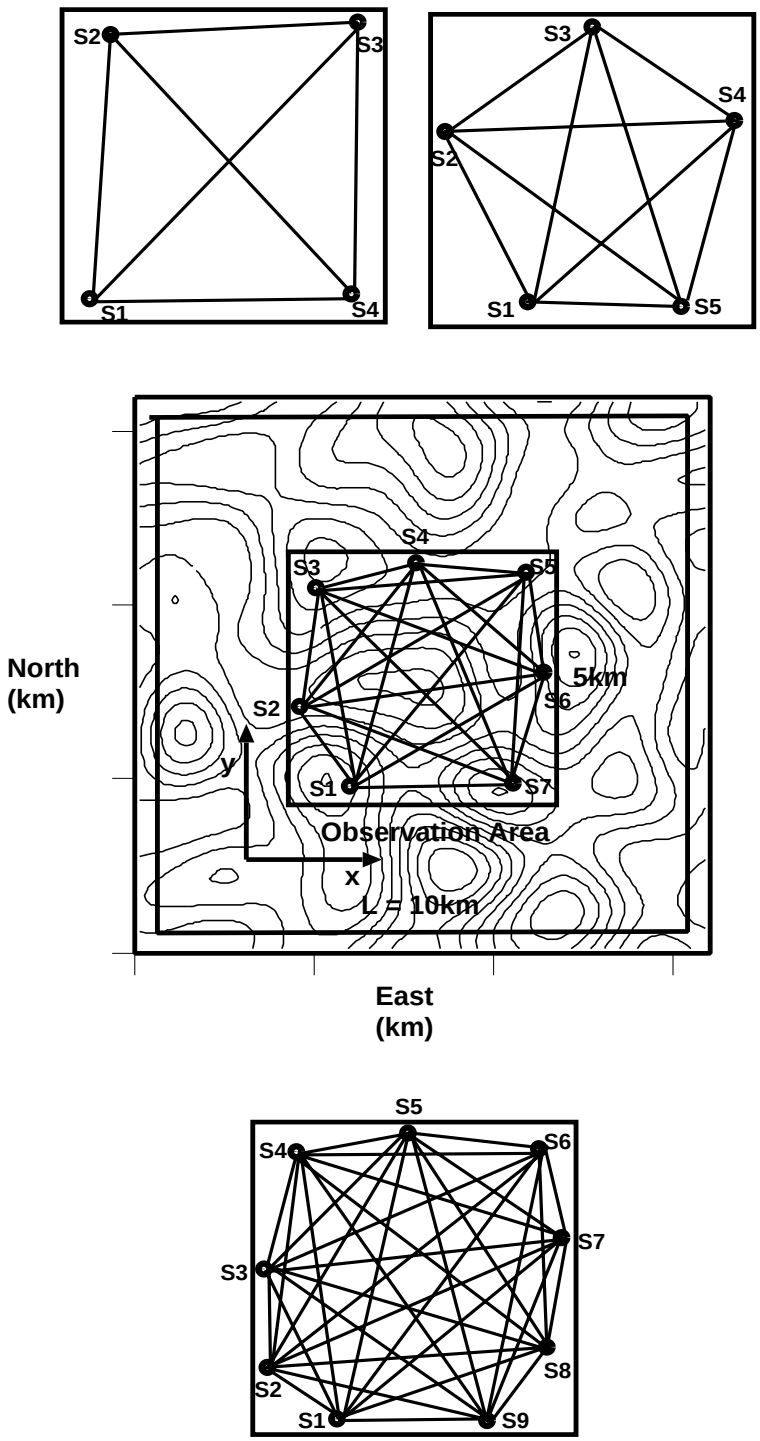

Figure 4.1: Model domain and the configuration of seven acoustic stations superimposed on the stream function field. The configurations for four, five and nine stations are indicated above and below of the model domain, respectively. S1-S9 are the name of stations.

linearized by considering $C_0 >> \mathbf{u}(x,y)\cdot\mathbf{n}$. After the linearization, Γ_i is replaced by the ray path Γ_{0i} for C_0. The travel time difference Δt_i for the reciprocal transmission between two acoustic stations is expressed by

$$\Delta t_i = \frac{1}{2}(t_i^+ - t_i^-) = -\oint_{\Gamma_{0i}} \frac{\mathbf{u}(x,y)\cdot\mathbf{n}}{C_0^2} ds \tag{4.3}$$

where the superscripts + and − denote the opposite directions of sound transmission [38]. In the field experiment, Δt_i is not error-free and is usually contaminated by travel time errors due to the movement of acoustic stations, the interference of sound waves with the sea surface and bottom, and so on. In our simulation experiments, random errors are introduced in the simulated travel time data instead of the above *in situ* travel time errors.

4.3.2 Inverse analysis

The inverse analysis is used to determine the unknown depth-averaged velocity field $\mathbf{u}(x,y)$ from the travel time difference data Δt_i in equation (4.3). The $\mathbf{u}(x,y)$ in equation (4.3) is further examined to make the inversion efficient. The two-dimensional vector field $\mathbf{u}$ may be decomposed into

$$\mathbf{u} = \mathbf{u}_\Psi + \mathbf{u}_\Phi \tag{4.4}$$

where $\mathbf{u}_\Psi$ is the solenoidal vector field and $\mathbf{u}_\Phi$ the nonrotational vector field. On a horizontal plane (x,y) these are expressed by

$$\mathbf{u}_\Psi = \nabla\times(-\Psi\hat{z}) = \Big(-\frac{\partial\Psi}{\partial y}, \frac{\partial\Psi}{\partial x}\Big) \tag{4.5}$$

$$\mathbf{u}_\Phi = \nabla\Phi = \Big(\frac{\partial\Phi}{\partial x}, \frac{\partial\Phi}{\partial y}\Big) \tag{4.6}$$

where $\hat{z}$ is the unit vector in the vertical direction, Ψ the stream function and Φ the velocity potential with no relative vorticity. Here notice that according to the projection slice theorem, the nonrotational component of current fields due to tidal sea level changes and bottom topography has no influence on the tomography result expressed by the stream function [38]. This means that acoustic tomography measurements have the ability to measure only the solenoidal vector field. In section 4.5, the projection slice theorem will be discussed in detail.

Introduction of stream function halves the number of unknown variables in the inverse analysis. We shall here expand $\Psi(x, y)$ into a truncated Fourier series:

$$\Psi(x,y) = \sum_{k=0}^{N}\sum_{l=0}^{N}\{A_{kl}\cos\gamma_0(kx+ly) + B_{kl}\sin\gamma_0(kx+ly)\} \tag{4.7}$$

where A_{kl} and B_{kl} are the unknown coefficients and $\gamma_0 = 2\pi/L$. L (= 10km) is the side length of the square inversion domain, which is taken as twice that of the observation area to avoid the effect of periodicity (Fig. 1). N is taken as 4 (2.5km/cycle) in consideration of the number of unknown coefficients and the size of resolvable vortices. Equation (4.7) then reduces to

$$\Psi(x,y) = \sum_{j=1}^{(N+1)^2} P_j Q_j(x,y) \tag{4.8}$$

where

$$\mathbf{P} = [A_{00}, B_{00}, A_{01}, B_{01}, \ldots, A_{NN}, B_{NN}]$$

and

$$\mathbf{Q}(x,y) = [1, 0, \cos\gamma_0 y, \sin\gamma_0 y, \ldots, \cos\gamma_0(Nx+Ny), \sin\gamma_0(Nx+Ny)]$$

Substituting equation (4.8) into (4.3), we obtain

$$\Delta t_i = \sum_{j=1}^{(N+1)^2} P_j \int_0^{R_i} \frac{\frac{\partial}{\partial y} Q_j(x,y) - \frac{\partial}{\partial x} Q_j(x,y) \tan\phi_i}{C_0^2} \mathrm{d}x \tag{4.9}$$

where ϕ_i is the angle between the eastward x-axis and the i-th ray path, and R_i the distance between two stations measured along the x-axis. Equation (4.9) can be rewritten in matrix form as

$$\mathbf{y} = \mathbf{E}\mathbf{x} + \mathbf{e} \tag{4.10}$$

where

$$\begin{aligned} \mathbf{y} &= [\Delta t_1, \Delta t_2, \Delta t_3, \ldots, \Delta t_{N_r}] \\ E_{ij} &= \int_0^{R_i} \frac{\frac{\partial}{\partial y} Q_j(x,y) - \frac{\partial}{\partial x} Q_j(x,y) \tan\phi_i}{C_0^2} dx \\ \mathbf{x} &= \mathbf{P}^T \end{aligned}$$

The $\mathbf{e}$ denotes the observational errors, added to the travel time differences as random errors. There is another source of error due to the inadequacies of the model which cannot describe vortex fields with length scales smaller than the spatial resolution of the tomography array due to a limited number of stations and the truncated wavenumber in the Fourier expansion. This error may also influence the performance of inversion.

Since the number of unknown parameters $\mathbf{x}$ to be estimated by inversion is greater than the number of data $\mathbf{y}$, the problem is underdetermined. The stochastic inverse method is applied to obtain the optimum estimate of $\mathbf{x}$ [38]. The expected uncertainty, the difference between the true value of $\mathbf{x}$ and its estimate $\hat{\mathbf{x}}$, becomes as shown in (2.24). From the condition that makes the diagonal component of $\mathbf{P}$ minimum, the

optimal estimate $\hat{\mathbf{x}}$ can be obtained as shown in (2.33) by

$$\hat{\mathbf{x}} = \mathbf{R}_{xx}\mathbf{E}^T(\mathbf{E}\mathbf{R}_{xx}\mathbf{E}^T + \mathbf{R}_{ee})^{-1}\mathbf{y} \tag{4.11}$$

Each component of $\mathbf{R}_{xx}$ and $\mathbf{R}_{ee}$ can be specified when sufficient statistical information on current fields is available [38]. Given the limited information, we shall assume that all the components of $\mathbf{R}_{xx}$ and $\mathbf{R}_{ee}$ possess the following constant values σ_{xx}^2 and σ_{ee}^2, respectively:

$$\mathbf{R}_{xx} = \sigma_{xx}^2\mathbf{I}, \qquad \mathbf{R}_{ee} = \sigma_{ee}^2\mathbf{I} \tag{4.12}$$

where $\mathbf{I}$ is the unit matrix. When putting $\alpha^2 = \sigma_{ee}^2/\sigma_{xx}^2$, $\hat{\mathbf{x}}$ reduces to

$$\hat{\mathbf{x}} = \mathbf{V}[\mathbf{\Lambda}^T\mathbf{\Lambda} + \alpha^2\mathbf{I}]^{-1}\mathbf{\Lambda}^T\mathbf{U}\mathbf{y} \tag{4.13}$$

where $\mathbf{E} = \mathbf{U}\mathbf{\Lambda}\mathbf{V}^T$ is given from the singular value decomposition of the coefficient matrix $\mathbf{E}$. The inversion in the form of equation (4.13) is called the ridge regression [25] and also the damped least squares method [36].

4.3.3 The L-curve method

The next step is to determine the optimum value of the weighting factor α^2. On the basis of the Gauss-Markov theorem the covariances $\mathbf{R}_{xx}$ and $\mathbf{R}_{ee}$ must be given as *a priori* statistical information. However, the covariance of the solution field $\mathbf{R}_{xx}$ is generally unavailable for tidal vortex fields, which are variable at each tidal period.

The α^2 is the weighting factor to minimize the magnitude of $\|\mathbf{x}\|$ in balance with that of $\|\mathbf{y} - \mathbf{E}\mathbf{x}\|$. Equation (4.13) can be rewritten

$$\hat{\mathbf{x}} = \sum_{i=1}^{N_r} \frac{\lambda_i(\mathbf{u}_i^T\mathbf{y})}{\lambda_i^2 + \alpha^2}\mathbf{v}_i \tag{4.14}$$

where $\mathbf{u}_i$ and $\mathbf{v}_i$ are the eigenvectors in the observation and the model spaces, respec-

tively. The $\mathbf{u}_i$ and $\mathbf{v}_i$ has the following relationships with $\mathbf{U}$ and $\mathbf{V}$

$$\mathbf{U} = (\mathbf{u}_1, \mathbf{u}_2, \cdots, \mathbf{u}_{N_r})$$
$$\mathbf{V} = (\mathbf{v}_1, \mathbf{v}_2, \cdots, \mathbf{v}_{N_r})$$

The λ_i are the eigenvalues comprising the diagonal components of Λ. Equation (4.14) tells us that the solution $\hat{\mathbf{x}}$ becomes insensitive to α^2 for $\lambda_i > \alpha^2$ and the influence of λ_i on $\hat{\mathbf{x}}$ is damped for $\lambda_i < \alpha^2$. There are a number of references in the literature on the method to obtain the best selection of α^2. The L-curve method recently developed by Hansen and O'leary [21] is chosen as a simple, reliable one. The L-curve is a plot in the $(\zeta(\alpha), \xi(\alpha))$ plane, where parameters $\zeta(\alpha)$ and $\xi(\alpha)$ are the size of estimated error and solution. The idea understanding this method is that the optimum value of α^2 is given as a point where the curvature of the concave L-curve becomes a maximum, making both the size of estimated error and solution as small as possible in balance. For the L- curve continuously differentiable up to the second order, its curvature $\kappa(\alpha)$ is defined as

$$\kappa(\alpha) = \frac{\zeta'\xi'' - \zeta''\xi'}{\left\{(\zeta')^2 + (\xi')^2\right\}^{3/2}} \tag{4.15}$$

where the superscript $'$ means differentiation with respect to α. Without having *a priori* statistical information on the solution field and data, the optimum value of α^2 can be determined by this method.

4.3.4 Derivatives of the L-curve

It is possible to show that the L-curve always have an L-shape structure. From equation (4.14) the $\hat{\mathbf{x}}^T\hat{\mathbf{x}}$ and $(\mathbf{y} - \mathbf{E}\hat{\mathbf{x}})^{\mathbf{T}}(\mathbf{y} - \mathbf{E}\hat{\mathbf{x}})$ can be obtained

$$\xi = \hat{\mathbf{x}}^T\hat{\mathbf{x}} \;\; = \;\; \sum_{i=1}^{N_r} \frac{\lambda_i^2\beta^2}{(\lambda_i^2 + \alpha^2)^2} \tag{4.16}$$

$$\zeta = (\mathbf{y} - \mathbf{E}\hat{\mathbf{x}})^{\mathbf{T}}(\mathbf{y} - \mathbf{E}\hat{\mathbf{x}}) \quad = \quad \sum_{i=1}^{N_r} \frac{\alpha^4 \beta^2}{(\lambda_i^2 + \alpha^2)^2} \tag{4.17}$$

,respectively, where $\beta = \mathbf{u}_i^T \mathbf{y}$. The derivative of ζ and ξ with respective to α become

$$\frac{d\zeta}{d\alpha} \quad = \quad \sum_{i=1}^{N_r} \frac{2\alpha|\beta|\lambda_i^2}{(\lambda_i^2 + \alpha^2)^2} \tag{4.18}$$

$$\frac{d\xi}{d\alpha} \quad = \quad \sum_{i=1}^{N_r} \frac{-2\alpha|\beta|\lambda_i}{\lambda_i^2 + \alpha^2} \tag{4.19}$$

Thus

$$\frac{d\xi}{d\zeta} = -\left(\frac{\sum_{i=1}^{N_r} \frac{\lambda_i}{\lambda_i^2 + \alpha^2}}{\sum_{i=1}^{N_r} \frac{\lambda_i^2}{(\lambda_i^2 + \alpha^2)^2}} \right) \tag{4.20}$$

Therefore the calculation result of equation (4.20) is always negative, so that the size of the solution ξ becomes smaller as the size of the estimated error ζ increases. As a result, the slope of the L-curve is always negative. The second derivative of ξ with respective to ζ is evaluated as follows:

$$\frac{d}{d\alpha}\frac{d\alpha}{d\zeta}\frac{d\xi}{d\zeta} = \frac{\sum_{i=1}^{N_r} \frac{\lambda_i^4 - 3\alpha^2\lambda_i^2}{(\lambda_i^2 + \alpha^2)^3}}{2\alpha^2|\beta|\Big(\sum_{i=1}^{N_r} \frac{\lambda_i^2}{(\lambda_i^2 + \alpha^2)^2}\Big)^2} \cdot \frac{\sum_{i=1}^{N_r} \frac{\lambda_i}{\lambda_i^2 + \alpha^2}}{\sum_{i=1}^{N_r} \frac{\lambda_i^2}{(\lambda_i^2 + \alpha^2)^2}} \tag{4.21}$$

Equation (4.21) shows that the L-curve is downward convex if $\sum_{i=1}^{N_r} \lambda_i^4 - 3\alpha^2\lambda_i^2$ is positive. This is a critical condition to make the L-curve method valid. This condition provides the upper limit of α

$$\alpha < \frac{\lambda_{max}}{\sqrt{3}}$$

where λ_{max} is the maximum eigenvalue. As the major role of α in the damped least squares scheme is to reduce the effect of quite small eigenvalues on the solution, α

should be greater than the minimum eigenvalue. Thus, $\sum_{i=1}^{N_r} \lambda_i^4 - 3\alpha^2\lambda_i^2$ is positive and the resulting L-curve is downward convex, drawing a L-shaped curve.

4.3.5 Evaluation of the inversion result

The inversion result obtained by the computer simulation is evaluated by calculating a correlation coefficient between the model stream function Ψ_m and the reconstructed stream function $\hat{\Psi}_r$:

$$\rho = \frac{\sum_{m=1}^{N_g} \Psi_m \cdot \hat{\Psi}_r}{\sqrt{\sum_{m=1}^{N_g} \Psi_m^2} \cdot \sqrt{\sum_{m=1}^{N_g} \hat{\Psi}_r^2}} \tag{4.22}$$

where N_g ($= 900$) is the number of grid points in the tomography domain. The spatial resolution ΔR of the tomography system is determined by the number of ray paths covering the observation region and may be defined as

$$\Delta R = \sqrt{\frac{A}{M}}$$

where A is the area of the tomography domain and M the number of the ray path. The number of terms for the truncated Fourier expansion should be determined fitting to ΔR.

4.4 Computer simulation

4.4.1 Experiments with different station numbers and error levels

The computer simulation of CAT has been conducted for four cases with four, five, seven and nine stations (hereafter Cases I, II, III and IV, respectively), in which the ocean model domain is surrounded adequately by the acoustic stations (Figure 4.1). ΔR is estimated as 4.2km, 2.5km, 1.2km and 0.8km for Cases I, II, III and IV,

respectively. The conditions of computer simulation for each case are presented in Table 1.

Table 4.1: Conditions of the simulation experiments for each case.

\		Station Num.	Ray Num.	ΔR(km)	Random Err.	α	ρ
Case I		4	6	12.2	st.	0.3	0.410
Case II		5	10	9.5	st.	0.3	0.803
Case III	-A	7	21	6.6	st.$\times$ 1/2	0.44	0.900
	-B				st.	0.74	0.887
	-C				st.$\times$ 3/2	1.01	0.867
	-D				n.e.	0.1	0.914
	-E				st.	0.1	0.677
Case IV		9	36	5.0	st.	0.62	0.922
Case V	-A	7	21	6.6	st.	0.59	0.854
	-B				st.	1.33	0.534

For these four cases, the model vortex fields are constructed by putting $a = 1.0$, $b = 0.7$, $c = 0.5$ and $d = 0.3$ in equation (4.1). The quality of vortex fields reconstructed by the inverse analysis, of course, depends on the configuration of acoustic stations, even given the fixed number of stations. In this paper, close attention is focused on the number of stations rather than their configuration. Thus only one configuration of stations is examined for each case, in which the sides of the polygonal domain are taken as almost the same length.

No tomography experiments in the sea are error-free, so random errors should be added to evaluate the performance of inversion. Random errors produced by multiplying random numbers by the Gaussian distribution of a standard deviation $2\pi \times 0.017$ms are added to the travel time differences obtained in the simulation. We shall call these random errors the standard error level. To clarify the effect of the random errors on the inversion, Case III with seven acoustic stations is further divided into four cases; Cases III-A, -B and -C are the cases in which random errors are produced by multiplying the random numbers by 1/2, 1 and 3/2, respectively. Case III-D is the error-free case.

Figures 4.2a, b, and c show the L curves, the κ - α plots and the ρ - α plots for

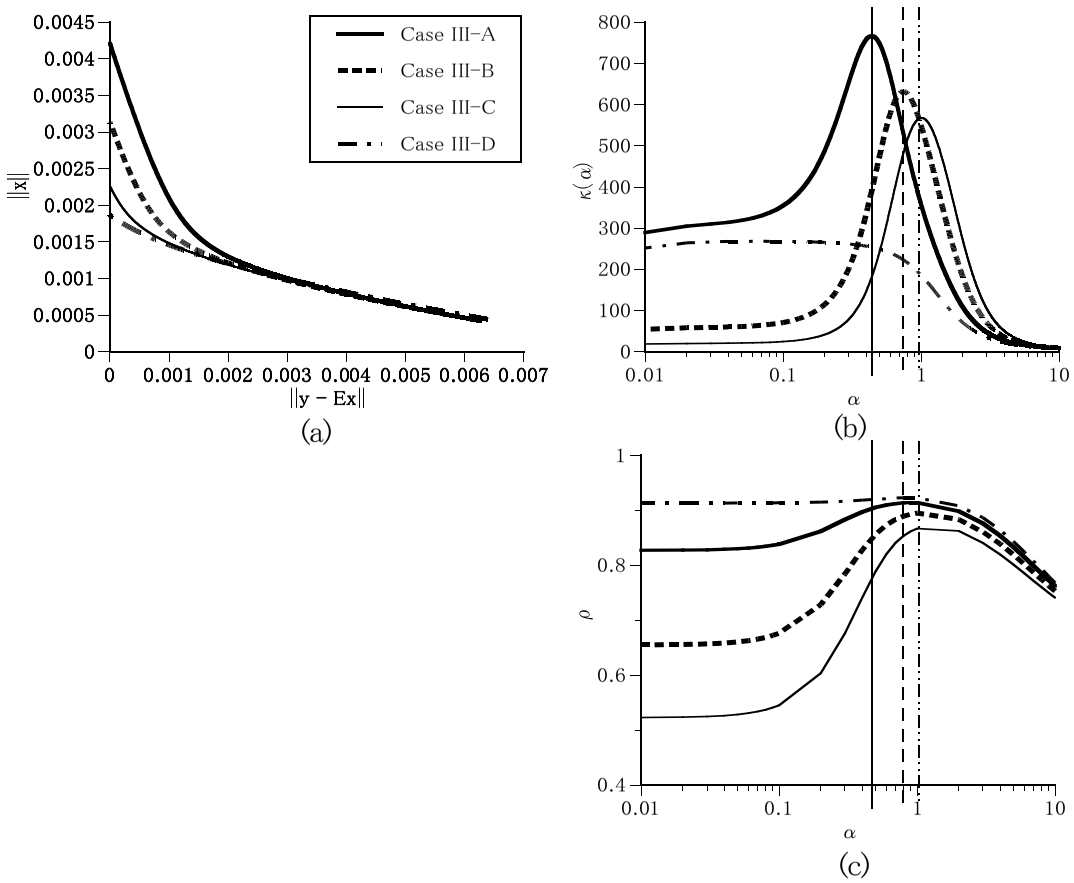

Figure 4.2: (a) L curves, (b) κ curves and (c)ρ curves obtained for Cases III-A, -B, -C and -D, respectively. The κ and ρ are plotted against α and the vertical lines point the peaks on the κ curves.

Cases III-A, -B, -C and -D, respectively, characterized according to the fixed number of stations and the different levels of random errors. For Cases III-A, -B and -C with random noise, the L curve has a fold near $\|\mathbf{y} - \mathbf{Ex}\| = 0.001$, in contrast to the L curve for Case III-D, which is nearly flat in the range $\|\mathbf{y} - \mathbf{Ex}\| < 0.001$ (Figure 4.2a). As expected, corresponding steep peaks appear in the κ - α plots for the first three cases, while κ is nearly constant at $\alpha < 0.4$ for the fourth case (Figure 4.2b). The peak positions are shifted to the smaller side of α with decreasing random errors as expected. Peaks also exist in the ρ - α plots for the first three cases (Figure 4.2c),

although the peak positions are not the same as those for the κ - α plots. The steepness of the peaks decreases with decreasing random error and is zero for the error-free case. The optimum value of α may be determined as a peak position on the κ curve because the ρ curve cannot be obtained in the field experiment. At the peak positions of $\alpha = 0.44$, 0.74 and 1.01, the values of ρ are estimated as 0.900, 0.887 and 0.867 for Cases III-A, -B and -C, respectively. These satisfactory values of ρ are found because the ρ curves are flat around the corresponding peaks. For Case III-D (error-free), the optimum inversion is obtained for any α smaller than 0.4 where the κ curve is nearly horizontal.

The L, κ and ρ curves for Cases I, II and IV with different numbers of stations and the standard error level are shown in Figure 4.3. Except for Case IV, with nine stations, there are no clear folds in the L curves (Figures 4.3a and b). As expected, a steep peak placed at $\alpha = 0.62$ is seen on the κ curve for Case IV (Figure 4.3c). The value of ρ reaches a large value of 0.922 at $\alpha = 0.62$ and maintains values greater than 0.9 over the wide range of $0.1 < \alpha < 2.0$. For Cases I and II, any values of α smaller than 1.0 are selectable. According to equation (4.14), these results are expected when $\lambda >> \alpha$. However, the inversion results are so bad, especially for Case I, because of the insufficient number of stations.

A tidal vortex field prepared for the computer simulation is shown in Figure 4.4 with the contour plot of the stream function. A cyclonic vortex with a diameter of about 15km is located at the middle of the domain, surrounded by four smaller diameter anticyclonic vortices. The upper panel of Figure 4.5a shows the contour plot of the stream function for Case III-B, obtained by the computer simulation in which the optimum value of α is used. The contour plot of the difference between the model and reconstructed stream functions is also shown at the lower panel of the figure. The overall feature of the vortices is well reconstructed, although the shape of the central vortex is horizontally less elongated than that of the model stream function field. The smallest anticyclonic vortex at the upper right is shifted lower and is spread

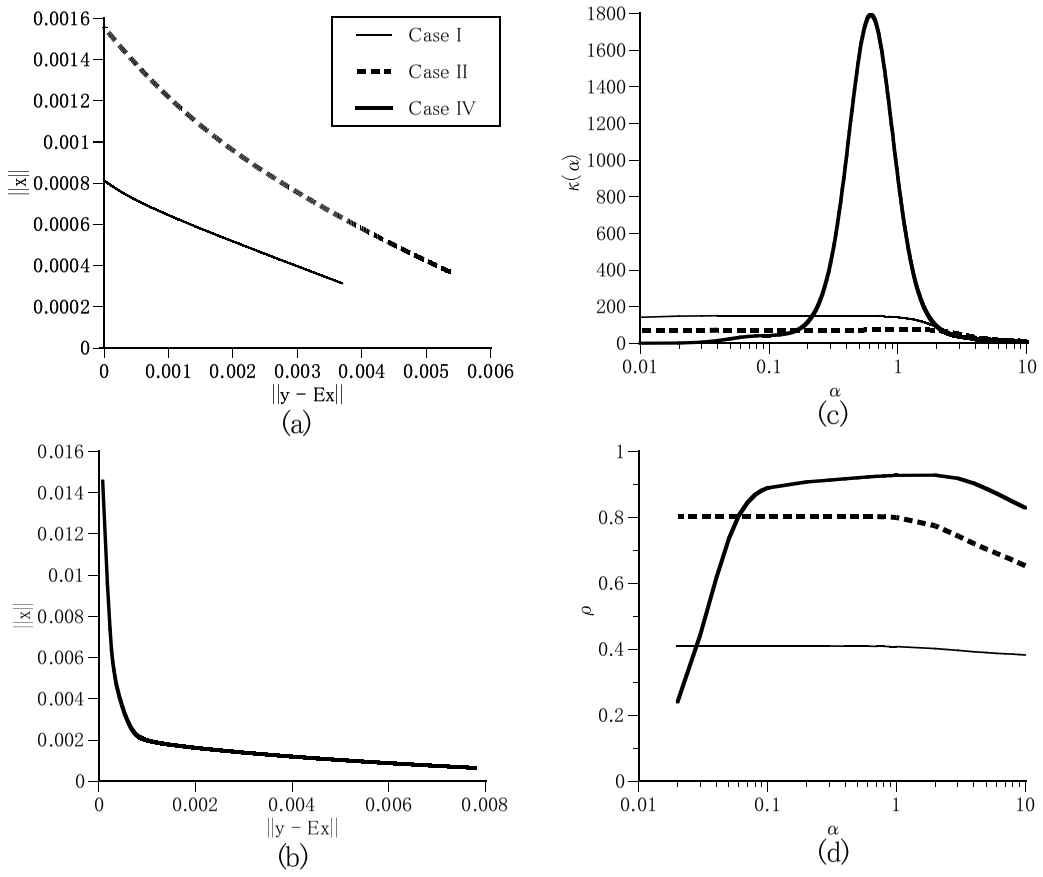

Figure 4.3: (a), (b) L curves, (c)κ curves and (d)ρ curves obtained for Cases I, II and IV, respectively. The κ and ρ are plotted against α.

more than in the model. There is a significant difference at the central part on the left side of the figure. The correlation coefficient ρ is estimated as 0.887. To clarify the effect of α, an inverse analysis for Case III-E is done with the inadequate α value of 0.1. Other conditions except α are fixed the same as those for Case III-B. The result for Case III-E is shown in Figure 4.5b. The model vortex field is quite poorly reconstructed and differences between both the stream functions are large in most of the domain. For this case, ρ is estimated as 0.677. This poor quality of inversion is caused by the inadequate choice of α, so determining the optimum value of α by the L-curve method is understood as a critical step in the present inversion.

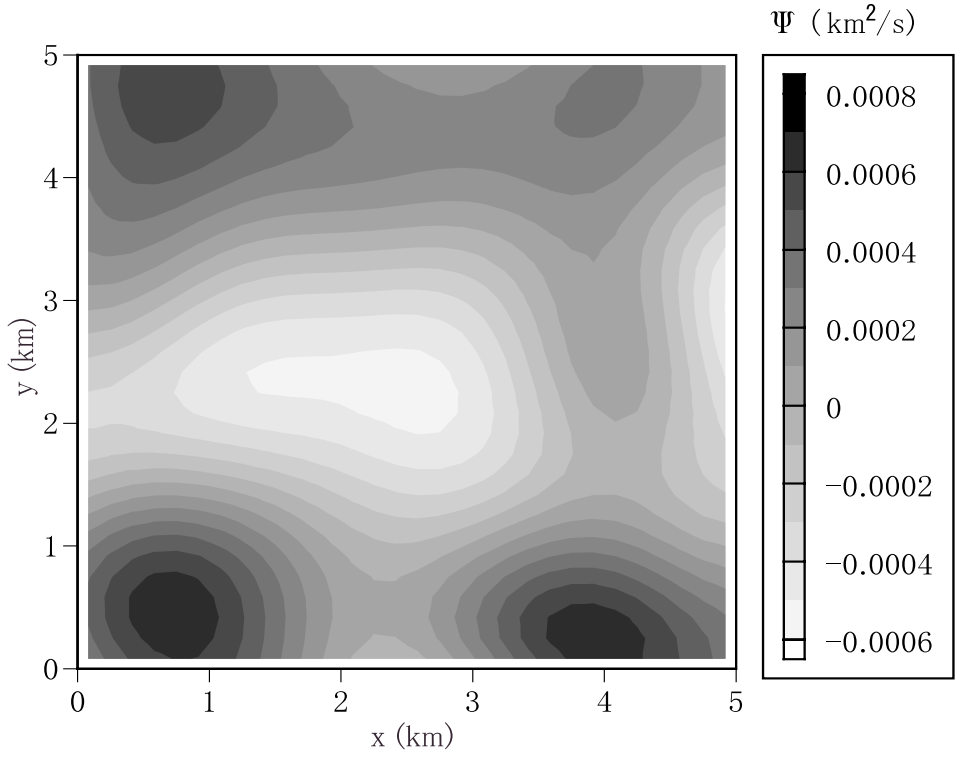

Figure 4.4: Contour plot of the stream function for the model vortex field constructed by putting $a = 1.0$, $b = 0.7$, $c = 0.5$ and $d = 0.3$ inequation (4.1).

The inversion results for Cases I, II and IV are shown in Figures 4.6a, b and c, respectively. The four stations in Case I are too few for the vortex field to be reconstructed. The inversion result is greatly improved for Case II with five stations, but the size of the central cyclonic vortex is considerably smaller than that of the model vortex field. The best agreement with the model vortex field is attained for Case IV with nine stations. The ρ value is estimated as 0.410, 0.803 and 0.922 for Cases I, II and IV, respectively.

4.4.2 Experiments with different vortex fields and standard error level

Tidal vortex fields generated in the coastal seas are highly variable during a tidal period. We examine the performance of the present inverse method for various vortex

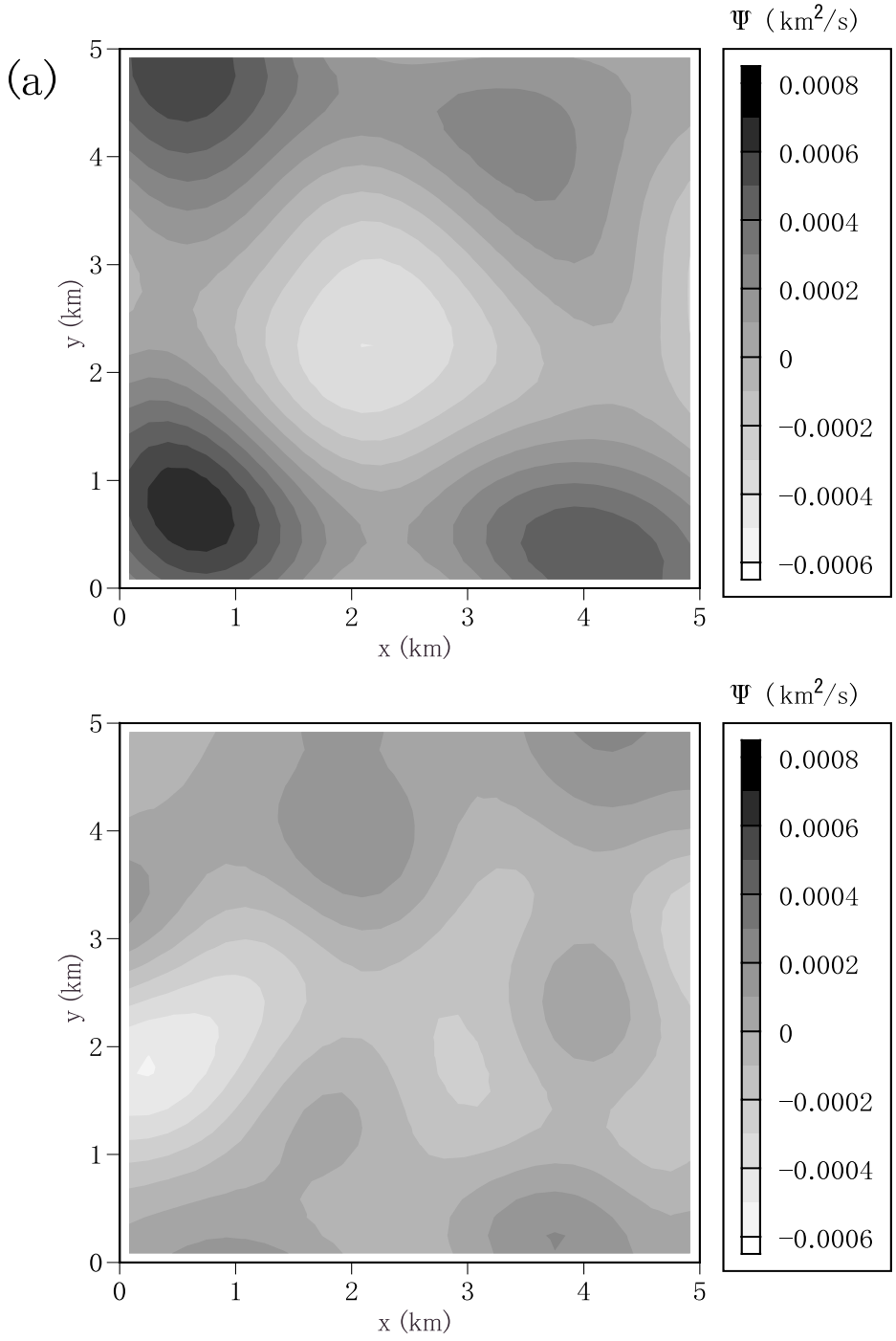

Figure 4.5: Contour plots of the stream function for the reconstructed vortex fields in (a) Case III-B and (b) Case III-E. The differences between the model and reconstructed vortex fields are presented at the lower panel of the figures.

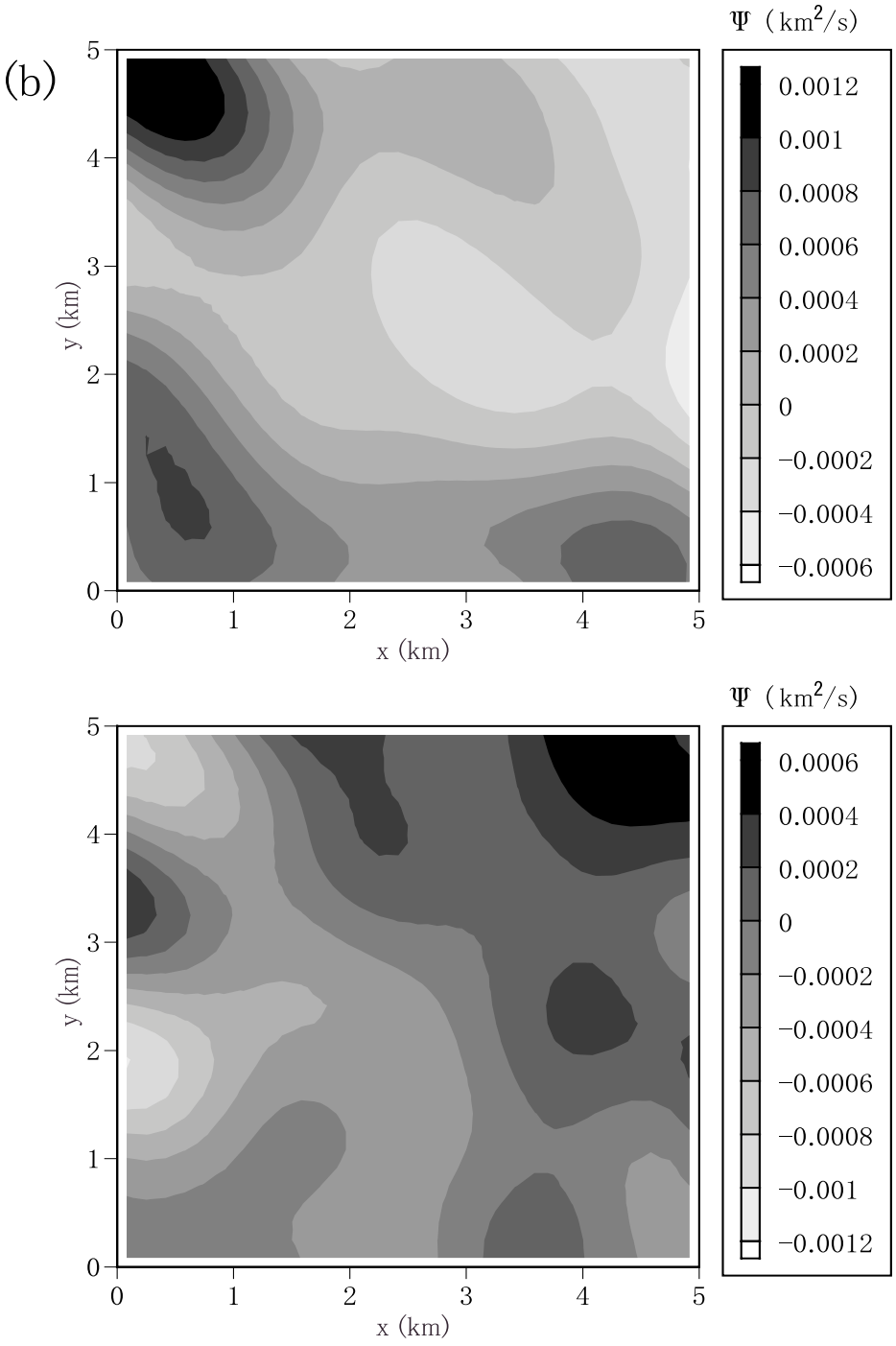

Figure 4.5: (Continued)

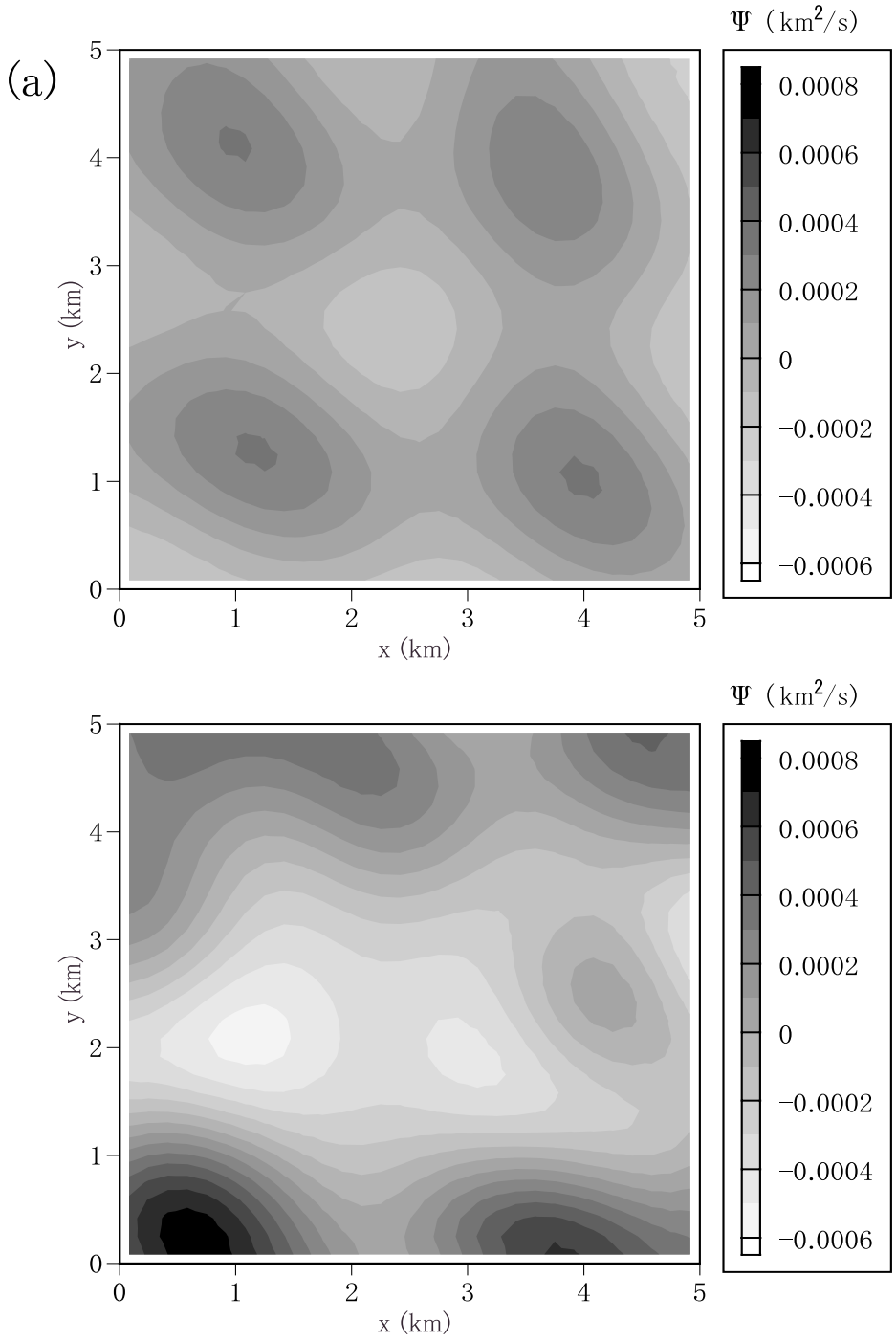

Figure 4.6: Contour plots of the stream function for the reconstructed vortex fields in (a) Case I, (b) Case II and (c) Case IV. The differences between the model and reconstructed vortex fields are presented at the lower panel of the figures.

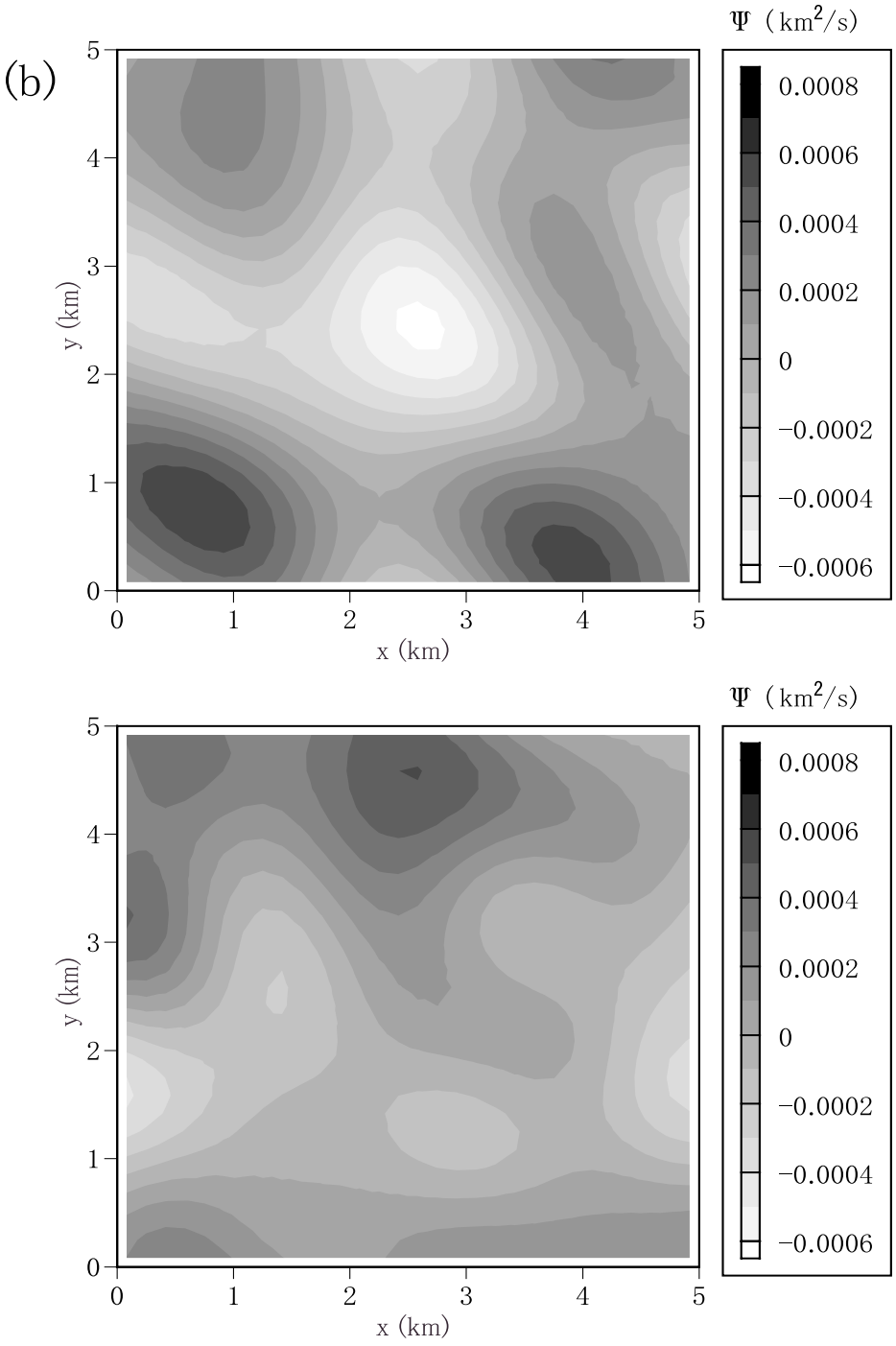

Figure 4.6: (Continued)

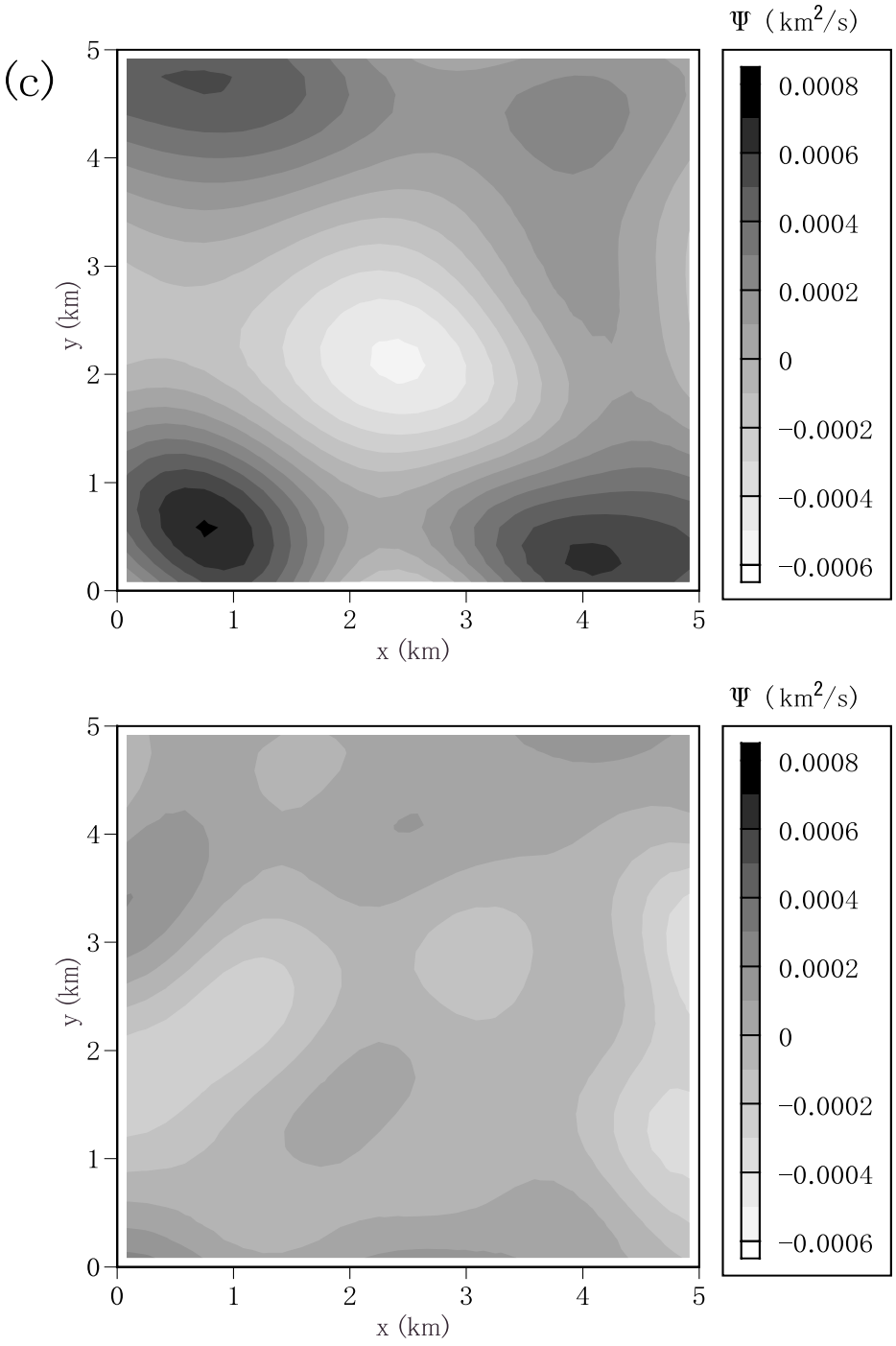

Figure 4.6: (Continued)

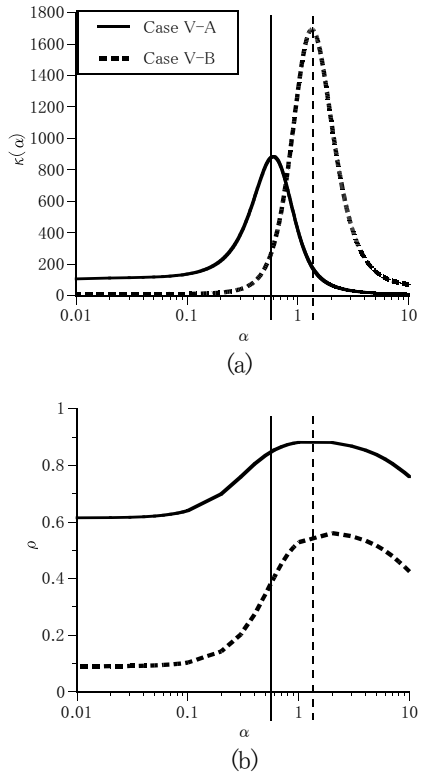

Figure 4.7: (a)κ curves and (b)ρ curves obtained for Cases V-A and -B. The vertical lines point the peaks on the κ curves.

fields corresponding to different tidal phases. Two kinds of vortex fields are here generated by putting $a = 1.0$, $b = 0$, $c = 0$ and $d = 0$ (Case V-A) and $a = 0$, $b = 0$, $c = 0$ and $d = 1.0$ (Case V-B). The computer simulation condition are taken the same as those for Case III-B, except for the prescribed vortex field. The vortex field for Case V-A has intensified energy in a wavenumber zone much lower than that for Case V-B; the size of the vortices distributed is much smaller for Case V-B than for Case V-A. The κ curve forms a steep peak at $\alpha = 0.59$ for Case V-A and $\alpha = 1.33$ for Case V-B (Figure 4.7a). The ρ curves are also characterized by broad peaks, distributed around the corresponding values of α (Figure 4.7b). The values of ρ are given as 0.854 and 0.534 for Cases V-A and -B, respectively. The small value of ρ for

Case V-B is due to the characteristic property of the model vortex field, i.e., there are some vortices with sizes smaller than the spatial resolution of tomography (ΔR). The unresolvable vortices may produce significant errors in the inverse analysis. This is also understood from the fact that optimum α is increased more for Case V-B than for Case V-A. It should also be noted that in the L-curve method the optimum values of α are changed flexibly, depending on the length scale of vortices.

4.5 Boundary correction of the inversion result

4.5.1 Basic idea and projection slice theorem

The idea of the algorithm presented in this section is to deal with velocity fields divided into two components: solenoidal and nonrotational components. The solenoidal component is determined from the acoustic tomography measurements. On the other hand, the nonrotational one is known that it cannot be measured by the acoustic tomography performed along the ray paths [38]. This idea has been proposed by Norton [40] and Sielschott [44] using some different algorithms.

The continuous vector field $\mathbf{u}$ can be decomposed into

$$\mathbf{u} = \mathbf{u}_\Psi + \mathbf{u}_\Phi \tag{4.23}$$

as shown in (4.4) and $\mathbf{u}_\Psi$ and $\mathbf{u}_\Phi$ is expressed by (4.5) and (4.6), respectively. The projection slice theorem provides the theoretical basis of inversion algorithms for the scalar-field tomography.The vector version of the projection slice theorem is here introduced to show the relationship between Ψ and Φ in sound transmission measurements. To state the theorem, let the i-th ray path connecting the point a and b parameterize in terms of the distance γ from the arbitrary selected origin and the unit vector $\mathbf{n}_\perp$ normal to the ray, as illustrated in Figure 4.8. As a result, equation

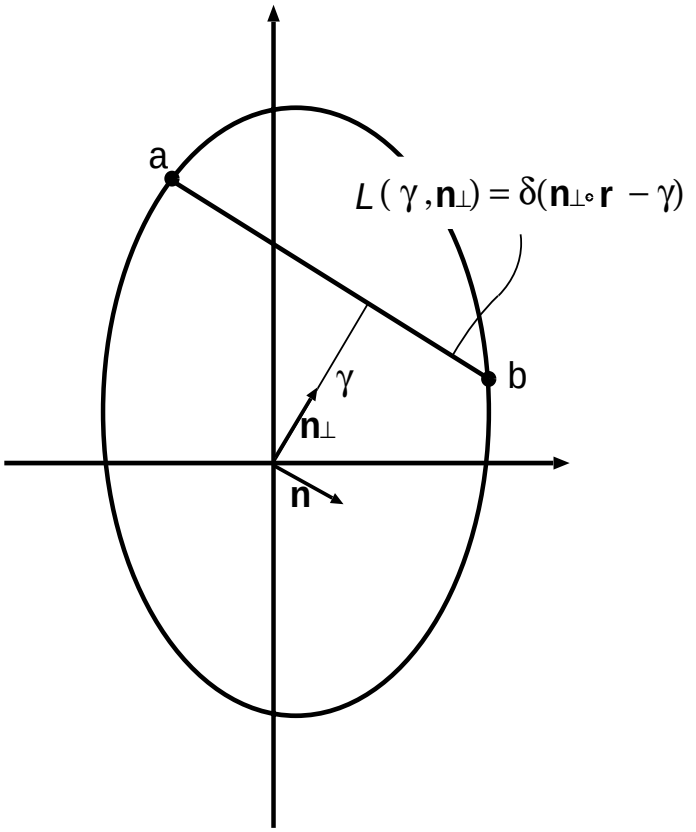

Figure 4.8: Schematic diagram showing the ray path L parameterized by its distance γ from the origin and by its direction represented by unit vector $\mathbf{n}$.

(4.3) reduces to

$$\triangle t_i(\gamma, \mathbf{n}_\perp) = -\oint_{L(\gamma,\mathbf{n}_\perp)} \frac{\mathbf{u}(\mathbf{r}) \cdot \mathbf{n}}{C_0^2} ds \tag{4.24}$$

Here, $\mathbf{r} = (x, y)$. This equation is rewritten

$$\triangle t_i(\gamma, \mathbf{n}_\perp) = -\frac{\mathbf{n}}{C_0^2} \cdot \oint \oint \mathbf{u}(\mathbf{r}) \delta(\mathbf{n}_\perp \cdot \mathbf{r} - \gamma) d^2\mathbf{r} \tag{4.25}$$

where δ is the Dirac delta function. Let us take two-dimensional Fourier transform of $\mathbf{u}(\mathbf{r})$

$$\hat{\mathbf{u}}(\mathbf{k}) = \int \int \mathbf{u}(\mathbf{r}) \exp(-i\mathbf{k} \cdot \mathbf{r}) d^2\mathbf{r} \tag{4.26}$$

where $\mathbf{k}$ is a wave number vector in the two-dimensional domain. The Fourier transform of $\triangle t_i(\gamma, \mathbf{n}_\perp)$ with respective to γ becomes

$$\hat{\triangle} t_i(k, \mathbf{n}_\perp) = \int \int \mathbf{u}(\mathbf{r}) \exp(-ik\mathbf{n}_\perp \cdot \mathbf{r}) d^2\mathbf{r} = \hat{\mathbf{u}}(k\mathbf{n}_\perp) \tag{4.27}$$

Therefore, equation (4.27) reduces to

$$\hat{\triangle} t_i(k, \mathbf{n}_\perp) = -\frac{\mathbf{n}}{C_0^2} \cdot \hat{\mathbf{u}}(k\mathbf{n}_\perp) \tag{4.28}$$

Now, the two-dimensional Fourier transform of equation (4.23) in use of equation (4.5) and (4.6) is

$$\hat{\mathbf{u}}(\mathbf{k}) = i(\mathbf{k} \times \hat{z})\hat{\Psi}(\mathbf{k}) + i\mathbf{k}\hat{\Phi}(\mathbf{k}) \tag{4.29}$$

where $\hat{\Psi}(\mathbf{k})$ and $\hat{\Phi}(\mathbf{k})$ are the two-dimensional Fourier transforms of $\Psi(\mathbf{r})$ and $\Phi(\mathbf{r})$, respectively. Substituting (4.29) into (4.28) yields

$$\hat{\triangle} t_i(k, \mathbf{n}_\perp) = -\frac{ik}{C_0^2} \hat{\Psi}(\mathbf{k}) \tag{4.30}$$

by $\mathbf{n}_\perp \times \hat{z} = \mathbf{n}$ and $\mathbf{n} \cdot \mathbf{n}_\perp = 0$. The important point of this result is that $\hat{\Phi}(\mathbf{k})$ is

removed and the stream function Ψ can be analyzed independently of the velocity potential Φ. This result also means that acoustic tomography measurements have no ability of measuring the velocity potential. Another explanation of this is that the increment of the velocity potential from station to station has no change for any ray paths connecting the stations.

4.5.2 Application algorithms

The remaining task is to determine Φ about which acoustic tomography measurements do not contain any information. It is straightforward that the constraint $\nabla \cdot \mathbf{u} = 0$ yields the Laplace's equation of Φ, which can be solved from the boundary values of $\mathbf{u}$. As the normal component of $\mathbf{u}$ vanishes on the closed boundary, we get

$$\frac{\partial \Phi}{\partial \tau} = -\tau \cdot \mathbf{u}_\Psi \tag{4.31}$$

and for the open boundary we get the boundary condition like

$$\nabla_\tau \Phi = 0 \tag{4.32}$$

By adding the solution of the Laplace's equation for Φ to the reconstructed stream function field, the correction to satisfy the boundary conditions can be done. However, the corrected field may not be the best solution which minimizes the residual based on equation (4.3)

$$\mathbf{e}^T\mathbf{e} = \sum_{i=1}^{N} \left(\Delta t_i + \oint_{\Gamma_0 i} \frac{\mathbf{u}(x,y) \cdot \mathbf{n}}{C_0^2} ds \right)^2 \tag{4.33}$$

Thus, the algorithm for the boundary correction is operated iteratively.

The algorithm is summarized as follows:

(i) Calculate the solution $\mathbf{u}_\Psi$ from the observation data Δt_i

(ii) Judge whether or not the iteration continues.

(iii) Calculate $\mathbf{u}_\Phi$ by solving the Laplace's equation of Φ which satisfies the boundary conditions (4.31) and (4.32) and determine $\mathbf{u} = \mathbf{u}_\Psi + \mathbf{u}_\Phi$.

(iv) Correct the observational data Δt_i

$$\Delta t_i' = \Delta t_i + \oint_{\Gamma_0 i} \frac{\mathbf{u}(x,y) \cdot \mathbf{n}}{C_0^2} ds$$

(V) Go back to (i) and calculate the corrected solution $\mathbf{u}_\Psi'$ from $\Delta t_i'$ to obtain the final current field $\mathbf{u} = \mathbf{u} + \mathbf{u}_\Psi'$.

The iteration is finished at a few times. Through the iteration, we have a solution $\mathbf{u}$ that fulfills the differential travel time data optimally, but even at this stage the boundary conditions may still be not satisfied perfectly by the final solution $\mathbf{u}$.

4.5.3 Computer simulation

To illustrate the significance of the boundary correction the model vortex field mentioned above (see Figure 4.4) is modified to impose a closed condition at both the boundaries $x = 0$ and $x = 5$km. The computer simulation is conducted for Case III-D, which is error-free and has seven acoustic stations. Differential travel times are calculated between the acoustic stations distributed in the vortex field model.

Figure 4.9a shows the model vortex field described with velocity vectors. The disappearance of u-component near the boundaries $x = 0$ and $x = 5$km is seen in this figure. The result of inversion analysis obtained without imposing the boundary condition is shown in Figure 4.9b. Current vectors near the closed boundaries are not in good agreement with the model vortex field. The estimated correlation coefficients ρ_u and ρ_v for the u- and v-components are 0.780 and 0.674, respectively. The current field corrected with the boundary condition and its deviation from the current field without the boundary condition are shown in Figure 4.9c and 4.9d, respectively. The velocity field is modified to satisfy the closed boundary conditions and the correlation

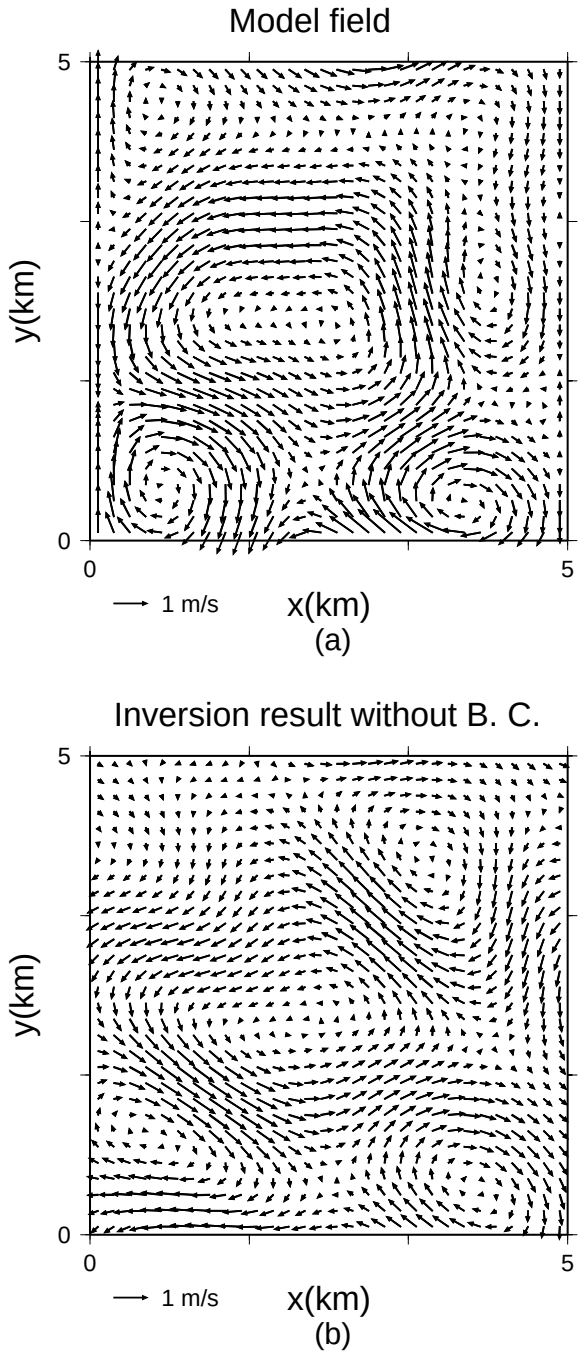

Figure 4.9: (a) The current field of ocean model and (b) the inversion result not corrected with the boundary conditions (c) the inversion result corrected with the boundary conditions (d) the deviation of (b) from (c)

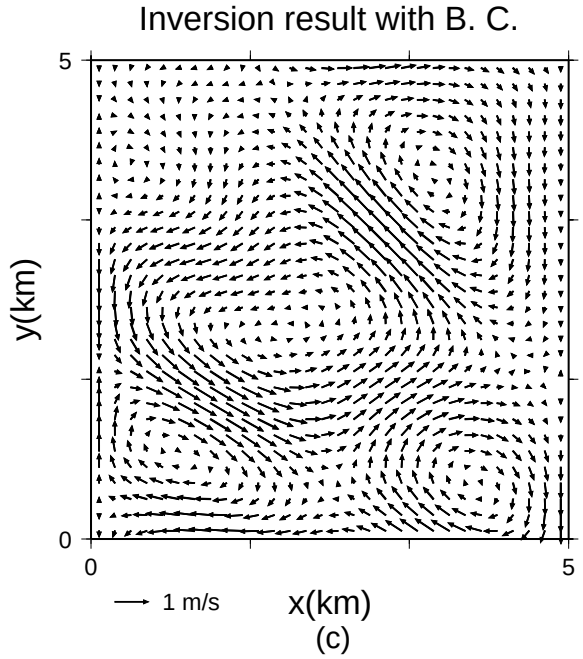

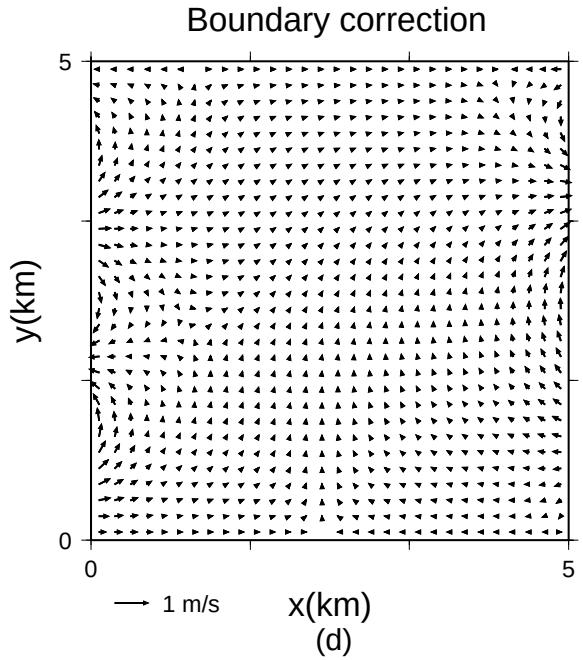

Figure 4.9: (Continued)

coefficients are increased up to 0.814 and 0.745 for ρ_u and ρ_v, respectively.

4.6 Inverse analysis including the boundary condition

4.6.1 Algorithms

If the stream function can be modified to satisfy the boundary condition, it is not necessary to correct the inversion result as discussed in the previous section. A spectral method including the coastal boundary condition was first used for the analysis of currents in Lake Ontario by Rao and Schwab [41]. They incorporated the principle of no flow perpendicular to a coastline into the eigenfunctions of current fields. This method has been applied to the mapping of current fields from the drifter data by Eremeev *et. al.* [12, 13]. Another method which used the boundary-fitted coordinate system to convert any coastal boundary into a rectangular boundary was applied to the analysis of the moored current meter data obtained on the Texas-Louisiana shelf [4]. Most recently, the nowcast of surface velocity fields in Monterey Bay were attempted by using the HF radar data on the basis of the normal mode analysis [27]. They used the eigenfunctions which satisfy no flow across the closed boundaries. Here, the method using the stream function put into zero at the coastlines is introduced.

Assuming that the coastline exists at both the eastern and western boundaries of the model domain as described in Figure 4.9a, we shall represent the stream function which satisfy no flow normal to the closed boundaries as follows:

$$\Psi(x,y) = \sum_{k=0}^{N}\sum_{l=0}^{N}\{A_{kl}\cos\gamma_0(kx+ly) + B_{kl}\sin\gamma_0(kx+ly)\}\cos\gamma_0 x \tag{4.34}$$

The algorithm of this method is very simple and the remaining work is to estimate A_{kl} and B_{kl} which satisfy no normal flow condition at the coastline.

4.6.2 Computer simulation

To illustrate the usefulness of this method the model vortex field of Figure 4.9a is also used here. The current vectors reconstructed are modified to satisfy the closed boundary conditions (Figure 4.10) and the correlation coefficients become 0.840 and 0.662 for ρ_u and ρ_v, respectively.

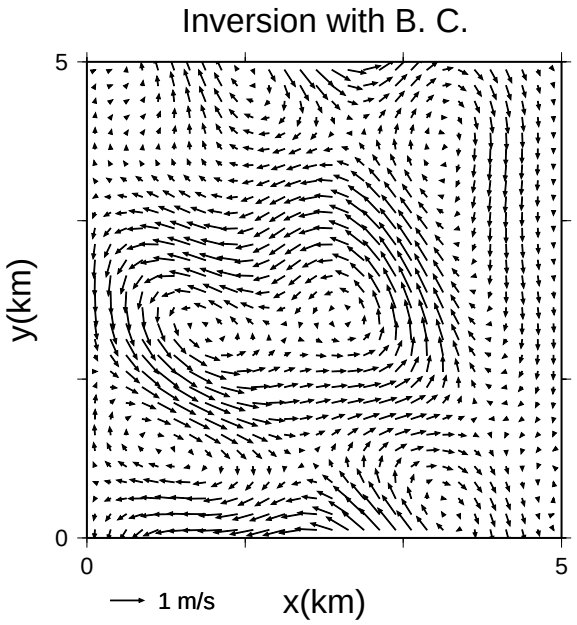

Figure 4.10: Inversion result reconstructed by including the boundary conditions

However, there is a serious shortcoming in this approach. This comes from that the coastline is generally not fitted to the inversion domain put to be rectangular. Thus, transforming the inversion domain to fit to the coastlines is needed for the practical application of this method.

4.7 Boundary-fitted coordinates and numerical grid generation

Coordinate transformation from the Cartesian coordinates system (x, y) to a new curvilinear coordinate system (ζ, η) is introduced to treat the arbitrary shaped coastlines in the inversion. The scheme of this transformation is shown briefly in Figure 4.11. The x and y on the physical domain (PD) represent the longitudinal and latitudinal coordinates. The counterparts ζ and η on the computational domain (CD) are the new curvilinear coordinates. This transformation method is called the boundary-fitted coordinate method.

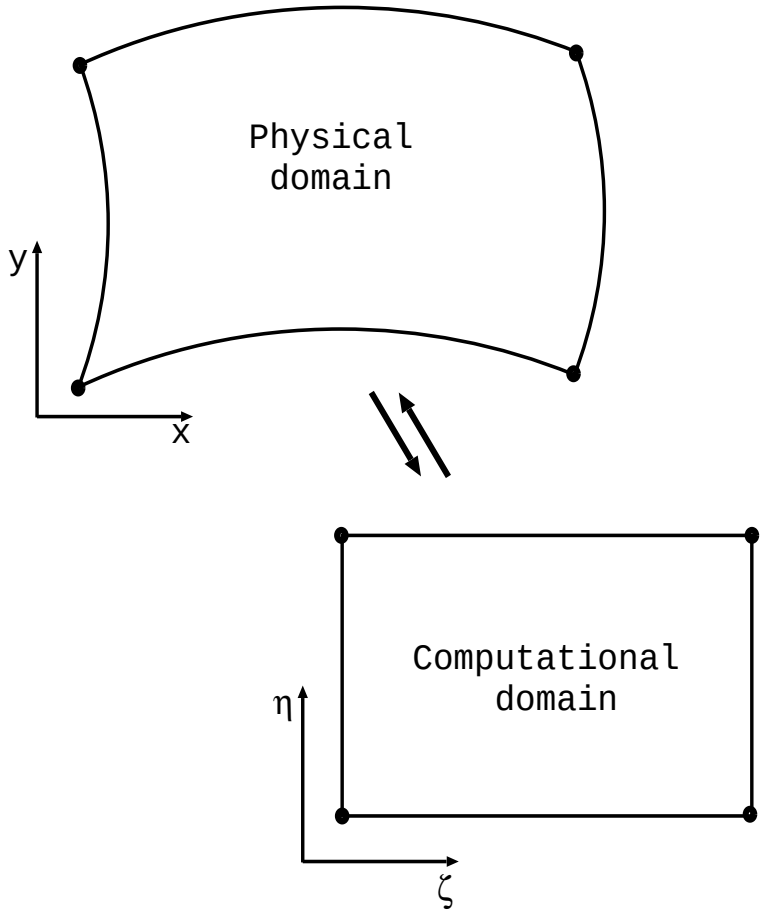

Figure 4.11: Schematic diagram for the transformation of coordinate system.

To make a boundary-fitted inverse domain, the numerical grid generation method with a lot of application to the coastal ocean modeling is used. An appropriate choice of the numerical grid has a key role in determining the quality of the solution of the coastal ocean model. The grid generation strategy is very important especially for the complicated physical domain accompanied by the complicated physical phenomena.

One can use a numerical grid generation technique to design the boundary-fitted curvilinear coordinate system for the coastal seas with complicated boundaries. There are a number of methods for the coordinate transformation. In this section, a brief discussion of the algorithm proposed by Thompson *et. al.* [46] is presented.

4.7.1 Transfinite interpolation

The coordinate transformation may be done directly by interpolation from the boundary location given by the latitude and longitude coordinate. Such coordinate generation procedures are referred to as the algebraic generation systems. Let the description start from an unidirectional interpolation before discussing two-directional one.

Unidirectional interpolation means that the interpolation is done for only one direction on the curvilinear coordinate. The simplest type of unidirectional interpolation for the linear case is expressed by

$$\mathbf{r}(\zeta) = (x(\zeta), y(\zeta)) = (1 - \frac{\zeta}{I_{max}})\mathbf{r}(\zeta_1) + \frac{\zeta}{I_{max}}\mathbf{r}(\zeta_2) \tag{4.35}$$

where $0 \leq \zeta \leq I_{max}$ and $\mathbf{r}$ is the Cartesian coordinate vector. The $\mathbf{r}(\zeta_1)$ and $\mathbf{r}(\zeta_2)$ are two boundary values for $\mathbf{r}$. Figure 4.12 shows this relations simply. Equation (4.35) can be written in another form

$$\mathbf{r}(\zeta) = \sum_{n=1}^{2} \phi_n(\frac{\zeta}{I_{max}})\mathbf{r}(\zeta_n) \tag{4.36}$$

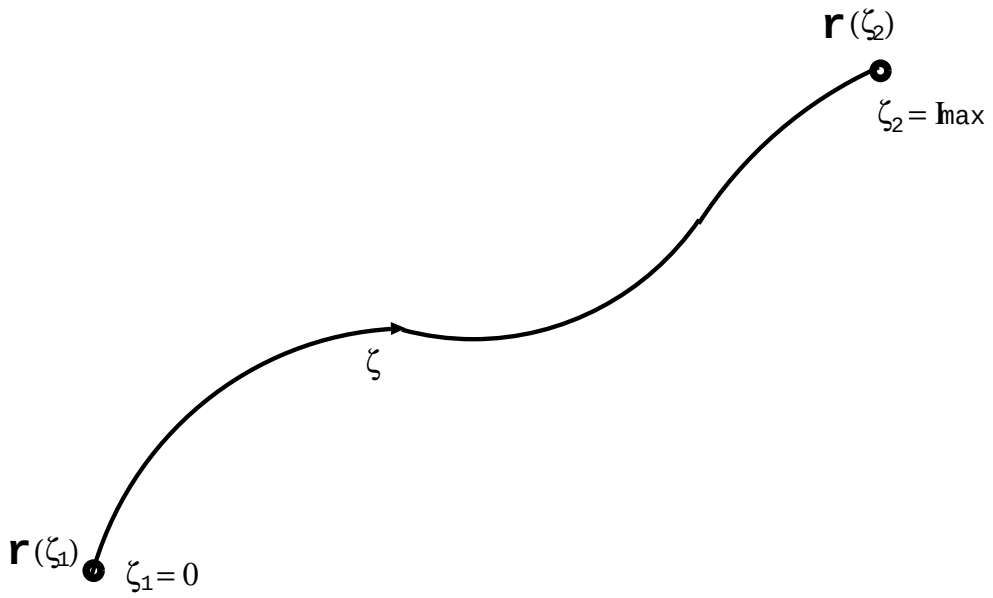

Figure 4.12: Schematic diagram of the unidirectional interpolation

where

$$\begin{aligned} \phi_1(\frac{\zeta}{I_{max}}) &= 1 - \frac{\zeta}{I_{max}} \\ \phi_2(\frac{\zeta}{I_{max}}) &= \frac{\zeta}{I_{max}} \end{aligned}$$

Of course, other interpolation methods are selectable for ϕ. Here, we select the linear interpolation for simplicity.

In two-direction method, a linear interpolation is done for two ways on the curvilinear coordinate by

$$\mathbf{r}(\zeta, \eta) = \sum_{n=1}^{2} \phi_n(\frac{\zeta}{I_{max}})\mathbf{r}(\zeta_n, \eta) \tag{4.37}$$

and

$$\mathbf{r}(\zeta, \eta) = \sum_{m=1}^{2} \psi_m(\frac{\zeta}{J_{max}})\mathbf{r}(\zeta, \eta_m) \tag{4.38}$$

where

$$\begin{aligned} \phi_1(\frac{\zeta}{I_{max}}) &= 1 - \frac{\zeta}{I_{max}}, \qquad \phi_2(\frac{\zeta}{I_{max}}) = \frac{\zeta}{I_{max}} \\ \psi_1(\frac{\eta}{J_{max}}) &= 1 - \frac{\eta}{J_{max}}, \qquad \psi_2(\frac{\eta}{J_{max}}) = \frac{\eta}{J_{max}} \end{aligned} \tag{4.39}$$

This interpolation is called the transfinite one since $\mathbf{r}(\zeta, \eta)$ is defined on the entire boundary between $\zeta = 0$ and $\zeta = I_{max}$ for equation (4.37) and between $\eta = 0$ and $\eta = J_{max}$ for equation (4.38).

The sum of equations (4.37) and (4.38) is

$$\mathbf{S}(\zeta, \eta) = \sum_{n=1}^{2} \phi_n(\frac{\zeta}{I_{max}})\mathbf{r}(\zeta_n, \eta) + \sum_{m=1}^{2} \psi_m(\frac{\zeta}{J_{max}})\mathbf{r}(\zeta, \eta_m) \tag{4.40}$$

where $\mathbf{S}(\zeta, \eta)$ on the boundary $\zeta = 0$ is given by

$$\mathbf{S}(0, \eta) = \mathbf{r}(0, \eta) + \sum_{m=1}^{2} \psi_m(\frac{\eta}{J_{max}})\mathbf{r}(0, \eta_m) \tag{4.41}$$

This means that $\mathbf{S}(\zeta, \eta)$ does not match with $\mathbf{r}(0, \eta)$ on the boundary $\zeta = 0$ because of the existence of the second term on the right hand side. The schematic diagram of this mismatch is shown in Figure 4.13. Similar mismatches which occur on all the boundaries are removed from $\mathbf{S}(\zeta, \eta)$ by subtracting a function formed by reducing the discrepancies between two boundaries by interpolation. Finally, the transfinite interpolation with the boundary correction results in

$$\begin{aligned} \mathbf{S}(\zeta, \eta) &= \sum_{n=1}^{2} \phi_n(\frac{\zeta}{I_{max}})\mathbf{r}(\zeta_n, \eta) + \sum_{m=1}^{2} \psi_m(\frac{\zeta}{J_{max}})\mathbf{r}(\zeta, \eta_m) \\ &\quad - \sum_{n=1}^{2}\sum_{m=1}^{2} \phi_n(\frac{\zeta}{I_{max}})\psi_m(\frac{\eta}{J_{max}})\mathbf{r}(\zeta_n, \eta_m) \end{aligned} \tag{4.42}$$

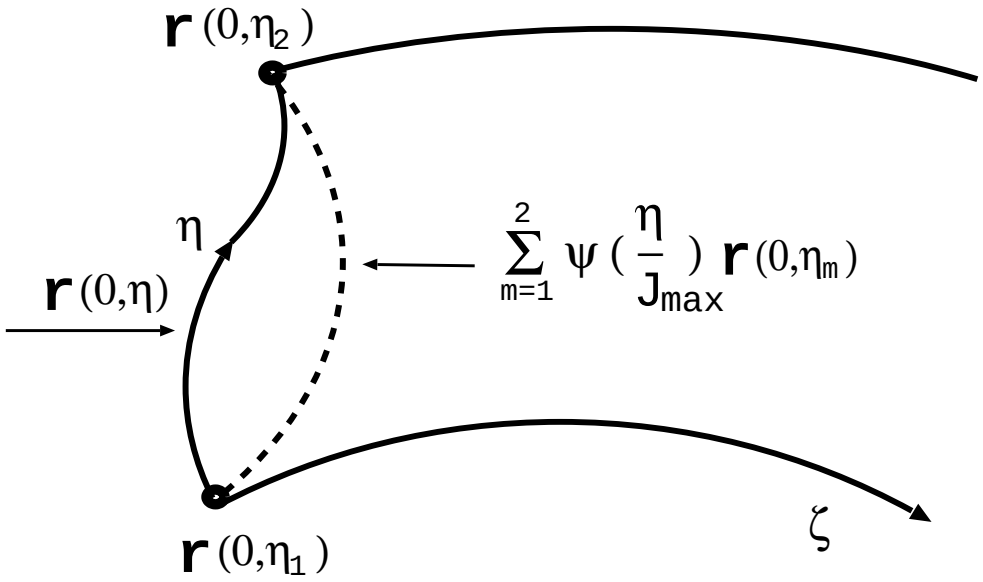

Figure 4.13: Schematic diagram of the boundary matching in the transfinite interpolation

4.7.2 Elliptic grid generation systems

A set of elliptic partial differential equations serves as a mean of coordinate transformation from PD to CD. Grids generated by the elliptic grid generation system generally have a tendency to be smoother than those by the algebraic grid generation system [46]. The Laplace or Poisson type systems are the most common form of the elliptic grid generation system. The basic coordinate transformation between (x, y) and (ζ, η) is described by the following system of the Poisson's equation:

$$\begin{aligned} \frac{\partial^2 x}{\partial \zeta^2} + \frac{\partial^2 x}{\partial \eta^2} &= P(x, y) \\ \frac{\partial^2 y}{\partial \zeta^2} + \frac{\partial^2 y}{\partial \eta^2} &= Q(x, y) \end{aligned} \tag{4.43}$$

where $P(x, y)$ and $Q(x, y)$ are the control functions which control the spacing and orientation of the coordinate lines. The system (4.42) reduces to the Laplace's system when $P(x, y) = Q(x, y) = 0$. Before generating a grid on the CD, the initial guesses

of x and y on the CD are done by the transfinite interpolation. The grid then can be generated by solving the Laplace or Poisson systems for both the x and y numerically. The boundary conditions for solving this system are the values of the (x, y) coordinates at the boundaries of the CD, which correspond to longitudes and latitudes along the coastlines on the PD. The elliptic grid generation systems of Laplace or Poisson type have better quality of smoothness, orthogonality, and well distributed interior.

4.7.3 Application to the tomography field

When the boundary-fitted coordinate transformation is applied to the CAT inversion domain, we shall introduce the new stream function on the CD (see equation (4.7))

$$\Psi(\zeta, \eta) = \sum_{k=0}^{N} \sum_{l=0}^{N} \Big(A_{kl} \cos(\alpha k \zeta + \beta l \eta) + B_{kl} \sin(\alpha k \zeta + \beta l \eta) \Big) \tag{4.44}$$

where

$$\alpha = \frac{2\pi}{L_\zeta}, \qquad \beta = \frac{2\pi}{L_\eta}$$

Here, L_ζ and L_η are the side lengths of the square in the ζ and η direction, respectively. From the above equation, $u(\zeta, \eta)$ and $v(\zeta, \eta)$ are also obtained as

$$u(\zeta, \eta) = -\frac{\partial \Psi}{\partial \eta}, \qquad v(\zeta, \eta) = \frac{\partial \Psi}{\partial \zeta} \tag{4.45}$$

For including boundary condition, equation (4.34) may be redefined on the CD by multiplying $\cos \alpha\zeta$ in equation (4.44).

The remaining task is to make a coordinate transformation for the integral equation (4.3). Here, note that the ray paths are not straight lines on the CD. Thus, the integration on the CD is approximated by the sum of the segmented integral sections

as follows:

$$\Delta t_i = -\Bigg(r_1 \cdot \oint_{\Gamma_{0i_1}} \frac{\mathbf{u}(\zeta,\eta)\cdot\mathbf{n}_1}{C_0^2} ds \quad + \quad r_2 \cdot \oint_{\Gamma_{0i_2}} \frac{\mathbf{u}(\zeta,\eta)\cdot\mathbf{n}_2}{C_0^2} ds + \cdots + r_n \cdot \oint_{\Gamma_{0i_n}} \frac{\mathbf{u}(\zeta,\eta)\cdot\mathbf{n}_n}{C_0^2} ds \Bigg) \tag{4.46}$$

where

$$\Gamma_{0i_1} + \Gamma_{0i_2} + \cdots + \Gamma_{0i_n} = \Gamma_{0i}$$

and $\mathbf{n}_1$, $\mathbf{n}_2$,$\cdots$, $\mathbf{n}_n$ are the unit vectors tangent to the i_1-, i_2-,$\cdots$, i_n-th ray segments, respectively. Here, Γ and s are the lengths on the CD. The r_1, r_2,$\cdots$, r_n are the ratios of the unit arc lengths on the PD to those on the CD. By this approach, equation (4.9) is transformed to

$$\begin{aligned} \Delta t_i \quad = \quad & \Bigg(\sum_{j=1}^{(N+1)^2} r_1 \cdot P_j \int_0^{R_{i1}} \frac{\frac{\partial}{\partial\eta}Q_j(\zeta,\eta) - \frac{\partial}{\partial\zeta}Q_j(\zeta,\eta)\tan\phi_{i1}}{C_0^2} d\zeta \\ & + \sum_{j=1}^{(N+1)^2} r_2 \cdot P_j \int_{R_{i1}}^{R_{i2}} \frac{\frac{\partial}{\partial\eta}Q_j(\zeta,\eta) - \frac{\partial}{\partial\zeta}Q_j(\zeta,\eta)\tan\phi_{i2}}{C_0^2} d\zeta \\ & + \cdots + \sum_{j=1}^{(N+1)^2} r_n \cdot P_j \int_{R_{in-1}}^{R_{in}} \frac{\frac{\partial}{\partial\eta}Q_j(\zeta,\eta) - \frac{\partial}{\partial\zeta}Q_j(\zeta,\eta)\tan\phi_{in}}{C_0^2} d\zeta \Bigg) \end{aligned} \tag{4.47}$$

where

$$\mathbf{P} = [A_{00}, B_{00}, A_{01}, B_{01}, \ldots, A_{NN}, B_{NN}]$$

and

$$\mathbf{Q}(\zeta,\eta) = [1, 0, \cos\beta\eta, \sin\beta\eta, \ldots, \cos(\alpha N\zeta + \beta N\eta), \sin\gamma_0(\alpha N\zeta + \beta N\eta)]$$

Here, ϕ_{i1}, ϕ_{i1},$\cdots$, ϕ_{in} are the angles between the ζ-axis and the i_1-, i_2-,$\cdots$, i_n-th ray segments. R_{i1}, R_{i2},$\cdots$, R_{in} are the start or end points of each ray segment along the ζ-axis.

Note that the current field reconstructed by the inversion which uses equation (4.46) is represented by the function of ζ and η. This means that when u and v on the CD are transformed to those on the PD, the directions of u and v are also changed. Figure 4.14 shows the schematic diagram for the transformation of u and v from the CD to PD. When putting the angle between $u(\zeta,\eta)$ and $u_o(x,y)$ into θ_x and that between $v(\zeta,\eta)$ and $v_o(x,y)$ into θ_y (θ_x and θ_y are measured counterclockwise), the $u(x,y)$ and $v(x,y)$ transformed on the PD is expressed by follows:

$$\begin{aligned} u(x,y) &= \frac{u(\zeta,\eta)(\sin\theta_x + \cot\theta_y \cos\theta_x) - v(\zeta,\eta)(\cos\theta_x + \tan\theta_x \sin\theta_y)}{\tan\theta_x + \cot\theta_y} \\ v(x,y) &= \tan\theta_x \cdot u(x,y) + v(\zeta,\eta)(\cos\theta_y + \tan\theta_x \sin\theta_y) \end{aligned} \tag{4.48}$$

for $\theta_y \neq 0$ and,

$$\begin{aligned} u(x,y) &= \frac{u(\zeta,\eta)\cos\theta_x - v(\zeta,\eta)(\cos\theta_y + \tan\theta_x \sin\theta_y)}{\tan\theta_x} \\ v(x,y) &= u(\zeta,\eta)\cos\theta_x \end{aligned} \tag{4.49}$$

for $\theta_y = 0$.

4.8 Summary and discussion

A computer simulation of the CAT has been carried out to find out the inversion scheme suitable for the two-dimensional tidal vortex fields with a horizontal scale of 5km×5km, and to determine the optimum number of stations for the model vortex field. The simulation was conducted with four kinds of configurations constructed with four, five, seven and nine acoustic stations. In most cases, the random errors of the Gaussian distribution were added to the travel time difference data to evaluate the effect of errors on the inversion. The model vortex fields with different length scale have been examined to test the performance of the inversion.

The conventional stochastic inverse method is reduced to the damped least square

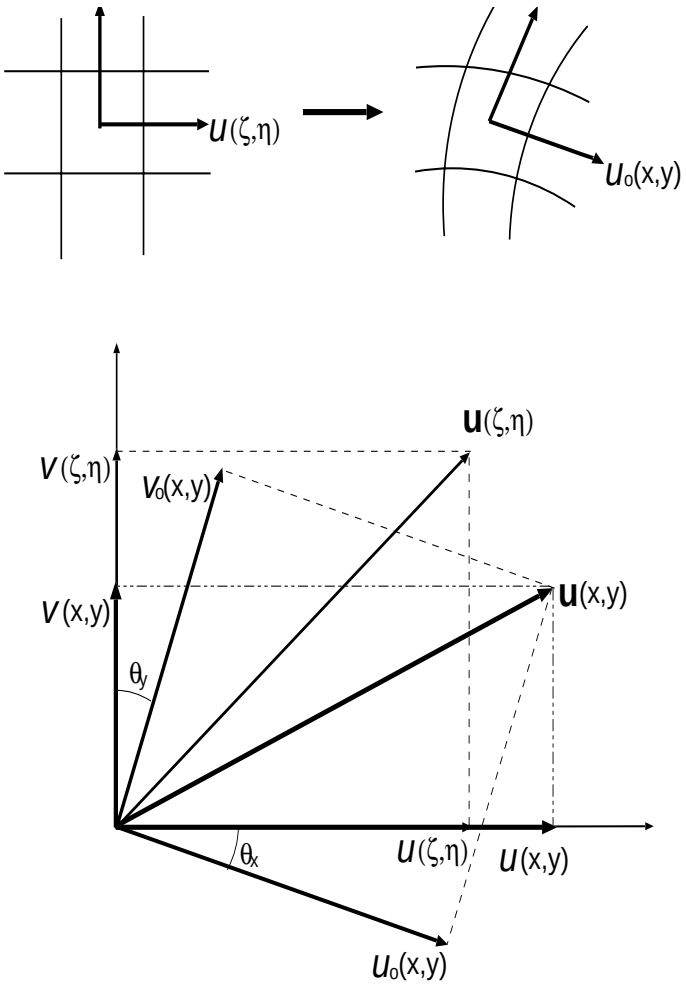

Figure 4.14: Schematic diagram for the coordinate transformation of u and v. The u_o and v_o represent the velocity components in the orthogonal curvilinear grid system

method because variable tidal vortex fields in the coastal seas make it difficult to obtain sufficient *a priori* statistical information on the solution field. The appropriate selection of the weighting factor α^2 was found to be the most important point in obtaining an optimum inversion inversion. The L-curve method—searching for a point where the curvature κ of the L curve becomes maximum—is applied to determine the optimum α. The results of the computer simulation show the usefulness of the L-curve method in which the optimum α can be determined flexibly, depending on variable vortex fields and the data errors. When tidal vortices with various length scales

coexist, vortices smaller than ΔR are difficult to reconstruct, serving to increase α. Even in such complicated conditions, vortices larger than ΔR can still be well reconstructed by use of the optimum α. The L-curve method is proposed as a simple method for reconstructing two-dimensional tidal vortex fields in the coastal seas. Given the sufficient *a priori* statistical information, the full form of the covariance matrix of the solution may be determined *a priori*, serving to improve the performance of the inversion.

New methods for the CAT inversion including coastal boundaries are also proposed. One method is to correct the inversion result to satisfy the boundary condition. The other is to include the boundary condition into the stream function field which satisfy the closed boundary condition.

The role of the new methods in the inversion are investigated by performing the computer simulation. It is shown that application of boundary conditions improved the inversion results to be consistent with the model field.

In addition the boundary-fitted curvilinear coordinates are introduced to include the arbitrary shaped coastal boundaries into the inversion. The boundary-fitted curvilinear coordinates may broaden the application of the CAT to the coastal seas with complex coastlines.

CHAPTER 5

ANALYSES OF THE REAL OCEAN DATA

5.1 Introduction

In this chapter the inversion and data assimilation methods proposed in the previous chapters are applied to two cases of field experiments. In one experiment, the tomography domain is reserved at the central part of the coastal sea distant from the shoreline. In another one, the acoustic stations are taken near the shoreline which surrounds the tomography domain.

5.2 Bungo Channel experiment

5.2.1 Site and Method

A CAT experiment was carried out at the central part of the Bungo Channel of the Seto Inland Sea during June 28 - 30, 1999 (Figure 5.1). In this experiment four acoustic stations (T1 $\sim$ T4) were placed at the corners of the square region with side length 5km and one (T5) at the center of the square. An upward looking ADCP was moored 10m above the bottom at station A near T5 to obtain comparison data with the CAT. The experiment was carried out during 18:00 June 28 to 12:00 June 30. Sound signals were transmitted every 6 minutes in this experiment.

The configuration of the CAT mooring system is shown in Figure 5.2. Each station are composed of a 5.5kHz transmitter and hydrophone, mounted on the mooring line

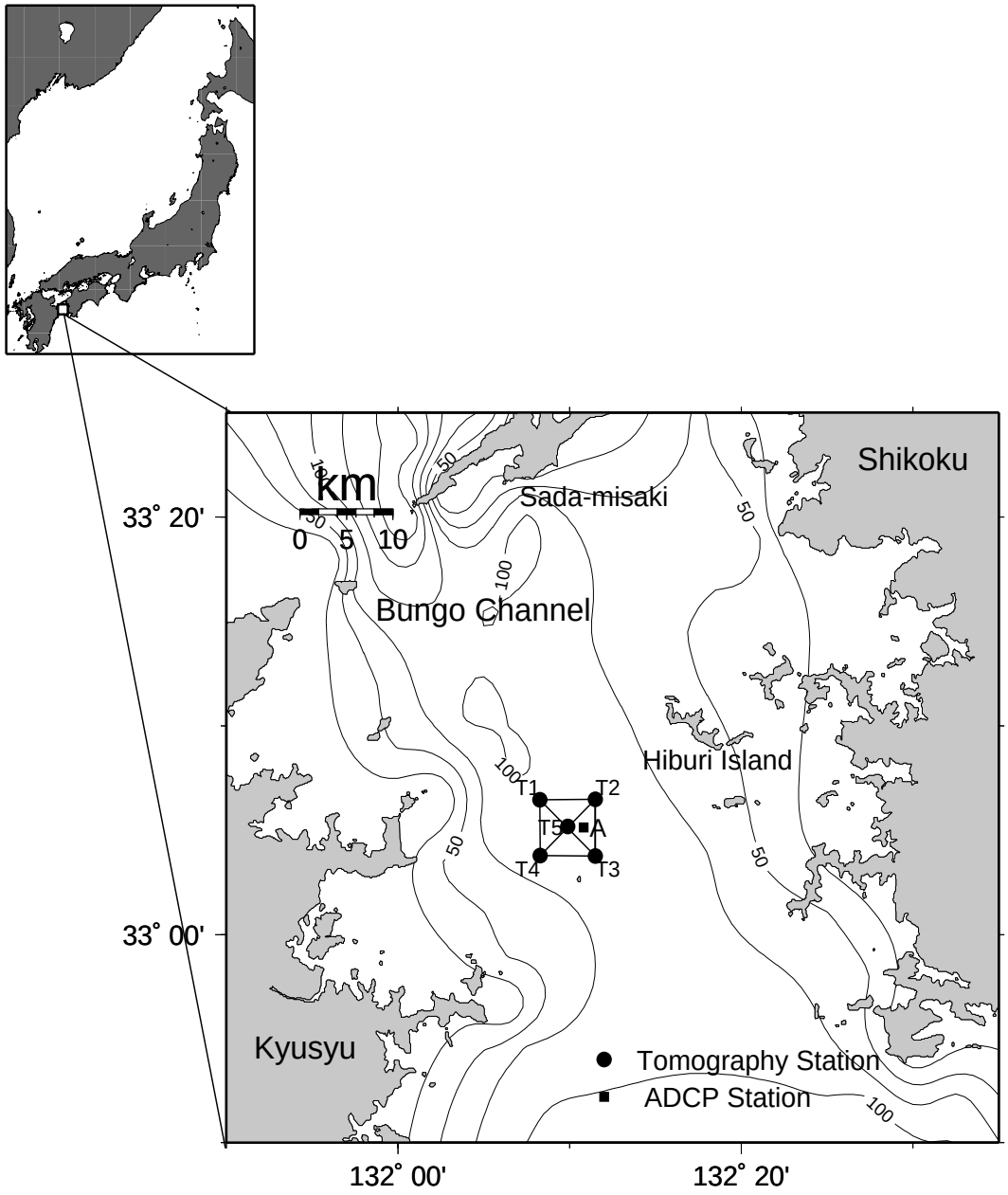

Figure 5.1: Location map of the Bungo Channel experiment. The position of the acoustic stations (T1 $\sim$ T5) is marked by the dots and that of the ADCP mooring station (A) by the square.

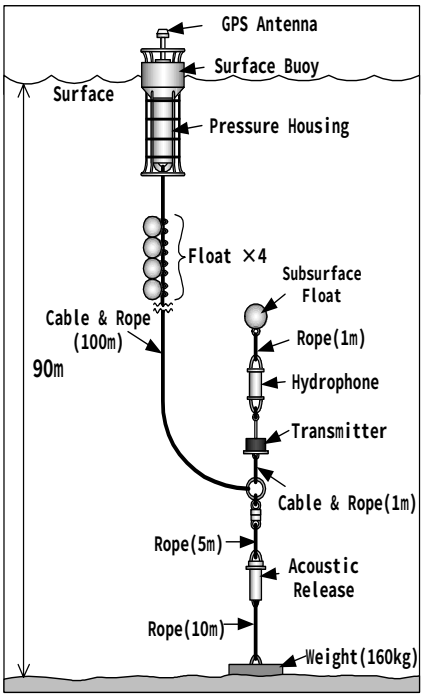

Figure 5.2: Mooring design for the Bungo Channel experiment

at 17m and 18m above the bottom, respectively. The transmitter and hydrophone are designed to stand up vertically by a subsurface float. Each mooring system is also equipped with the Global Positioning System (GPS) to synchronize the timing of sound transmission and receiving with precise accuracy. The travel time data acquired at each station are saved in the memory inside the pressure housing supported by a surface buoy. As the bottom topography is relatively flat with a floor depth of about 90m around the observation region, all the mooring stations have the same design.

5.2.2 Inversion

Figure 5.3 shows the time series of differential travel times obtained for all the station pairs in the Bungo Channel experiment. These time series were smoothed through 30 minutes running mean. Because of the weak signals obtained between T1 and T3,

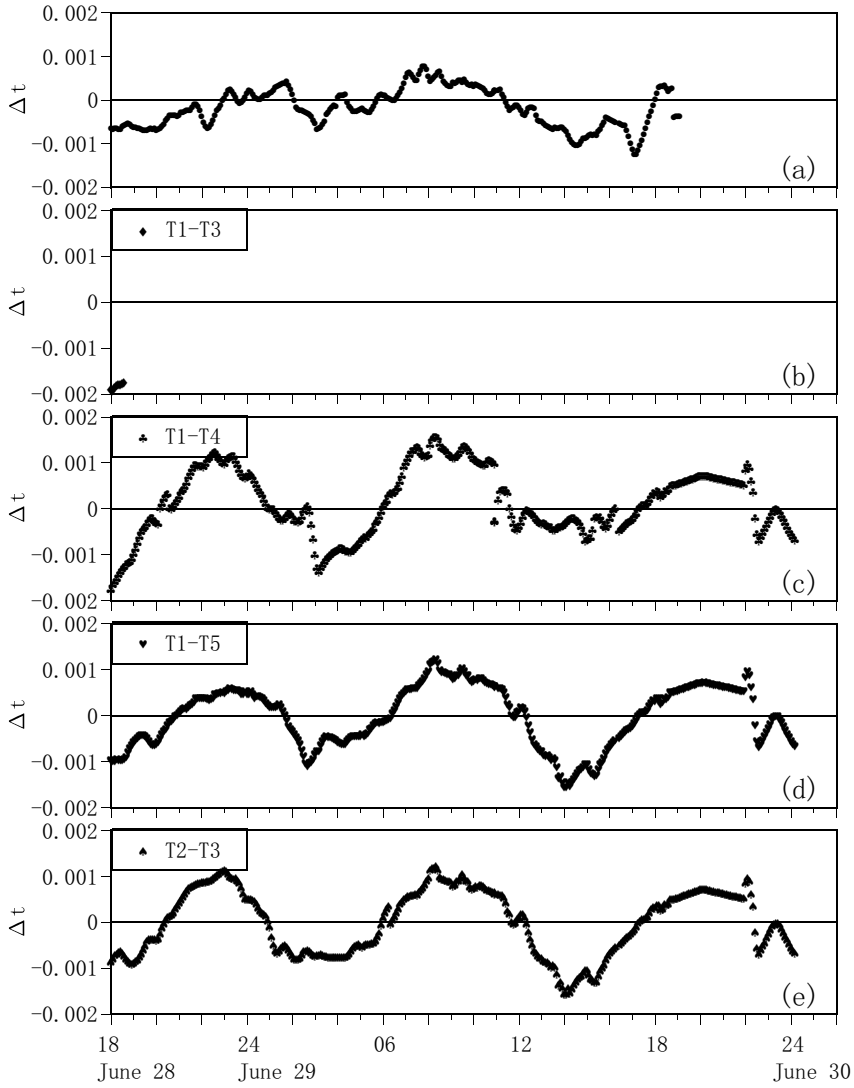

Figure 5.3: Time series of differential travel times obtained for all the station pairs in the Bungo Channel experiment.

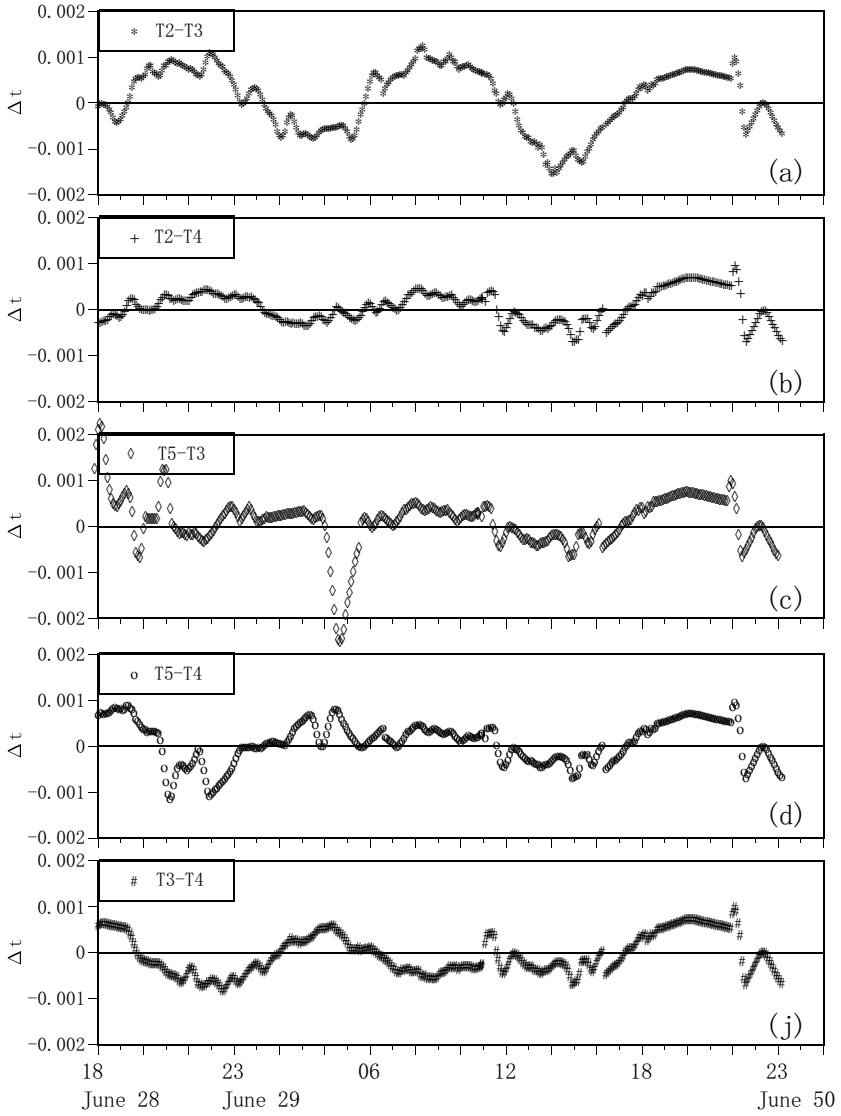

Figure 5.3: (Continued)

the differential travel time data between T1 and T3 were not included in the inverse analysis.

In the Bungo Channel experiment the ray paths T1-T4 and T2-T3 were directed to the north-to-south and T1-T2 and T4-T3 to the east-to-west, respectively. Thus, in the inversion the (x, y) coordinate is rotated counterclockwise by 10° as shown in Figure 5.4 to reduce the nullspace in the matrix $\mathbf{E}$. If the (x, y) coordinate is used

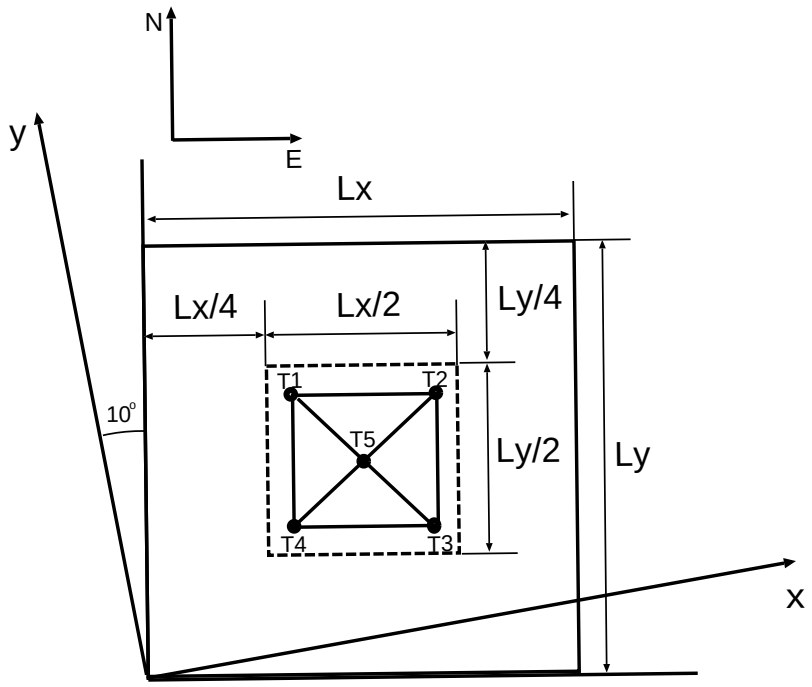

Figure 5.4: Sketch of the tomography and inversion domains for the Bungo Channel experiment. L_x and L_y are the east-west and north-south lengths of the inversion domain, respectively.

in the inversion without rotation, no information is obtained on the u-components of current near the ray paths T1-T4 and T2-T3 and the v-component near the ray paths T1-T2 and T4-T3. The lack of information results in the increasing nullspace in the matrix $\mathbf{E}$.

Figure 5.5 shows the reconstructed stream function fields obtained at the phase when the tidal current changes its direction from north to south. Semi-closed stream-

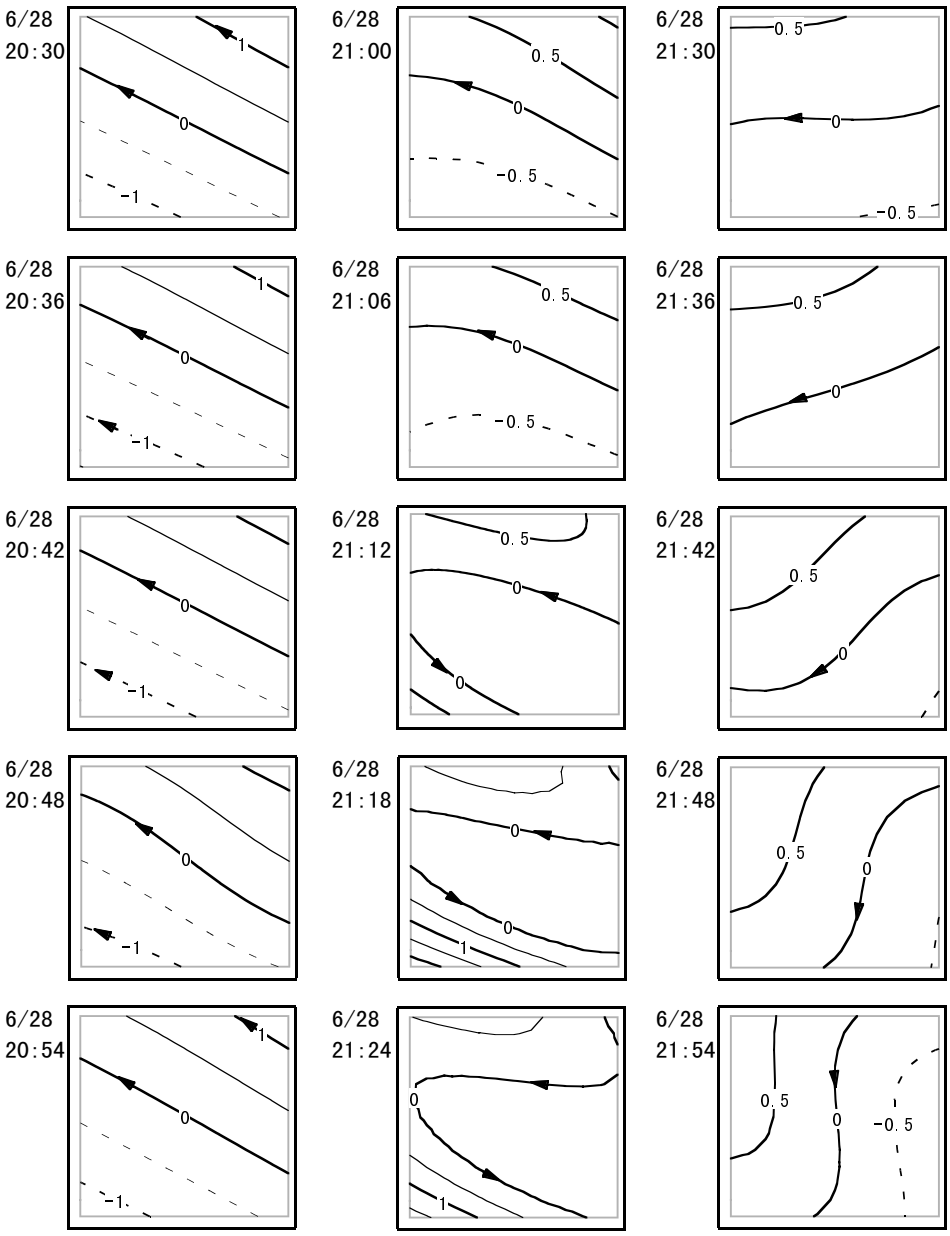

Figure 5.5: Reconstructed stream function fields obtained during 20:30 to 21:54, June 28.

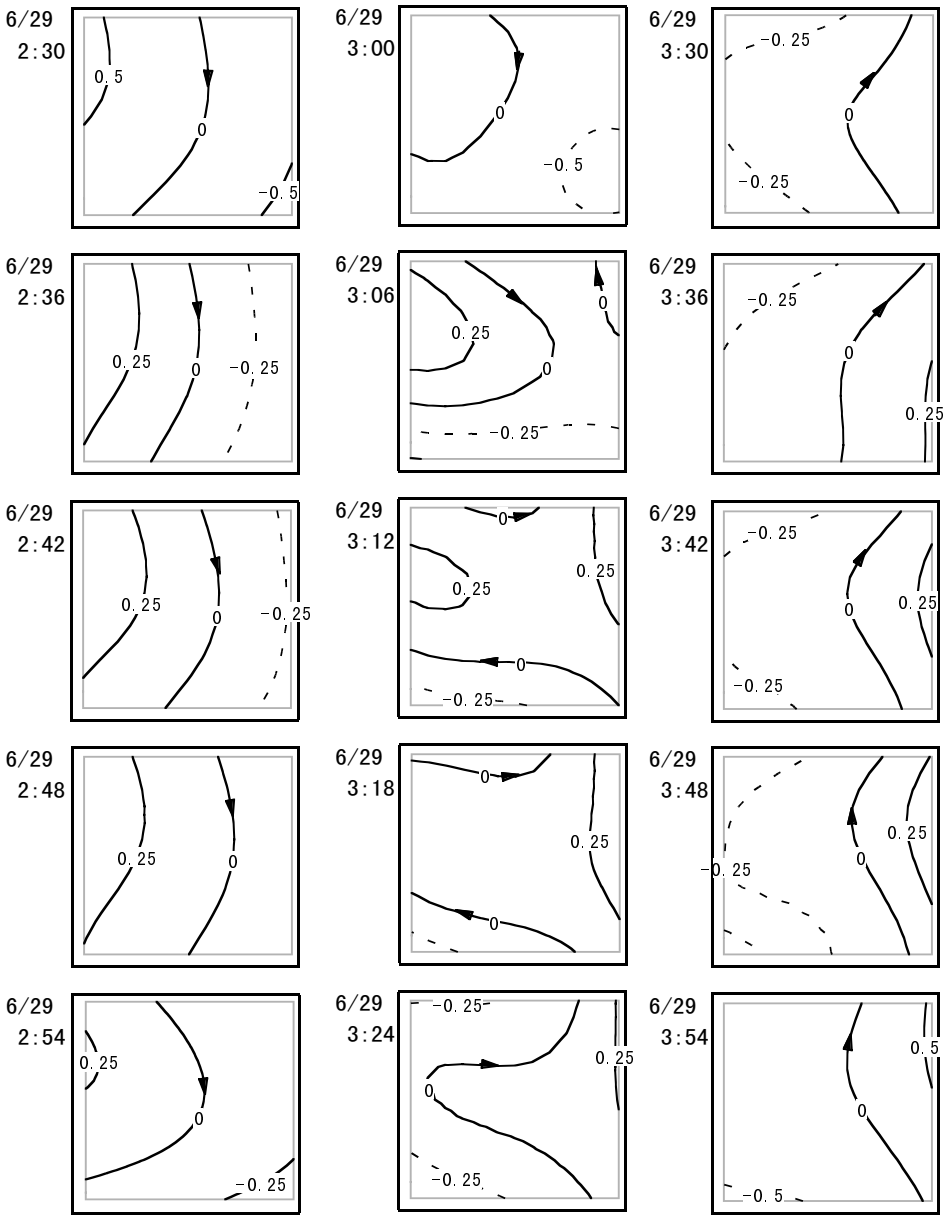

Figure 5.6: Reconstructed stream function fields obtained during 2:30 to 3:54, June 29.

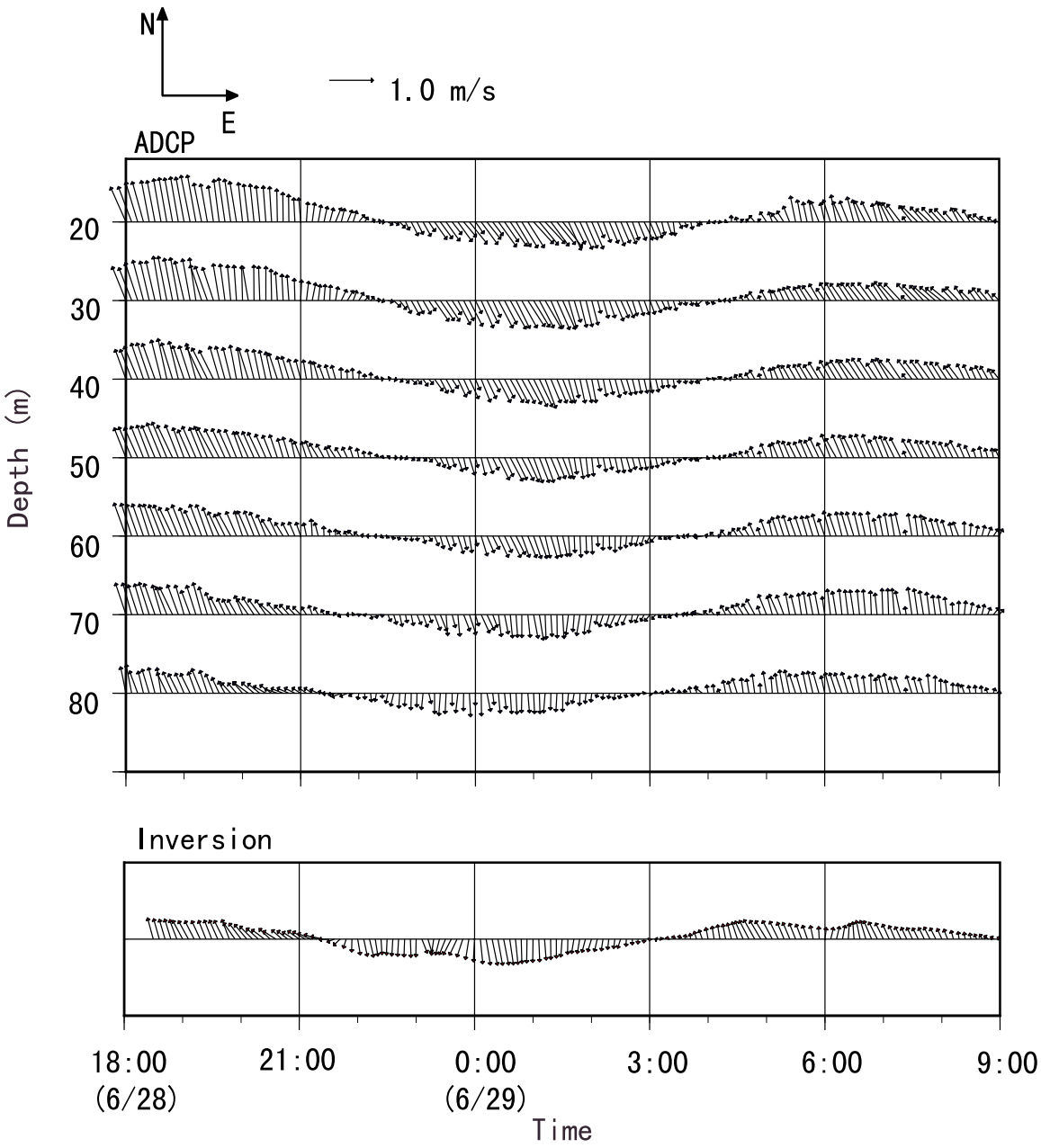

Figure 5.7: Comparison of the ADCP and inversion results at the ADCP station A. The upper and lower panels are for the ADCP and inversion, respectively. A scale of velocity is drawn at uppermost part of the figure.

lines with a counterclockwise rotation are visible during 21:12 to 21:24 of June 28. More detailed maps show that an elliptical vortex is generated inside the semi-closed streamlines. Except this period, the streamline patterns are fairly monotone. The current fields obtained 6 hours later are shown in Figure 5.6. At this time, the current direction change from south to north, inducing a clockwise elliptical vortex during 3:06 to 3:24 of June 29 (Figure 5.6). The inversion results obtained at station A are compared with the ADCP data in Figure 5.7. The inversion results have the best fit with the deepest ADCP data obtained at the 80m depth. The mean and standard deviation of the velocity difference between both the data at this depth are $8.4 \pm 6.6 \mathrm{cms}^{-1}$ for the magnitude and $8.0 \pm 7.1^{\circ}$ for the direction. It should be remarked that the velocity is underestimated by the CAT. The major source of this underestimation may come from that CAT produces path-integrated data along the ray while ADCP makes point measurements in the horizontal space.

5.3 Neko-Seto Channel experiment

5.3.1 Site and Method

A CAT experiment was carried out in the Neko-Seto Channel of the Seto Inland Sea, Japan during March 2 - 3, 1999 (Figure 5.8). Five acoustic stations (S1 $\sim$ S5) were used in this experiment. The same CAT systems as those used in the Bungo Channel experiment were deployed at the nearshore stations of about 10m depth not to disturb ship traffic. All the acoustic stations transmitted sound signals every 5 minutes at a synchronized timing. The distances between a pair of acoustic stations ranged from 2km to 5km. A transmitter and hydrophone were mounted on the mooring line at 5m and 4m above the bottom, respectively. Figure 5.9 shows the sketch of the mooring system.

Because of the complicated shoals near station S4, any travel time data between S1-S4 and S2-S4 were not acquired. The sound transmission between S2 and S3 was

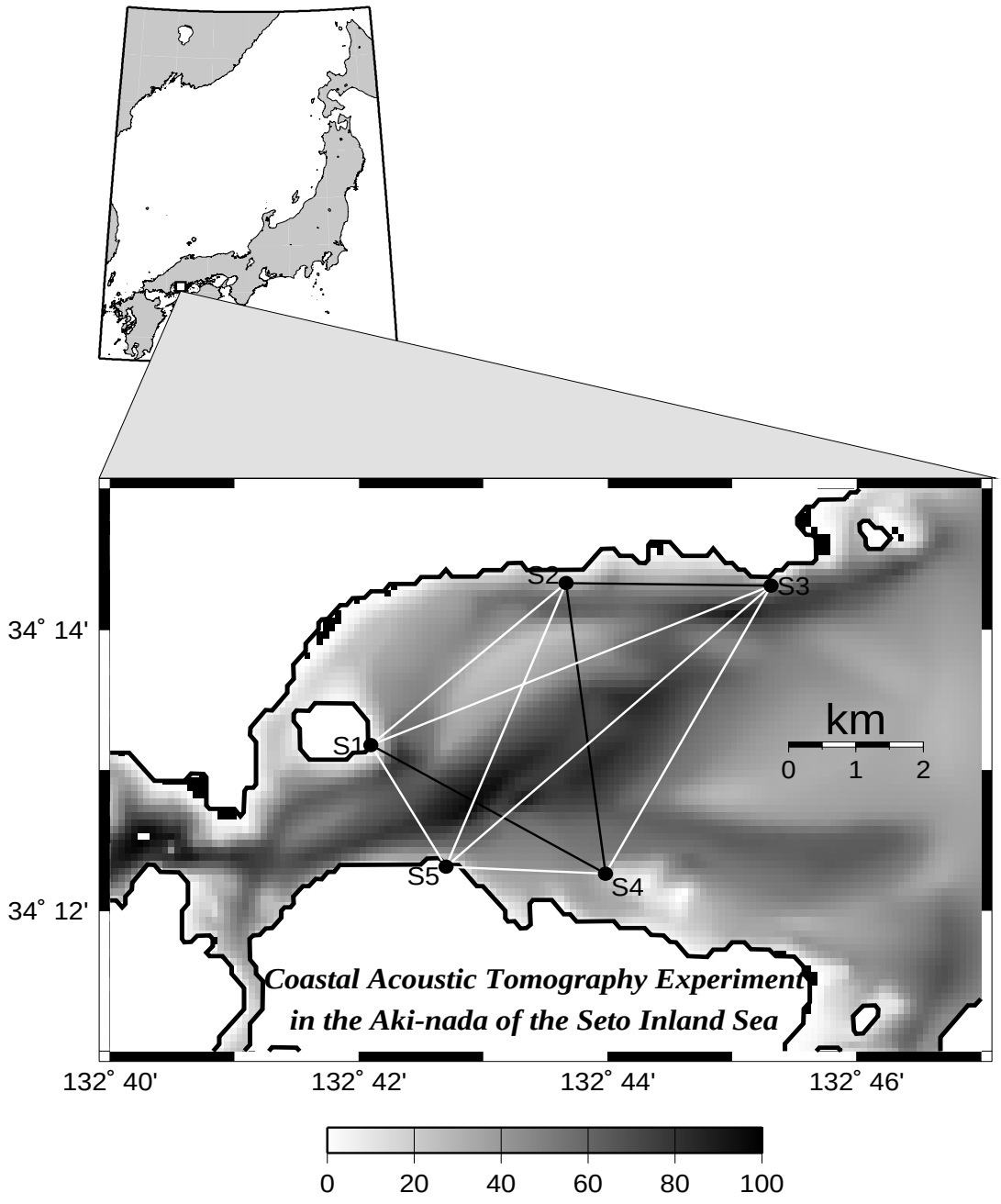

Figure 5.8: Coastline and bathymetry of the Neko-Seto Channel CAT experiment. The location of the CAT stations (S1 $\sim$ S5) are shown by the dots. The white and black lines indicate the ray paths of successful and failed transmissions, respectively.

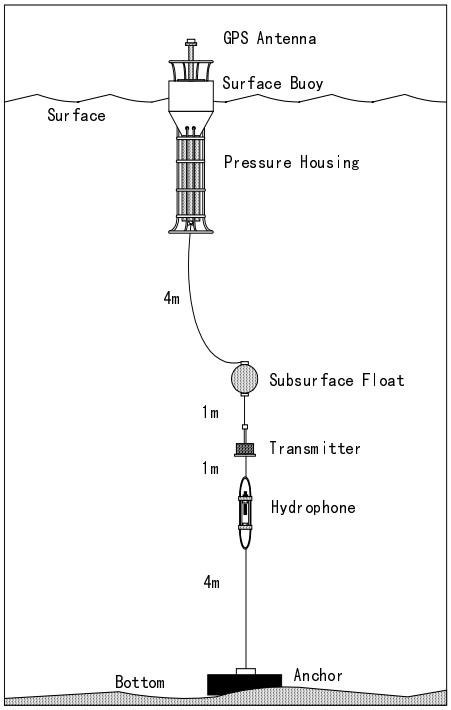

Figure 5.9: Sketch of th mooring system for the Neko-Seto Channel experiment.

prohibited by a cape protruded into the offshore.

Overall current features in the Neko-Seto Channel are characterized by a eastward tidal jet which flushes out from a narrow inlet located at the western part of the region. At the flood tide, the strengthened tidal jet induces a pair of tidal vortices [45]. The location of the vortex pair can also be seen through the bottom topography in Figure 5.8. Better reconstruction of the tidal vortex generation by the optimal analytical method for CAT proposed in the previous chapters is the main target of this section. The validity of the inversion results is confirmed in comparison with the results of the shipboard ADCP surveys, which were done inside of the observation region in parallel to the tomography experiment.

5.3.2 Inversion

The time series of the differential travel times obtained for all the station pairs are shown in Figure 5.10. During two and half hours after 8:00 March 3, the station S5 did not work well because of the drifting of the mooring system, so the inversion were not performed during this period. The time series data were smoothed through 30 minutes running mean. Major variability of the time series was a semi-diurnal tide. However, the time series for S2-S5 were out of phase to those for S1-S3 though the ray path S1-S3 was close to the ray path S3-S5. This means that currents along these two ray paths have an reverse direction.

In order to introduce the shape of the coastlines in the inversion, we shall use the boundary-fitted curvilinear coordinates. As shown in Figure 5.11, the physical domain (PD), which covers the acoustic tomography region bounded by northern and southern coastlines, is transformed into a rectangular computational domain (CD). The eastern and western boundaries of the CD are determined to cover all the acoustic rays. The rectangle represented with dashed lines in the upper panel of Figure 5.11 is the inversion domain that may be utilized in the conventional inversion.

Figure 5.12 shows the reconstructed current fields obtained every hour by the inversion including the coastal boundary correction. The initiation, growth, translation and decay of the tidal vortices are well visible in the reconstructed current fields. At the start of the CAT experiment a clockwise vortex is developed in the region surrounded by S1, S2, S4 and S5, and its shape and location is well compared to the ADCP data, represented by the red velocity vectors (Figures 5.12(b) and (c)). This vortex diminishes rapidly in the slack water (Figure 5.12(d)). A vortex pair with a east-to-west arrangement is developed with increasing eastward current (Figures 5.12(g) and (h)). This vortex pair exists for the next two hours (Figures 5.12(i) and (j)) and diminishes in the slack water (Figure 5.12(l)). A vortex pair with the reverse rotation appears at the phase of maximum westward current (Figure 5.12(m)). The western, clockwise vortex is absorbed into the narrow outlet (Figure

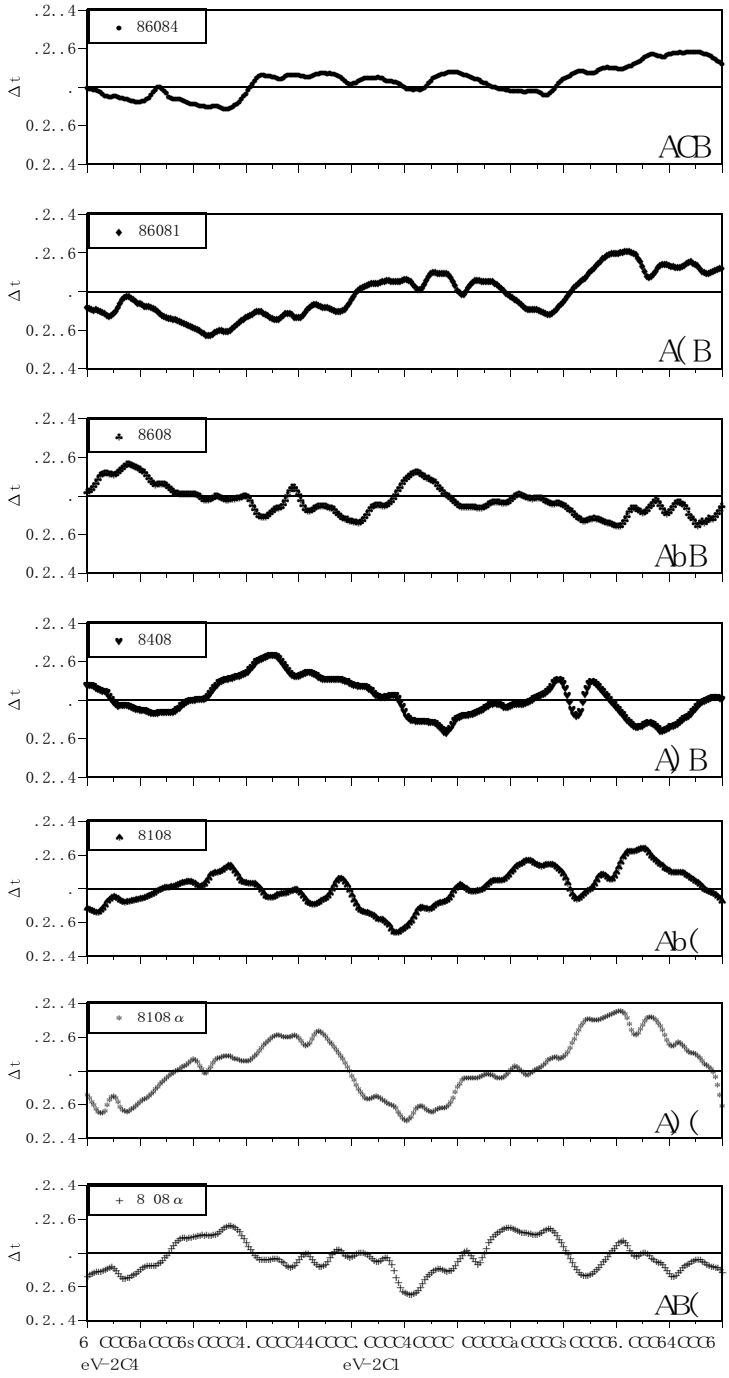

Figure 5.10: The time series of the differential travel times obtained for all the station pairs in the Neko-Seto Channel experiment.

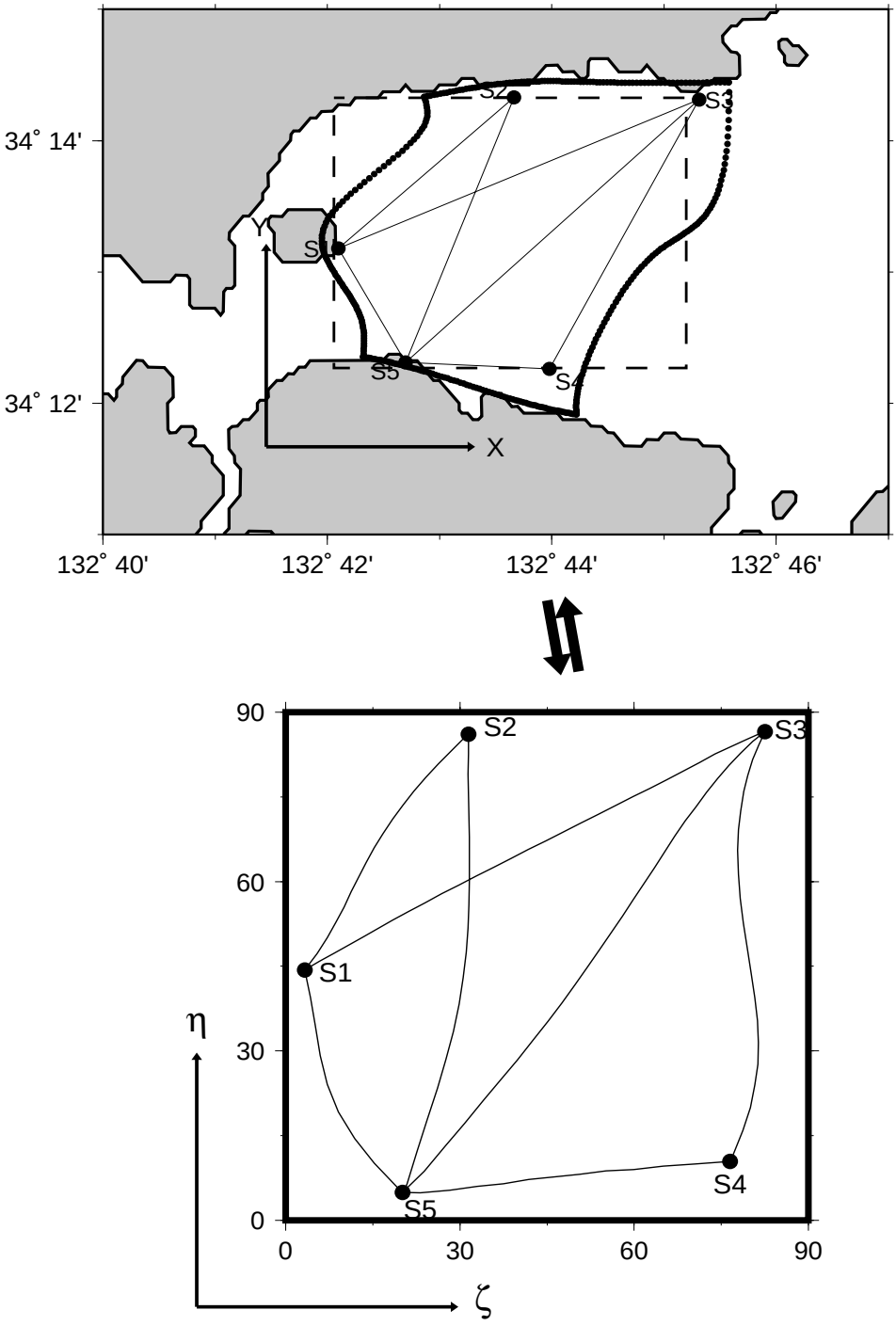

Figure 5.11: Curvilinear coordinate transformation applied to the Neko-Seto Channel experiment. The upper panel shows the PD surrounded by the thick solid line. This PD is transformed into the rectangular CD in the lower panel.

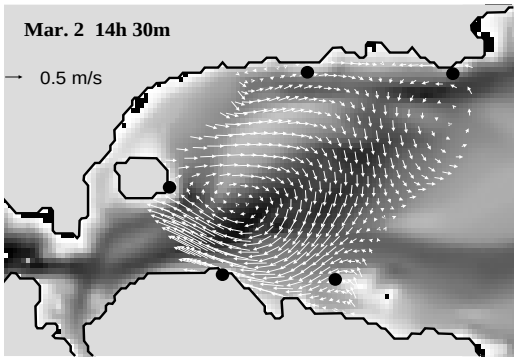

(a) 14h 30m (March 2)

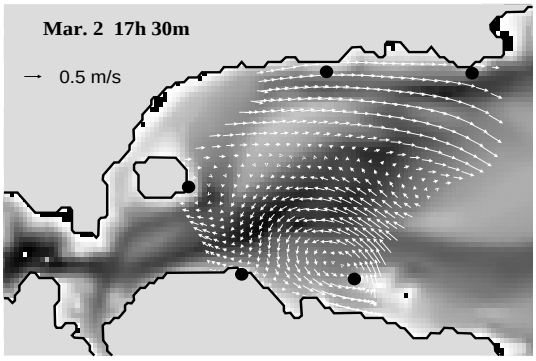

(d) 17h 30m

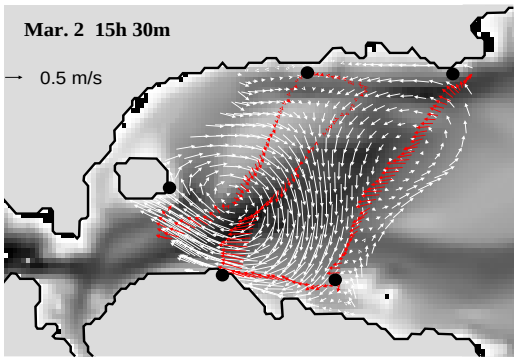

(b) 15h 30m

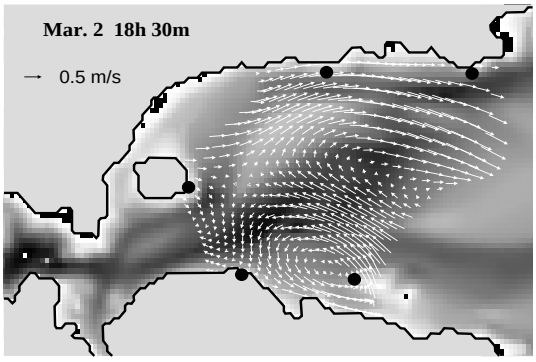

(e) 18h 30m

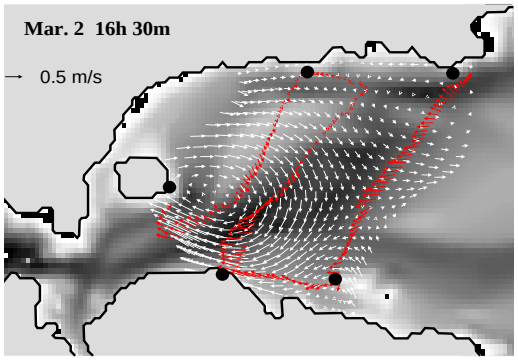

(c) 16h 30m

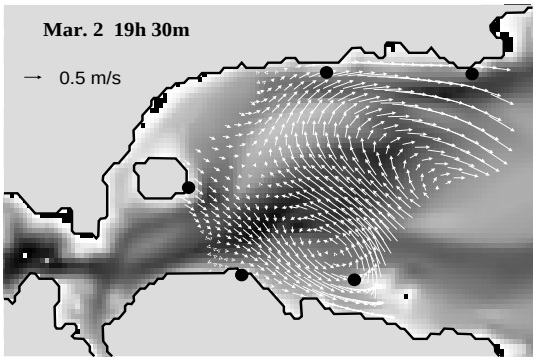

(f) 19h 30m

Figure 5.12: Inversion results obtained at various tidal phases. The red vectors in (b)-(c) and (t)-(u) represent the shipboard ADCP data obtained during 14:45 to 16:45 March 2 and during 10:40 to 12:40 March 3, respectively.

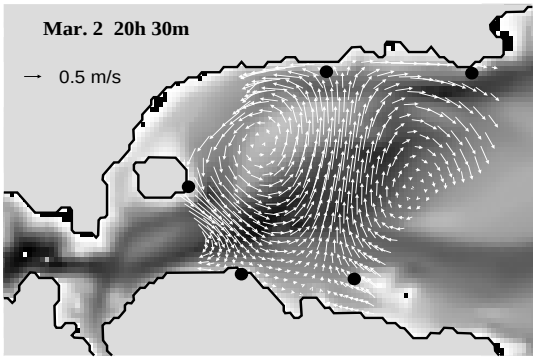

(g) 20h 30m

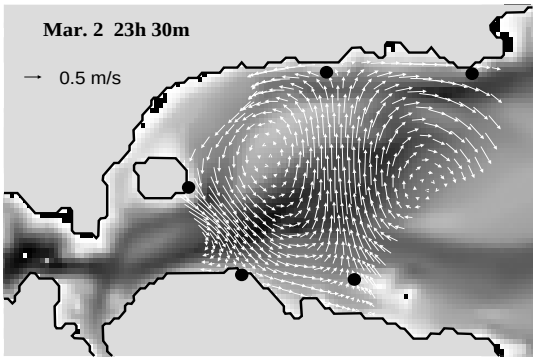

(j) 23h 30m

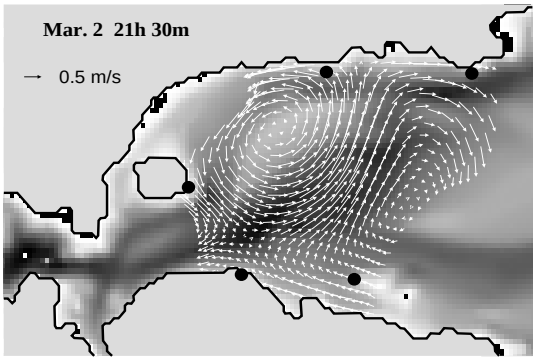

(h) 21h 30m

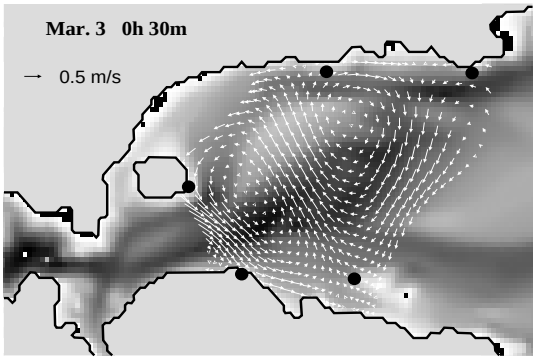

(k) 0h 30m (March 3)

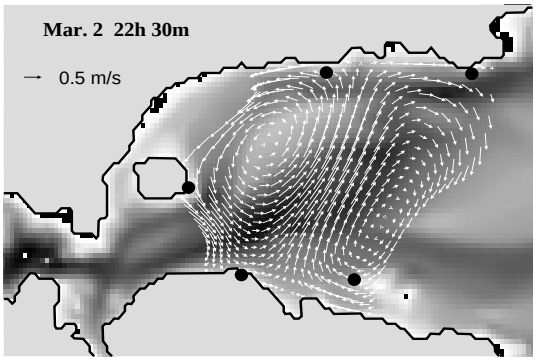

(i) 22h 30m

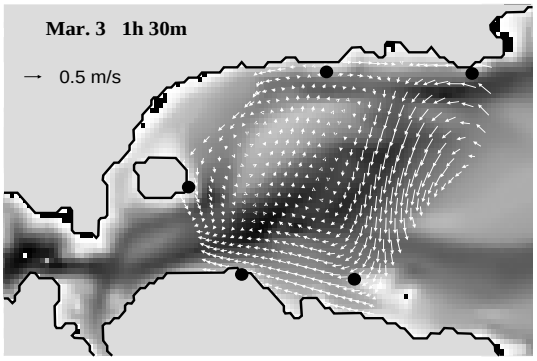

(l) 1h 30m

Figure 5.12: (Continued)

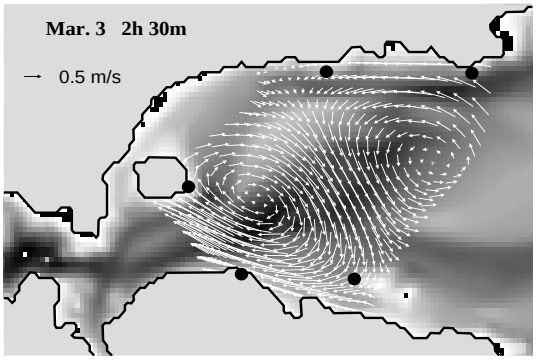

(m) 2h 30m

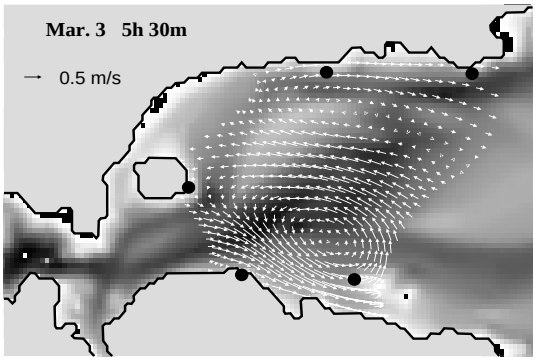

(p) 5h 30m

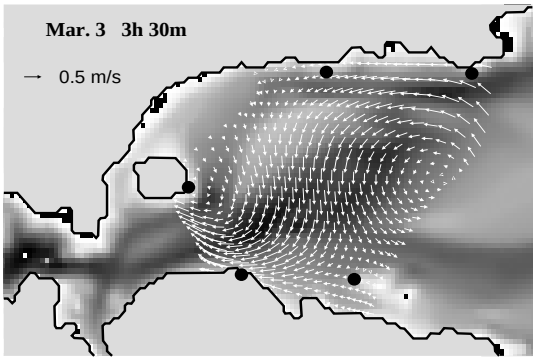

(n) 3h 30m

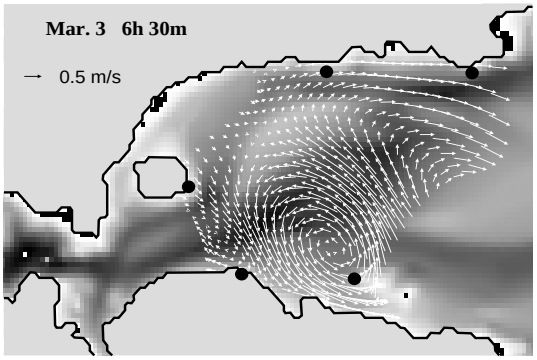

(q) 6h 30m

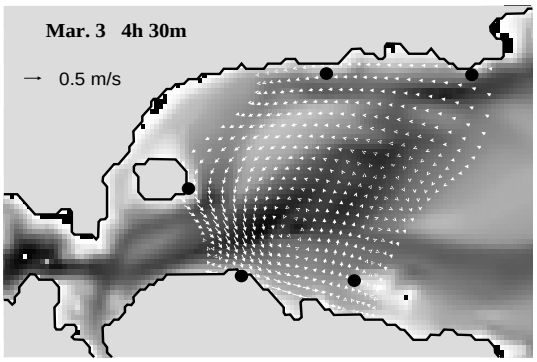

(o) 4h 30m

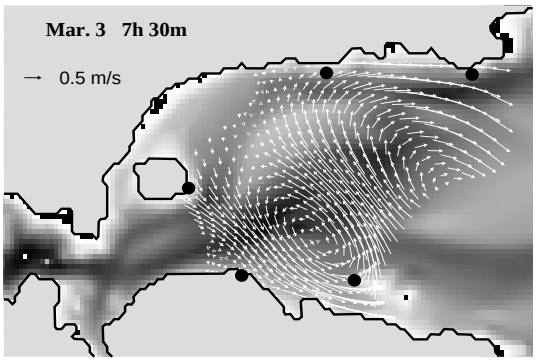

(r) 7h 30m

Figure 5.12: (Continued)

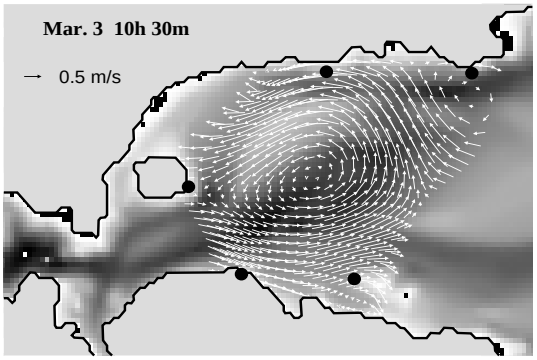

(s) 10h 30m

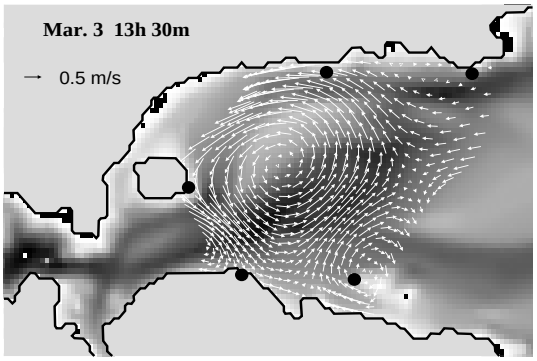

(v) 13h 30m

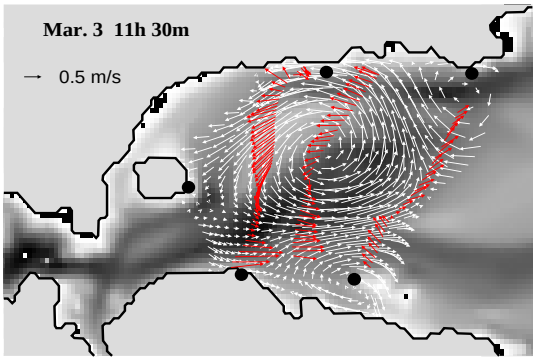

(t) 11h 30m

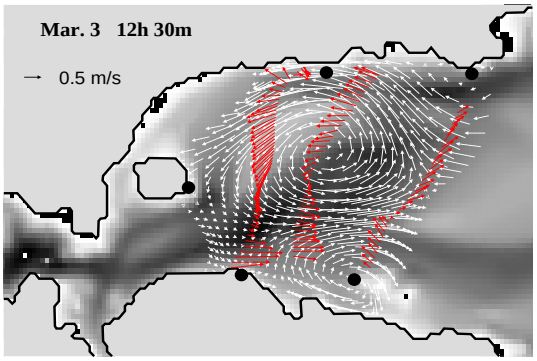

(u) 12h 30m

Figure 5.12: (Continued)

5.12(n)) and the both vortices diminish in the slack water (Figure 5.12(o)). The next flood tide is stronger than the previous one which occurred 12 hours ago. At this time, the vortex pair is arranged in the north-to-south direction (Figures 5.12(t) and (u)). Such difference of the vortex pair at the time lag of 12 hours is caused by the diurnal component of tide. The ADCP data obtained during 10:40 to 12:40 March 3 are in good agreement with the inversion results in the western half of the tomography domain while the current directions are opposite at the eastern edge of the domain (Figure 5.12(t) and (u)). The reason for this disagreement is that the number of ray paths is smaller in the eastern half of the tomography domain than in its western half.

5.4 Application of the data assimilation to the Neko-Seto Channel data

5.4.1 Numerical ocean model

In order to obtain the inversion estimates which are consistent with the dynamical laws such as mass and momentum conservation, the Kalman filter technique is needed to be combined with a deterministic ocean model where these physical laws are reflected. For the assimilation of CAT data the Princeton Ocean Model (POM) developed by Blumberg and Mellor [1] is used. This model is a three-dimensional primitive equation model with a free surface and formulated in a sigma coordinate vertically and a Cartesian coordinate horizontally. This model uses a mode splitting technique to calculate separately an external, barotropic and internal, baroclinic modes. In this study, the data assimilation is performed only for the barotropic mode because the vortex field which is dominant in the Neko-Seto Channel is quite barotropic. Thus, the state vector $\mathbf{x}$ in (3.1) is composed of two-dimensional velocity components (u, v) and surface elevation η, which results in 2193 state vector length.

The external mode equations are obtained by integrating the internal mode equations over the depth, thereby eliminating all vertical structures. The conservation of mass and momentum for the external mode are expressed by

$$\frac{\partial \eta}{\partial t} + \frac{\partial \overline{U} D}{\partial x} + \frac{\partial \overline{V} D}{\partial y} = 0 \tag{5.1}$$

$$\begin{aligned} \frac{\partial \overline{U} D}{\partial t} + \frac{\partial \overline{U}^2 D}{\partial x} + \frac{\partial \overline{UV} D}{\partial y} \quad - \quad & \tilde{F}_x - f\overline{V}D + gD\frac{\partial \eta}{\partial x} = - < wu(0) > + < wu(-1) > \\ & -\frac{gD}{\rho_0}\int_{-1}^{0}\int_{\sigma}^{0}\Big[D\frac{\partial \rho^{'}}{\partial x} - \frac{\partial D}{\partial x}\sigma^{'}\frac{\partial \rho^{'}}{\partial \sigma}\Big]d\sigma^{'}d\sigma \end{aligned} \tag{5.2}$$

$$\begin{aligned} \frac{\partial \overline{V} D}{\partial t} + \frac{\partial \overline{UV} D}{\partial x} + \frac{\partial \overline{V}^2 D}{\partial y} \quad - \quad & \tilde{F}_y + f\overline{U}D + gD\frac{\partial \eta}{\partial y} = - < wv(0) > + < wv(-1) > \\ & -\frac{gD}{\rho_0}\int_{-1}^{0}\int_{\sigma}^{0}\Big[D\frac{\partial \rho^{'}}{\partial y} - \frac{\partial D}{\partial y}\sigma^{'}\frac{\partial \rho^{'}}{\partial \sigma}\Big]d\sigma^{'}d\sigma \end{aligned} \tag{5.3}$$

Here, the overbars denote vertically integrated velocities and $< wu(0) >$ and $< wv(0) >$ are the wind stress components and $< wu(-1) >$ and $< wv(-1) >$ are the bottom stress components. The horizontal eddy friction terms $\tilde{F}_x$ and $\tilde{F}_y$ are defined as

$$\begin{aligned} \tilde{F}_x &= \frac{\partial}{\partial x}\Big[H2\overline{A}_M\frac{\partial \overline{U}}{\partial x}\Big] + \frac{\partial}{\partial y}\Big[H2\overline{A}_M(\frac{\partial \overline{U}}{\partial y} + \frac{\partial \overline{V}}{\partial x})\Big] \\ \tilde{F}_y &= \frac{\partial}{\partial y}\Big[H2\overline{A}_M\frac{\partial \overline{V}}{\partial y}\Big] + \frac{\partial}{\partial x}\Big[H2\overline{A}_M(\frac{\partial \overline{U}}{\partial y} + \frac{\partial \overline{V}}{\partial x})\Big] \end{aligned} \tag{5.4}$$

For the horizontal viscosity coefficient A_M the Smagorinsky diffusivity is used. The formula for the Smagorinsky diffusivity is

$$A_M = C\Delta x\Delta y\frac{1}{2}|\nabla \mathbf{V} + (\nabla \mathbf{V})^T| \tag{5.5}$$

where parameter C is given 0.2. An advantage of the Smagorinsky diffusivity is that A_M is specified depending on the model resolution and velocity. A_M decreases as resolution is improved and velocity gradients become smaller [34].

The model domain is chosen as a rectangular basin which cover the entire tomography domain with 38 × 27 grid points (Figure 5.13). The grid size is 200m

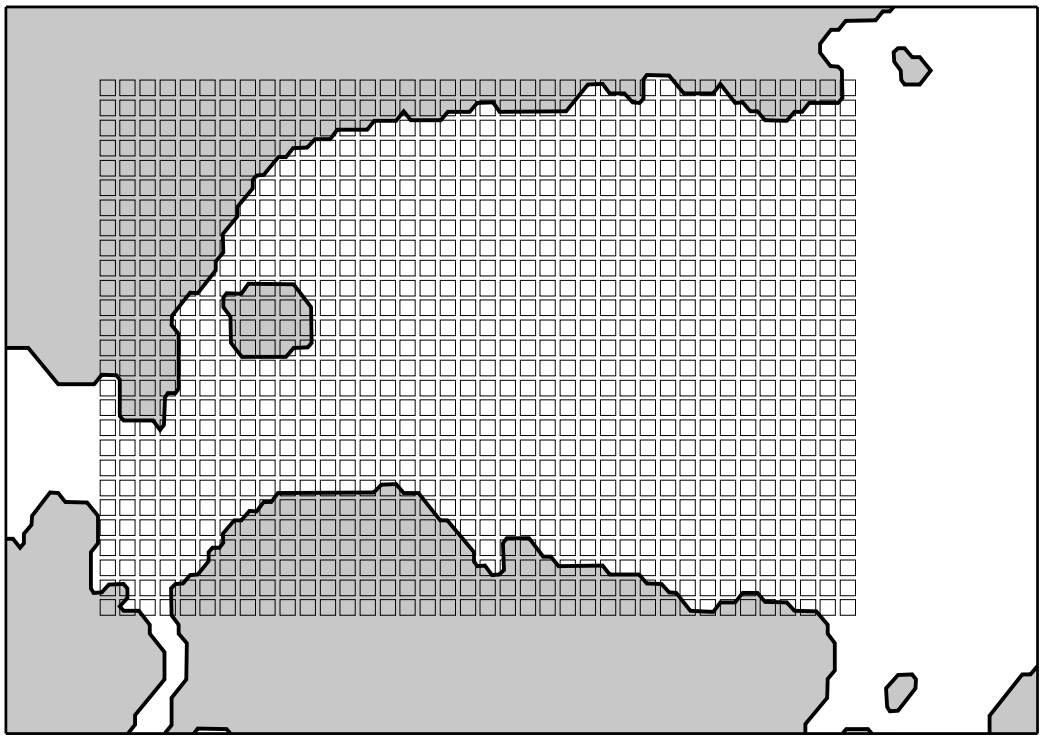

Figure 5.13: Model gird

for x- and y-directions and the realistic bottom topography is taken from the Coastal Area Topographic Map edited by the Japan Geographical Survey Institute. The open boundaries are introduced on the eastern and western sides. The time interval is set to 1s to satisfy the typical CFL (Courant-Friedrichs-Lewy) condition. M2 tidal sea level changes obtained at the nearest tidal gauge are given as the external forcing at the eastern and western open boundaries.

5.4.2 Data assimilation

In order to assimilate the CAT data into the two-dimensional ocean model the time-invariant Kalman gain filter based on Chandrasekher-type algorithm and the ensemble

Kalman filter (EnKF) based on Monte Carlo method are here applied to the Neko-Seto Channel data. Note that data assimilated into the model are not the current fields themshelves reconstructed by the inversion but the differential travel times obtained for each station pair because unknown errors are added to the reconstructed data after the inversion. Therefore, differential travel times are also calculated for the ocean model to make the innovation vector in (3.5). As the two-dimensional model used for the assimilation provides no information on temperature and salinity, the model ocean is assumed to be homogeneous. Thus, the ray paths of sound are refracted by the vertical profile of sound speed which increases with the pressure. However, since the current fields are barotropic in this region, only the straight, horizontal ray paths (direct ray paths) are considered in this study. The observation matrix $\mathbf{E}_k$ is obtained by projecting velocity fields onto the ray paths and integrating along each ray path. As a result, the $\mathbf{e}_k$ of equation (3.2) includes errors caused by this assumption.

For the time-invariant Kalman gain filter application the measurement error covariance matrix $\mathbf{R}_k$ and model error covariance matrix $\mathbf{Q}_k$ should be specified previously to calculate the Kalman gain. In consideration of the travel time accuracy of the CAT system ,the longer the distance between two acoustic stations, the smaller the velocity error becomes. Thus, the diagonal components of $\mathbf{R}_k$ are determined in the range of $(0.05\mathrm{ms}^{-1} \times 10^{-3})^2$ and $(0.1\mathrm{ms}^{-1} \times 10^{-3})^2$ by considering the distances between the stations. The measurement errors are assumed to be independent of the model errors and uncorrelated with time, so that $\mathbf{R}_k$ has only the diagonal components.

The model errors, caused by the tidal elevation uncertainties at the open boundaries, are difficult to be estimated. Those may be determined by a combination of dynamical intuition and trial-and-error. After the use of various values for the model errors the performance of the Kalman filter can be judged by monitoring differences between the observed and calculated differential travel times. The variance of model

errors is chosen to be $(80cm)^2$ for all the open boundary grids of the model. The model errors are assumed to be distributed through the following correlations

$$< \eta(x_0, y_m)\eta(x_0, y_n) >= (80cm)^2 \exp\left(-a\sqrt{(y_{m0} - y_{n0})^2}\right)$$
$$< \eta(x_M, y_m)\eta(x_M, y_n) >= (80cm)^2 \exp\left(-a\sqrt{(y_{mM} - y_{nM})^2}\right) \quad (5.6)$$

where x_0 and x_M denote the position at the western and eastern boundaries, respectively. The (y_{m0}, y_{n0}) and (y_{mM}, y_{mM}) are the set of the arbitrary boundary points at western and eastern boundaries, respectively. The a is determined 0.9. Before the time-invariant Kalman filter assimilation starts, the model is operated with sea level changes at the open boundaries. After the first spinning up of the model for a day, the assimilation starts.

To perform the assimilation by means of the EnKF, one hundred members of the state vectors are selected for the ensemble, which are made by adding the random errors to the sea level changes at the open boundaries. This process starts at the spinning up of the model for a day without the data assimilation. Each member of the ensemble is propagated forward with time through the ocean model and produces various initial state vectors just before the assimilation starts. During the data assimilation, the error covariance matrix $\mathbf{P}_k^f$, necessary for calculating Kalman gain, can be determined by using the mean and individual members of the ensemble. As described in Chapter 3, the tomography data should be disturbed by random errors to make an ensemble of measurements. The random velocity errors, which have the Gaussian distribution with a standard deviation of 5cms^{-1} for every pair of acoustic stations, are added to the tomography data.

Results from two kinds of data assimilations and the model result obtained at the phases of flood tides when strong tidal vortices appear are compared in Figures 5.14, 5.15, 5.16 and 5.17. In the model results without the data assimilation, tidal currents are too weak for actual tidal vortices to be generated even if the actual sea

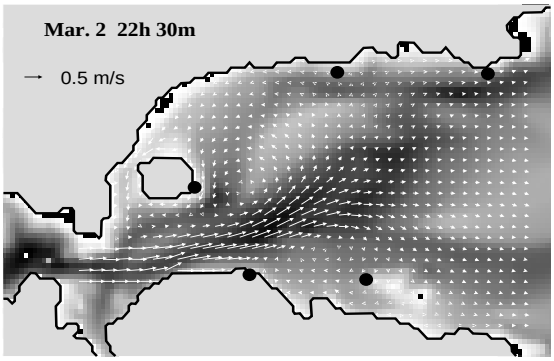

(a)

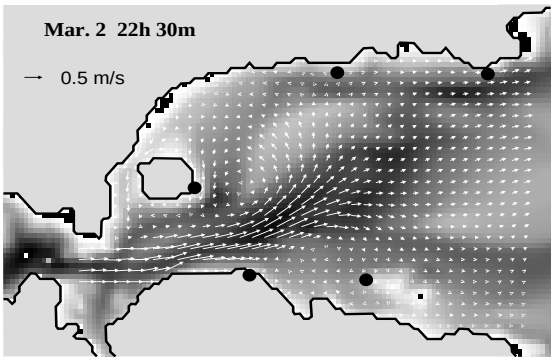

(b)

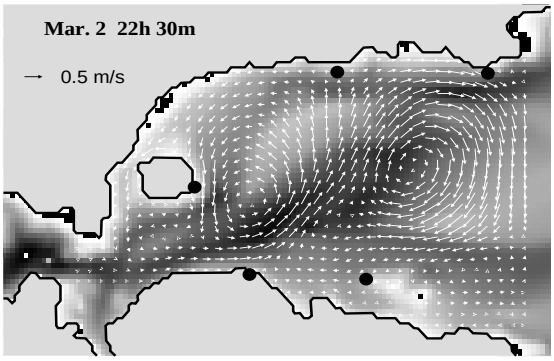

(c)

Figure 5.14: Vector plots of the tidal current fields obtained at 22:30 March 2 from the model (a) without assimilation, (b) with the time-invariant Kalman filter assimilation and (c) with the EnKF assimilation.

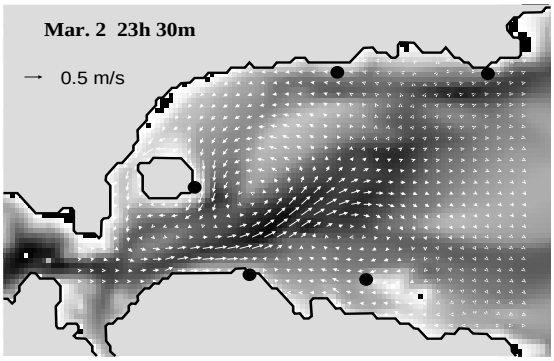

(a)

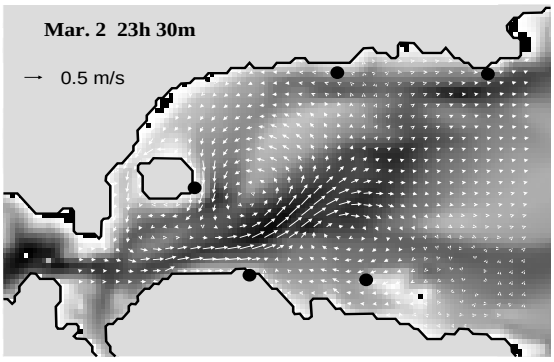

(b)

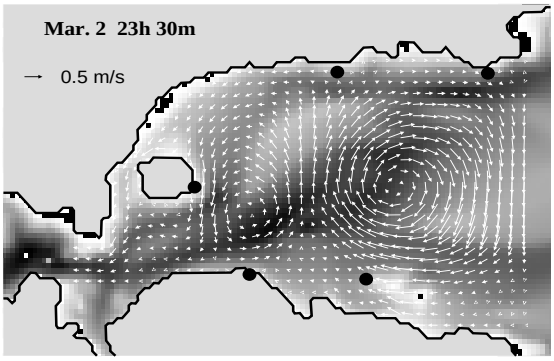

(c)

Figure 5.15: Vector plots of the tidal current fields obtained at 23:30 March 2 from the model (a) without assimilation, (b) with the time-invariant Kalman filter assimilation and (c) with the EnKF assimilation.

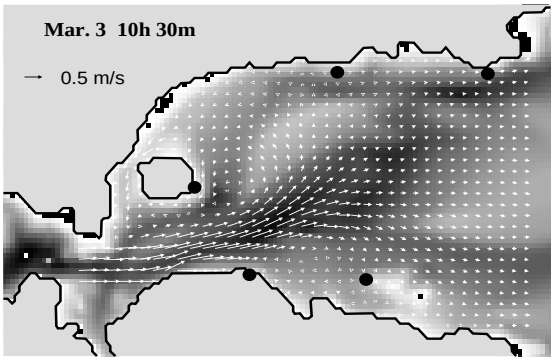

(a)

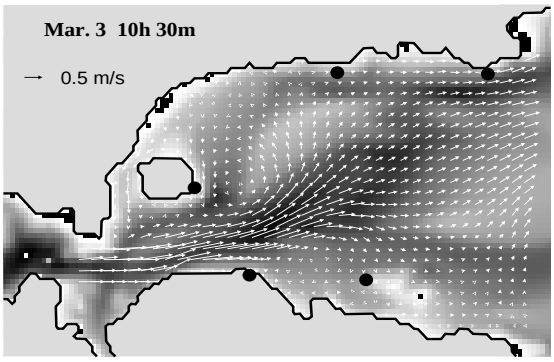

(b)

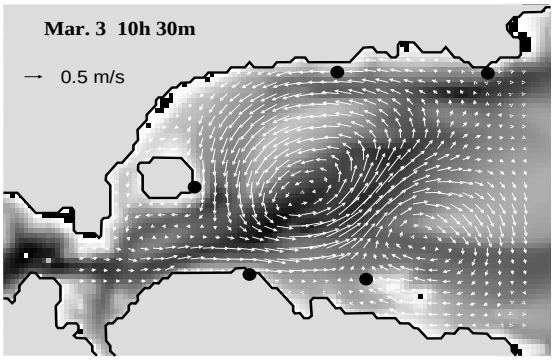

(c)

Figure 5.16: Vector plots of the tidal current fields obtained at 10:30 March 3 from the model (a) without assimilation, (b) with the time-invariant Kalman filter assimilation and (c) with the EnKF assimilation.

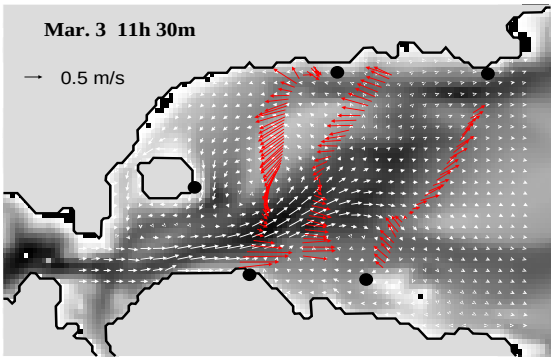

(a)

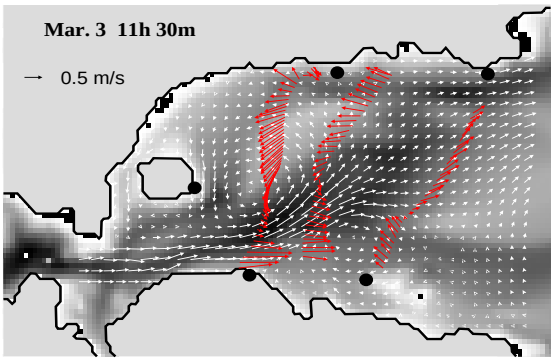

(b)

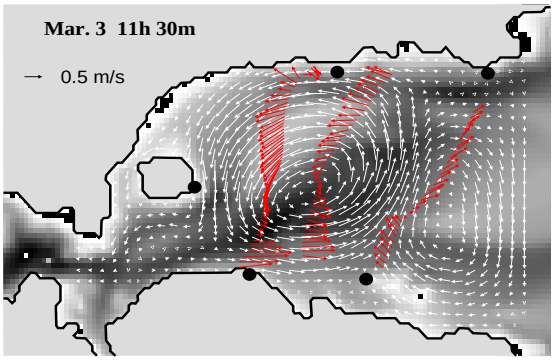

(c)

Figure 5.17: Vector plots of the tidal current fields obtained at 11:30 March 3 from the model (a) without assimilation, (b) with the time-invariant Kalman gain filter assimilation and (c) with the EnKF assimilation. The red vectors represent the shipboard ADCP data obtained during 10:40 to 12:40 March 3.

level data are imposed as the open boundary conditions of the model. The results from the time-invariant Kalman gain filter show tidal currents strengthened a little, but vortex formation is still not satisfactory in comparison with the pure inversion results. The role of the data assimilation is drastically understood with the EnKF results. The simulated vortex fields are surprisingly improved through the EnKF technique. The vortex shapes and locations are similar to the results of the pure inversion. The strength of the vortices obtained by the EnKF technique is closer to the ADCP data than from the pure inversion.

The results of data assimilation and pure inversion are compared with the shipboard ADCP data at all the ADCP data points in Figure 5.18. It is clearly seen that the data assimilation has a significant role in improving the tomography results. The velocity at the ADCP data points is simulated better by the EnKF data assimilation than by the pure inversion. Table 5.1 shows the average velocity obtained along three ADCP transects, numbered from west to east in order. The results are largely improved by the data assimilation based on the EnKF technique.

Table 5.1: Comparisons of the velocity means along the three ADCP transects between the ADCP data and tomography results. The ADCP transects are numbered from the western to the eastern.

Line number	Velocity component (cms^{-1})	ADCP	Tomography	
			Inversion (with B.C.)	Assimilation
1	Um	-29.6	-42.5	-21.5
	Vm	-35.0	-38.4	-29.5
2	Um	-6.5	-3.9	-6.5
	Vm	-2.5	25.2	7.3
3	Um	17.3	2.4	10.7
	Vm	24.6	13.4	17.1
Mean	Um	-6.3	-14.7	-5.8
	Vm	-4.3	0.1	-1.7

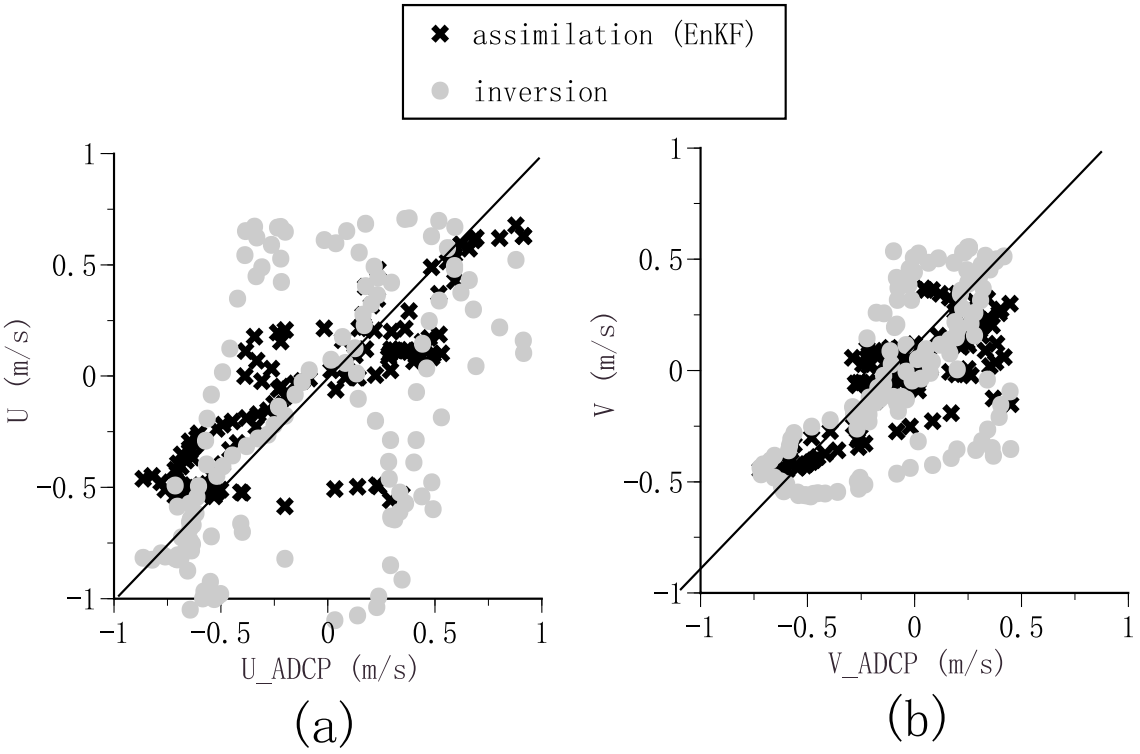

Figure 5.18: Scatter plots of the velocity components (a)u and (b)v obtained between the shipboard ADCP data and assimilation/inversion results. black crosses and gray dots represent the assimilation and inversion results, respectively.

5.5 Summary and discussion

The inversion results of the Bungo Channel experiment caught the counterclockwise/clockwise vortex of the elliptical shape which is clearly visible at the change of the flow direction from the north/south to south/north. In the Neko-Seto Channel experiment variable tidal vortices which changes with the tidal phases were reconstructed successfully. Such observations of the vortex fields are difficult to be achieved with the conventional point measurement technique of the same station number.

The differential travel time data obtained by the Neko-Seto Channel experiment were assimilated into two-dimensional ocean model. The data assimilation based on the time-invariant Kalman filter provides unsatisfactory results because it can

not work well for the strongly nonlinear phenomena such as tidal vortices while its computational time is largely saved. Much improved results for the tidal vortices are obtained by the data assimilation based on the EnKF. Comparison with the shipboard ADCP results shows that the EnKF results surpass the results of the pure inversion. It is because the dynamics and boundary conditions are satisfied in the EnKF technique.

The less accurate tomography data obtained in the Neko-Seto Channel experiment may be caused by that no data were acquired for three of ten acoustic ray paths which span five acoustic stations. Thus the differential travel time data only for the seven ray paths are available in the inversion and assimilation. It is expected that more accurate velocity fields can be reconstructed when data from all ten acoustic ray paths are available, rather than from just the seven used here.

Under the above consideration, we conclude that the data assimilation based on EnKF can be used as a quite powerful technique which is superior to the pure inversion in analyzing the CAT data. As a result of the assimilation, the coastal ocean model lacking the ability to simulate strongly nonlinear phenomena can reach a level sufficient for explaining them dynamically.

CHAPTER 6

GENERAL DISCUSSION

6.1 Inversion and data assimilation

If the conventional inverse analysis developed for the open ocean acoustic tomography is applied to the coastal acoustic tomography (CAT) of current velocity fields, two problems may occur. For the coastal seas with so variable current fields caused by an interaction between strong tidal currents and complex topographies, statistical information of current fields to be used for the conventional inversion may be so difficult to obtain prior to the tomography observation. The reason is why statistical information itself is also variable with tidal phases. Thus, a new inverse method with no use of *a priori* statistical information is required for the inversion of current fields in the coastal seas.

In Chapter 4, a new method to solve the problem mentioned above is proposed. The L-curve method determines the weighting factor α which appears in the damped least squares method. The α is equivalent to the ratio of the variance of noises to that of signals. In the conventional inverse method, α is determined by *a priori* information. The new inverse method allows α to be determined through a process seeking an optimal solution from travel time data at subsequent tidal phases. The current velocity fields obtained by the inversion can be corrected to satisfy the boundary conditions at the coast. This effect is also investigated through the computer simulation of acoustic tomography with a shore bounding the tomography domain. The result

shows that the effect of boundary correction is confined near the shore because the internal current field is forced to match with the travel time conditions provided by the ray paths passing the interior of the sea. In addition the boundary-fitted curvilinear coordinates are introduced to include the arbitrary shaped coastal boundaries into the inversion. The curvilinear coordinates may be so effective when the tomography stations are located at the periphery of the closed or semi-closed coastal seas.

The CAT can generally construct current velocity data with a resolution higher than the conventional point-measurement technique. This advantage of CAT is strengthened with increasing station number. However, the improvement of spatial resolution may still be required for CAT because of the limited number of station to be deployed in the sea. It is likely that current fields reconstructed by the inversion do not satisfy dynamic conditions due to errors introduced in the observation and inversion. Also the current velocity fields at subsequent time are independently reconstructed in the inversion while ocean currents have a continuous time-wise evolution. Such limited ability of CAT may be well improved through the assimilation of CAT data into an ocean model.

6.2 Extension to the three-dimensional current field analyses

In this study all of the data analyses and the field application are focused on two-dimensional current velocity fields. The extension of the present methods to three-dimensional cases may be expected in the application of CAT to the coastal sea with baroclinicity. There are two aspects to be considered for three-dimensional current field inversion. One is that we need an acoustic instrument which makes ray identification possible in the vertical section. The other is that we have to develop the inversion and data assimilation methods applicable to the three-dimensional current velocity fields. The former had been already demonstrated successfully by Zheng *et al.* [51, 52]. They showed that ray identification could be done by using a vertical array of hydrophones at each acoustic stations and the beamforming method. The

latter is an difficult issue which have never been studied by anybody until now.

For the inversion of three-dimensional current velocity fields, the vertical modes of current $Z_m(z)$ may be introduced. These modes are provided by the empirical orthogonal function (EOF) method of *a priori* current velocity data. If the first two modes are chosen as the simplest case, modes 0 and 1 correspond to the barotropic and the first baroclinic mode, respectively. By using the two modes the three-dimensional current fields may be expressed by the following equation:

$$\Psi(x,y,z) = \sum_{k=0}^{N}\sum_{l=0}^{N}\sum_{m=0}^{1}\{A_{klm}\cos\gamma_0(kx+ly) + B_{klm}\sin\gamma_0(kx+ly)\}Z_m(z) \qquad (6.1)$$

If two ray paths can be identified between two acoustic stations, the number of data and unknown variables is still balanced as in the two-dimensional case. There may be some difficulty to determine the EOF modes from the observation data. For this case, the EOF can be replaced by other function expansions.

The realization of three-dimensional data assimilation depends critically on the computer resource. First of all, the ocean model is modified three-dimensional and needs very huge computational time and capacity. The ensemble Kalman filter (EnKF) uses one hundred members of ensemble to estimate the covariance matrix. Each member propagates independently through the three-dimensional ocean model and the renewed members are stored in the memory. Suppose that 10 vertical layers are chosen for the three-dimensional ocean model. Then the length of state vector becomes 10 times greater than the two-dimensional one. The field application of data assimilation performed in Chapter 5 using usual Pentium II operated by Linux is too unrealistic to be done even for the case of 10 vertical layers. The innovation of the analytical method is also needed for realizing the three-dimensional acoustic tomography and the related data assimilation.

CHAPTER 7

CONCLUSIONS

In Chapter 2 the forward and inverse problems associated with the ocean acoustic tomography are reviewed. The forward problem is used for the ray identification, needed to solve the inverse problem. The fields of temperature and current velocity are reconstructed by using the identified travel time data. Though the Gauss-Markov method had been used as the most familiar technique in the ocean acoustic tomography, the damped least squares method can be an alternative to be selected when a priori statistical information is unavailable.

Data assimilation techniques which combine the measured data and a numerical ocean model are proposed in Chapter 3. Major results obtained in Chapter 3 are summarized as follows:

(1) The Kalman filter technique generally has a problem in its application to the large ocean model because it needs huge computational time and memory.

(2) The time-invariant Kalman gain filter based on Chandrasekhar-type algorithm has an advantage of reducing computational time, but not applicable to strongly nonlinear current fields.

(3) The ensemble Kalman filter (EnKF) based on the Monte Carlo method is proposed as the best method applicable to the CAT data assimilation, covering strongly nonlinear current fields.

New inverse methods for the CAT are proposed in Chapter 4. Major results obtained in Chapter 4 are summarized as follows:

(1) The L-curve method can determine the weighting factor α appearing in the damped least squares method without *a priori* statistical information.

(2) The current fields reconstructed by the inversion can be corrected to satisfy the closed boundary condition.

(3) Using the boundary-fitted curvilinear coordinates makes it easy to include the arbitrary shaped coastal boundaries into the inversion.

In Chapter 5 the proposed analytical methods are applied to two cases of CAT experiments, carried out in the Seto Inland Sea. Major results obtained in Chapter 5 are summarized as follows:

(1) The inversion results of the Bungo Channel experiment image the counterclockwise/clockwise vortex of the elliptical shape at the change of current direction from the north/south to south/north.

(2) In the Neko-Seto Channel experiment, the evolution process of tidal vortex fields is reconstructed successfully by the inversion based on the damped least squares method.

(3) The resolution and accuracy of the tidal vortex fields obtained in the Neko-Seto Channel are considerably improved by appling the EnKF technique of data assimilation.

From all the results above, it is concluded that the CAT is a powerful technique to reconstruct two-dimensional current fields through the inversion and assimilation of differential travel time data. The data assimilation is superior to the inversion if the appropriate ocean model is available in the region where a multiple set of CATs are deployed.

REFERENCES

[1] A. F. Blumberg and G. L. Meller. A description of a three-dimensional coastal ocean circulation model. *Three-dimensional coastal ocean models, Coastal Estuarine Sci.*, 4:1–16, 1987.

[2] G. Burgers, P. J. van Leeuwen, and G. Evensen. On the analysis scheme in the ensemble kalman filter. *Mon. Weather Rev.*, 126:1719–1724, 1998.

[3] D. Chester, P. Malanotte-Rizzoli, J. Lynch, and C. Wunsch. The eddy radiation field of the gulf stream as measured by ocean acoustic tomography. *Geophys. Res. Lett.*, 21:181–184, 1994.

[4] K. Cho, R. O. Ried, and W. D. Nowlin Jr. Objectively mapped stream function fields on the texas-louisiana shelf based on 32 months of moored current meter data. *J. Geophys. Res.*, 103:10377–10390, 1998.

[5] B. D. Cornuelle, W. Munk, and P. Worcester. Ocean acoustic tomography from ships. *J. geophys. Res.*, 94:6232–6250, 1989.

[6] B. D. Cornuelle and P. F. Worcester. Ocean acoustic tomography: Integral data and ocean models. In P. Malnaotte-Rizzoli, editor, *Modern Approaches to Data Assimilation in Ocean Modeling*, pages 97–115. Elsevier, 1996.

[7] B. D. Cornuelle, P. F. Worcester, J. A. Hildebrand, W. S. Hodgkiss, T. F. Duda Jr., J. Boyd, B. M. Howe, J. A. Mercer, and R. C. Spindel. Ocean acoustic tomography at 1000-km range using wavefronts measured with a large-aperture vertical array. *J. geophys. Res.*, 98:16365–16377, 1993.

[8] B. D. Cornuelle, C. Wunsch, D. Behringer, T. Birdsall, R. Heinmiller M. Brown, R. Knox, K. Metzger, W. Munk, J. Spiesberger, D. Webb R. Spindel, and P. Worcester. Tomography maps of the ocean mesoscale. part 1: Pure acoustics. *J. Phys. oceanogr.*, 15:133–152, 1985.

[9] B. D. Dushaw, P. F. Worcester, B. D. Cornuelle, and B. M. Howe. Variability of heat content in the central north pacific in summer 1987 determined from long-range acoustic transmissions. *J. Phys. oceanogr*, 23:2650–2666, 1993.

[10] B. D. Dushaw, P. F. Worcester, B. D. Cornuelle, and B. M. Howe. Barotropic currents and vorticity in the central north pacific ocean during summer 1987 determined from long-range reciprocal acoustic transmissions. *J. Geophys. Res*, 99:3263–3272, 1994.

[11] P. Elisseeff, H. Schmidt, M. Johnson, D. Herold, N. R. Chapman, and M. M. McDonald. Acoustic tomography of a coastal front in haro strait, british columbia. *J. Acoust. Soc. Am.*, 106:169–184, 1998.

[12] V. N. Eremeev, L. M. Ivanov, and A. D. Kirwan Jr. Reconstruction of oceanic flow characteristics from quasi-lagrangian data, 1, approach and mathematical method. *J. Geophys. Res.*, 97:9733–9742, 1992a.

[13] V. N. Eremeev, L. M. Ivanov, A. D. Kirwan Jr., O. V. Melnichenko, S. V. Kochergin, and R. R. Stanichnaya. Reconstruction of oceanic flow characteristics from quasi-lagrangian data, 2, characteristics of the large-scale circulation in the black sea. *J. Geophys. Res.*, 97:9743–9753, 1992b.

[14] G. Evensen. Sequential data assimilation with a nonlinear quasi-geostrophic model using monte carlo methods to forecast error statistics. *J. Geophys. Res.*, 99:10143–10162, 1994.

[15] I. Fukumori and P. Malanotte-Rizzoli. Assimilation of sea surface topography into an ocean circulation model using a steady-state smoother. *J. Geophys. Res.*, 100:6777–6793, 1995.

[16] F. Gaillard. Evaluating the information content of tomographic data: Application to mesoscale observations. *J. Geophys. Res*, 97:15489–15505, 1992.

[17] F. Gaillard, Y. Desaubies, U. Send, and F. Schott. A four-dimensional analysis of the thermal structure in the gulf of lion. *J. Geophys. Res*, 102:12515–12537, 1997.

[18] M. Ghil and P. Malanotte-Rizzoli. Data assimilation in meteorology and oceanography. *Adv. Geophys.*, 33:141–266, 1991.

[19] Ocean Acoustic Tomography Group. A demonstration of ocean acoustic tomography. *Nature*, 299:121–125, 1982.

[20] P. C. Hansen. Analysis of discrete ill-posed problems of the l-curve. *SIAM Rev.*, 34:561–580, 1992.

[21] P. C. Hansen and D. P. O'leary. The use of the l-curve in the regularization of discrete ill-posed problems. *SIAM J. Sci. Comput.*, 14:1487–1503, 1993.

[22] A. W. Heemink. *Storm Surge Prediction Using Kalman Filtering.* PhD thesis, Twente University of Technology, 1986.

[23] A. W. Heemink. Two-dimensional shallow water flow identification. *Appl. Math. Modelling*, 12:109–118, 1988.

[24] A. W. Heemink and H. Kloosterhuis. Data assimilation for non-linear tidal models. *Int. J. Numer. Meth. Fluids*, 11:1097–1112, 1990.

[25] A. E. Hoerl and R. W. Kennard. Ridge regression: biased estimation for non-orthogonal problems. *Technometrics*, 12:55–68, 1970.

[26] B. M. Howe, P. F. Worcester, and R. C. Spindel. Ocean acoustic tomography: mesoscale velocity. *J. Geophys. Res.*, 92:3785–3805, 1987.

[27] B. L. Lipphardt Jr., A. D. Kirwan Jr., C. E. Grosch, J. K. Lewis, and J. D. Paduan. Blending hf radar and model velocities in monterey bay through normal mode analysis. *J. Geophys. Res.*, 105:3425–3450, 2000.

[28] R. E. Kalman. A new approach to linear filtering and prediction problems. *Trans. ASME, Series D, J. Basic. Engr.*, 82:35–45, 1960.

[29] R. E. Kalman and R. S. Bucy. New results in linear filtering and prediction theory. *Trans. ASME, Series D, J. Basic. Engr.*, 83:95–108, 1961.

[30] A. Kaneko, G. Yuan, N. Gohda, and I. Nakano. Optimum design of the ocean acoustic tomography system for the sea of japan. *J. Oceanogr.*, 50:281–293, 1994.

[31] C. L. Lawson and R. J. Hanson. *Solving Least Squares Problems*. Prentice-Hall, Englewood Cliffs, NJ, 1974.

[32] P. B. Liebelt. *An Introduction to Optimal Estimation*. Addison-Wesley, Reading, MA, 1967.

[33] H. Madsen and R. Can nizares. Comparison of extended and ensemble kalman filters for data assimilation in coastal area modelling. *Int. J. Numer. Meth. Fluids*, 31:961–981, 1999.

[34] G. L. Mellor. *Users guide for a three-dimensional, primitive equation, numerical ocean model*. Program in Atmospheric and Oceanic Sciences, Princeton University, Princeton, NJ, 1998.

[35] D. Menemenlis and Michael Chechelnitsky. Error estimates for an ocean general circulation model from altimeter and tomography data. *Mon. Weather Rev.*, 128:763–778, 2000.

[36] W. Menk. *Geophysical Data Analysis: Discrete Inverse Theory.* 2nd ed. Academic Press, San Diego, 1989.

[37] W. M. L. Morawitz, P. J. Sutton, P. F. Worcester, and B. D. Cornuelle. Three-dimensional observations of a deep convective chimney in the greenland sea during winter 1988/89. *J. Phys. Oceanogr.*, 26:2316–2343, 1996.

[38] W. Munk, P. F. Worcester, and C. Wunsch. *Ocean Acoustic Tomography.* Cambridge University Press, New York, 1995.

[39] W. H. Munk and C. Wunsch. Ocean acoustic tomography: A scheme for large scale monitoring. *Deep-Sea Res.*, 26:123–161, 1979.

[40] S. J. Norton. Unique tomography reconstruction of vector fields using boundary data. *IEEE Trans. Image Process.*, 1:406–412, 1992.

[41] D. B. Rao and D. J. Schwab. A method of objective analysis for currents in a lake with application to lake ontario. *J. Phys. Oceanogr.*, 11:739–750, 1981.

[42] U. Send, F. Schott, F. Gaillard, and Y. Desaubies. Observation of a deep convection regime with acoustic tomography. *J. Geophys. Res*, 100:6927–6941, 1995.

[43] J. Sheinbaum. Variational assimilation of simulated acoustic tomography data and point observations: A comparative study. *J. Geophys. Res.*, 100:20745–20761, 1995.

[44] H. Sielschott. Measurement of horizontal flow in a large scale furnace using acoustic vector tomography. *Flow Meas. Instrum.*, 8:191–197, 1997.

[45] Y. Takasugi, T. Fujiwara, and T. Sugimoto. Formation of sand banks due to tidal vortices around straits. *J. Oceanogr.*, 50:81–98, 1994.

[46] J. F. Thompson, Z. U. Warsi, and C. W. Mastin. *Numerical Grid Generation: Foundations and Applications.* Elsevier, Amsterdam, 1985.

[47] R. Todling and S. E. Cohn. Suboptimal schemes for atmospheric data assimilation based on the kalman filter. *Mon. Weather Rev.*, 122:2530–2557, 1994.

[48] M. Verlaan and A. W. Heemink. Reduced rank square root filters for large scale data assimilation problems. In *Second International Symposium on Assimilation of Observations in Meteorology and Oceanography*, pages 247–252. World Meteorological Organization, WMO, March 1995.

[49] C. Wunsch. *The Ocean Circulation Inverse Problem.* Cambridge University Press, New York, 1996.

[50] G. Yuan, I. Nakano, H. Fujimori, T. Nakamura, T. Kamoshida, and A. Kaya. Tomographic measurements of the kuroshio extension meander and its associated eddies. *Geophys. Res. Lett.*, 26:79–82, 1999.

[51] H. Zheng, N. Gohda, H. Noguchi, T. Ito, H. Yamaoka, T. Tamura, Y. Takasugi, and A. Kaneko. Reciprocal sound transmission experiment for current measurement in the seto inland sea, japan. *J. Oceanogr.*, 53:117–127, 1997.

[52] H. Zheng, H. Yamaoka, N. Gohda, H. Noguchi, and A. Kaneko. Design of the acoustic tomography system for velocity measurement with an application to the coastal sea. *J. Acoust. Soc. Jpn. (E)*, 19:199–210, 1998.

ACKNOWLEDGEMENTS

First of all, I would like to thank my advisor Prof. Arata Kaneko, without whose continuous encouragement, suggestions and guidance this work would have been impossible. Special thanks are extended to Prof. Noriaki Gohda for his kind advice and scientific suggestions.

I am deeply grateful to the members of the committee, Profs. Mitsumasa Okada, Masakazu Shiba, and Yasushi Higo for their valuable suggestions, helpful criticisms and careful reading.

There are also many people whom I want to thank to; Mr. Haruhiko Yamaoka for his friendship, companionship and helping in data analysis, Mr. Tadashi Takano, Drs. Hong Zheng, Xiao-Hua Zhu, and Yoshio Takasugi for their help in field observation, Dr. Masazumi Arai for providing me the spectral model and many valuable suggestions, and Mr. Isao Sin-no for providing me the figures of his data anslysis results.

I want to thank to my parents, parents-in-law, sisters, brother-in-laws, and sister-in-law for there continuous support and encouragement.

Finally, I would like to give my special thanks to my lovely wife, Jiyeong, and my cute daughter, Sunwoo, for their patience, support, and love. I would like to dedicate this work to them.